

# Microglia activation and Lipid droplet pathology in animal models of type 2 diabetes and Alzheimer's disease

Mona Havik



Master Thesis for the title of Master in Pharmacy

45 credits

Section for Pharmacology and Pharmaceutical Biosciences  
Department of Pharmacy

The Faculty of Mathematics and Natural Sciences

UNIVERSITY OF OSLO

June 2021



# Microglia activation and Lipid droplet pathology in animal models of type 2 diabetes and Alzheimer's disease

Mona Havik



Main supervisor  
Associate professor Cecilie Morland

Co-supervisor  
PhD Student Gezime Seferi

Department of Pharmacy  
The Faculty of Mathematics and Natural Sciences

UNIVERSITY OF OSLO

June 2021

© Mona Havik - Department of Pharmacy, The Faculty of Mathematics and Natural Sciences,  
University of Oslo

2021

**Microglia activation and Lipid droplet pathology in animal models of type 2 diabetes  
and Alzheimer's disease**

Mona Havik

<http://www.duo.uio.no/>

Print: University Print Centre, University of Oslo

IV



# Acknowledgements

This master thesis is performed and written as a part of the Neurobiology and Toxicology group at the Section for Pharmacology and Pharmaceutical Biosciences, Department of Pharmacy, University of Oslo.

I would especially give a big thank you to my supervisors, associate professor Cecilie Morland and PhD student Gezime Seferi, for their guidance, optimism, motivation and availability throughout this master project. Their knowledge has given me inspiration and I want to thank them for everything they have taught me. I would also express my gratitude to the Neurobiology and Toxicology group for all the good talks, guidance and support during the entire master project.

A special thank you to my wonderful classmates, who have always supported me and contributed to good memories throughout the master study.

Lastly, I would like to thank my mom, dad and sister for the endless love and support they have given me. Thank you for as always believing in me.

Mona Havik

University of Oslo, June 2021



# Abstract

Alzheimer's disease (AD) is the most common cause of dementia. Globally, AD is among the 7 leading cause of death and significant affect the quality of life for the individuals affected and their relatives (World Health Organization, 2020). People with type 2 diabetes mellitus (T2DM) has an increased risk of developing AD, perhaps because the pathological processes in the brain are partly overlapping. Both AD and T2DM display increasing prevalence in the population. Research on pathological mechanisms for AD and diabetes-related dementia is important to acquire treatment options and improve life quality.

Research over the past decade has shown increasing evidence for an important role of neuroinflammation in AD pathology. Furthermore, recent studies have shown an interest in neutral lipids stored in lipid droplets in the brain as a possible mechanism for neuroinflammation (Marschallinger et al., 2020). Also, lipid droplets have been shown to accumulate in microglia, which are the resident immune cells of the brain and are identified as having a key role in neuroinflammation. The purpose of the present study is to investigate the potential effects of microglia activation and the accumulation of lipid droplets in the brain of mice with T2DM and AD.

Animal models for AD and T2DM were used to investigate microglia activation and lipid droplets pathology in the mouse brain. Exercised obese diabetic mice were also used in Morris water maze, a behavioral test to assess spatial memory and learning. Further, immunohistochemistry was performed to study microglia activation and lipid droplet accumulation. We found that microglia activation was higher in affected brain regions in mice with T2DM and AD: The AD mice had significantly higher microglia activation than its wild type control mice and the obese diabetic mice tended towards a higher state of microglia activation compared to their control genotype. Interestingly, no significant difference in lipid droplets accumulation was found between any of the animal models or genotypes. The T2DM mice tended towards performing worse than their non-diabetic littermates in the Morris water maze test for spatial memory. Furthermore, we found exercise to have a positive effect on cognitive function and mice with T2DM having an impaired memory performance, but a larger group of animals is needed for a final conclusion to be drawn. Overall, these results suggest that neuroinflammation plays a key role in neurodegenerative diseases, although lipid droplets do not appear to affect the microglia activation.





# Abbreviations

<b>5xFAD</b>	5 mutations for Familial Alzheimer's Disease
<b>A<math>\beta</math></b>	Amyloid- $\beta$
<b>AD</b>	Alzheimer Disease
<b>APOE</b>	Apolipoprotein E
<b>APP</b>	Amyloid precursor protein
<b>ARMS-PCR</b>	Amplification refractory mutation system-polymerase chain reaction
<b>BBB</b>	Blood-brain barrier
<b>BODIPY</b>	4,4-Difluoro-1,3,5,7,8-Pentamethyl-4-Bora-3a,4a-Diaza-s-Indacene
<b>BSA</b>	Bovine serum albumin
<b>bp</b>	Base pairs
<b>CA1</b>	Cornu ammonis 3
<b>CA3</b>	Cornu ammonis 3
<b>CSF</b>	Cerebrospinal fluid
<b>CNS</b>	Central nervous system
<b>COVID-19</b>	Coronavirus disease 2019
<b>CSF</b>	Cerebrospinal fluid
<b><i>db/+</i></b>	Heterozygous from the <i>Lepr<sup>db</sup></i> colony
<b><i>db/db</i></b>	Homozygous for the diabetes spontaneous mutation ( <i>Lepr<sup>db</sup></i> )
<b>DG</b>	Dentate gyrus
<b>DMSO</b>	Dimethyl Sulfoxide
<b>DNA</b>	Deoxyribonucleic acid
<b>dNTPs</b>	Deoxynucleotides
<b>E</b>	East
<b>ER</b>	Endoplasmic reticulum
<b>FI</b>	Forward inner
<b>FO</b>	Forward outer
<b>GFAP</b>	Glial fibrillary acidic protein
<b>GLUT1</b>	Glucose transporter type 1
<b>GLUT4</b>	Glucose transporter type 4
<b>Iba1</b>	Ionized calcium binding adaptor molecule 1

<b>IHC</b>	Immunohistochemistry
<b>IL-6</b>	Interleukin 6
<b>IL-1<math>\beta</math></b>	Interleukin 1 $\beta$
<b>IR</b>	Insulin receptor
<b>IRS1</b>	Insulin receptor substrate 1
<b>IRS2</b>	Insulin receptor substrate 2
<b>I.p.</b>	Intraperitoneal
<b>Lepr</b>	Leptin receptor
<b>LD</b>	Lipid droplets
<b>LTD</b>	Long-term depression
<b>LTP</b>	Long-term potentiation
<b>MAPK</b>	Mitogen-activated protein kinase
<b>MECT</b>	Maximal exercise capacity test
<b>MWM</b>	Morris water maze
<b>N</b>	North
<b>NaPi</b>	Sodium phosphate
<b>NCS</b>	Newborn calf serum
<b>NO</b>	Nitric oxide
<b>OP 1</b>	Operator 1
<b>OP 2</b>	Operator 2
<b>PCR</b>	Polymerase chain reaction
<b>PFA</b>	Paraformaldehyde
<b>PI3K</b>	Phosphoinositide 3-kinase
<b>PS1</b>	Presenilin 1
<b>PS2</b>	Presenilin 2
<b>RI</b>	Reverse inner
<b>RO</b>	Reverse outer
<b>ROI</b>	Region of interest
<b>ROS</b>	Reactive oxygen species
<b>rpm</b>	Revolutions per minute
<b>S</b>	South
<b>SARS-CoV-2</b>	Severe acute respiratory syndrome coronavirus 2
<b>SR</b>	Scavenger receptor

<b>SE</b>	South-east
<b>SW</b>	South-west
<b>T2DM</b>	Type 2 Diabetes Mellitus
<b>TAE</b>	Tris-acetate-EDTA
<b>TAGs</b>	Triacylglycerols
<b>Tg</b>	Transgenic
<b>TD-NMR</b>	Time Domain Nuclear Magnetic Resonance
<b>TNF- <math>\alpha</math></b>	Tumor necrosis factor $\alpha$
<b>TWS</b>	Trainable Weka Segmentation
<b>W</b>	West
<b>WHO</b>	World Health Organization
<b>Wt</b>	Wild type



# Table of contents

<b>1</b>	<b>Introduction .....</b>	<b>1</b>
1.1	Alzheimer's disease.....	1
1.1.1	Epidemiology .....	1
1.1.2	Aetiology and pathophysiology .....	1
1.2	Type 2 diabetes mellitus.....	4
1.2.1	Epidemiology .....	4
1.2.2	Aetiology and pathophysiology .....	4
1.3	Overlap of pathophysiology in type 2 diabetes mellitus and Alzheimer's disease ....	5
1.4	Neuroinflammation .....	9
1.4.1	Microglia .....	9
1.4.2	Microglia activation .....	10
1.4.3	Neuroinflammation in Alzheimer disease.....	11
1.4.4	Lipid droplets .....	14
1.5	Exercise and lipid droplets .....	15
1.6	Using mice as models for type 2 diabetes mellitus and Alzheimer's disease .....	16
<b>2</b>	<b>Aims of the study .....</b>	<b>18</b>
<b>3</b>	<b>Materials and methods.....</b>	<b>19</b>
3.1	Chemicals and reagents .....	19
3.2	Animals .....	21
3.3	Genotyping .....	23
3.3.1	Extraction and isolation of genomic DNA .....	23
3.3.2	Precipitation of DNA .....	25
3.3.3	Polymerase chain reaction.....	26
3.3.4	Gel electrophoresis .....	29
3.3.5	Interpretation of the results .....	30
3.4	Open field.....	30
3.5	Exercise regime .....	32
3.6	Body weight and body composition measurements .....	35
3.7	Morris Water Maze .....	36
3.8	Perfusion fixation .....	40
3.9	Cryostat sectioning.....	41
3.10	Immunohistochemistry .....	43
3.10.1	Buffers and solutions.....	44
3.10.2	Procedure for immunohistochemistry along with BODIPY labeling .....	44

3.10.3	Image acquisition with confocal microscopy.....	47
3.11	Image analysis of microglia activation and lipid droplets.....	48
3.11.1	Preparation and processing of the images for quantification of microglial cells 48	
3.11.2	Segmentation of microglia .....	50
3.11.3	Skeletonize .....	51
3.11.4	Quantitative analysis of lipid droplets.....	53
3.12	Statistics .....	54
<b>4</b>	<b>Results .....</b>	<b>56</b>
4.1	Genotyping .....	56
4.2	Body weight .....	57
4.3	Body composition .....	58
4.4	Physical performance in the maximal exercise capacity test.....	59
4.5	Open Field Exploration test.....	60
4.6	Learning and memory performance in the Morris Water Maze test.....	63
4.7	Microglia activation in sedentary <i>db/db</i> and <i>db/+</i> mice .....	70
4.8	Microglia activation in 5xFAD and wild type mice.....	73
4.8.1	Microglia activation and lipid droplets in exercised and sedentary <i>db/db</i> and <i>db/+</i> mice .....	75
4.9	Lipid droplets within microglia in <i>db/db</i> and <i>db/+</i> sedentary mice.....	76
4.10	Lipid droplets within microglia of 5xFAD and wild type mice.....	78
<b>5</b>	<b>Discussion.....</b>	<b>81</b>
5.1	Methodological considerations .....	81
5.1.1	Animals .....	81
5.1.2	Exercise regime .....	84
5.1.3	Perfusion fixation .....	85
5.1.4	Cryoprotection and cryostat sectioning.....	87
5.1.5	Immunohistochemistry .....	87
5.2	Interpretation and discussion of findings .....	88
5.2.1	Body composition .....	88
5.2.2	Effect of exercise on microglia activation and lipid droplet number and morphology .....	89
5.2.3	Open field Exploration test .....	89
5.2.4	Learning and memory performance in the Morris water maze.....	91
5.2.5	Microglia activation .....	93
5.2.6	Lipid droplets in microglia.....	96
<b>6</b>	<b>Conclusion.....</b>	<b>100</b>

<b>References .....</b>	<b>102</b>
<b>Appendixes .....</b>	<b>112</b>
Appendix I: Equipment .....	112
Appendix II: MWM form.....	113
Appendix III: Fiji macros .....	115



# 1 Introduction

## 1.1 Alzheimer's disease

### 1.1.1 Epidemiology

Alzheimer's disease (AD) is the most common cause of dementia and was globally ranked as the 7<sup>th</sup> leading cause of death (along with other forms of dementia) in 2019 by the World Health Organization (WHO) (World Health Organization, 2020). AD has an increasing prevalence in the population and the incidence increases with age. According to literature, the prevalence of dementia nearly doubles every 5-6 years after the age of 65 (GjØra et al., 2021; Reitz & Mayeux, 2014). Worldwide around 50 million people live with dementia, where AD covers 60-70 % of these cases (Patterson, 2018; World Health Organization, 2017). In Norway, it is estimated that around 57,600 people are diagnosed with AD, and this is likely to rise to about 134,900 people by 2050 (GjØra et al., 2021). The increased prevalence of AD leads to an increased socioeconomic burden on society. AD creates disability and dependency in the patient's life, hence does not only have a significant impact on individuals but also on their friends and families. The current global cost of dementia is about a trillion US dollars a year and is estimated to increase to three trillion US dollars by 2030 (GjØra et al., 2021; Patterson, 2018; World Health Organization, 2017).

### 1.1.2 Aetiology and pathophysiology

AD is a progressive, neurodegenerative disease affecting cognitive abilities (i.e., memory and thinking) and behavior (Kinney et al., 2018). Accumulation of amyloid- $\beta$  (A $\beta$ ) plaques and neurofibrillary tangles formed by hyperphosphorylated tau fibrils are hallmarks of AD. The precise mechanisms behind the pathology of AD are not fully determined, although A $\beta$  plaques and neurofibrillary tangles together with neurodegeneration, synaptic loss, glial activation and neuroinflammation make important contributions to disease progression (Bronzuoli, Iacomino, Steardo, & Scuderi, 2016; Molinuevo et al., 2018).

The majority of people with AD are above 65 years of age, but 1-5 % of the affected individuals get the disease before the age of 65. AD is classified into early-onset AD (if onset is before the age of 65) and late-onset (if disease onset is above the age of 65) (Reitz &

Mayeux, 2014). Early-onset AD is generally due to genetic inheritance with mutations in the genes encoding the amyloid precursor protein (APP), presenilin 1 (PS1) or presenilin 2 (PS2), being the most prominent. These mutations are rare in the population but increases the risk to suffer from AD by a large degree. In these cases, the resulting AD is considered familial AD (FAD). The genetic predisposition caused by mutations in the APP and the PS genes follow autosomal dominant inheritance and all of them contribute to enhanced production of pathological A $\beta$  (Heppner, Ransohoff, & Becher, 2015; Yankner, 1996). Most cases of AD, however, are sporadic and late-onset with a non-Mendelian pattern of inheritance. There are also predisposing genetic factors for this type of AD, such as apolipoprotein E (APOE), where the  $\epsilon$ 4 allele is the most important genetic risk factor for sporadic AD (Koffie et al., 2012; Reitz & Mayeux, 2014). Having one of the APOE  $\epsilon$ 4 alleles is shown to result in a 2- to 3-fold increase in the risk of developing AD. Being homozygous for the APOE  $\epsilon$ 4 is associated with a twelve-fold increase in the risk of developing AD (Karch & Goate, 2015). In the central nervous system (CNS), APOE is primarily produced in astrocytes and its main function is believed to be to transport cholesterol to neurons via APOE receptors (Heppner et al., 2015). It has been suggested that the APOE  $\epsilon$ 4 allele may cause accelerated loss of neuronal function as cholesterol is important for synaptogenesis and dendritic remodeling (Poirier, 1994). Genes associated with increased risk of AD is listed in figure 1.

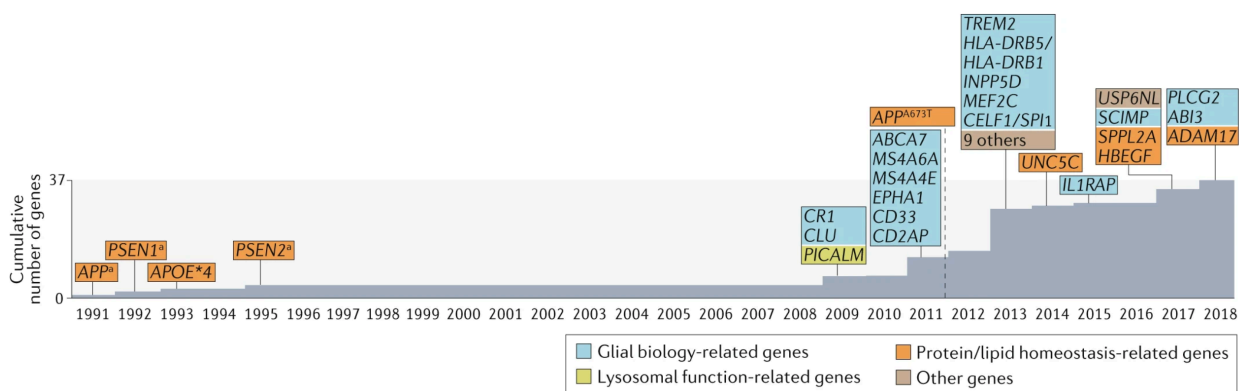


**Figure 1: Genes related to increase the risk of developing Alzheimer disease.**

The timeline of the genes illustrates the date on which their involvement with the disease was first published and classified by biological function categories. The majority of genes are associated with microglial biology (blue) suggesting microglia has an important impact on the pathogenesis of AD. <sup>a</sup> = Mutations in genes which can cause the autosomal dominant form of AD. PSEN1 is the gene encoding presenilin 1 and PSEN2 is the gene for presenilin 2. AD; Alzheimer's disease. Image retrieved from: (Searce-Levie, Sanchez, & Lewcock, 2020).

AD predominantly affects the neocortex and the hippocampus. Both of these brain regions are involved in memory and cognition. The neocortex is the seat for memory storages and is

important for cognition and complex integration of information. The hippocampus has an essential role in regulating spatial learning and memory processes, as well as affective behaviors (T. H. Lee & Yau, 2020; Vorhees & Williams, 2014). Hence, degeneration and/or dysregulation of these regions may explain the key symptoms of AD. Hippocampus is divided into the Cornua ammonis and dentate gyrus (DG), where cornua ammonis contains of the cornu ammonis 1 (CA1), cornu ammonis 2 (CA2) and cornu ammonis 3 (CA3) and consist of a unique pattern (c-shaped) of dense packed neurons (figure 2) (Anand & Dhikav, 2012; Leuner & Gould, 2010). Neurogenesis takes place in the subgranular zone of the DG and seems to be activated by stimuli such as training and learning (Gould, Beylin, Tanapat, Reeves, & Shors, 1999; van Praag, Christie, Sejnowski, & Gage, 1999). AD results in synaptic loss, neurodegeneration, inflammation, amyloid plaques and tau tangles throughout the hippocampus and cerebral cortex (Sheppard & Coleman, 2020), accompanied by cognitive impairment.

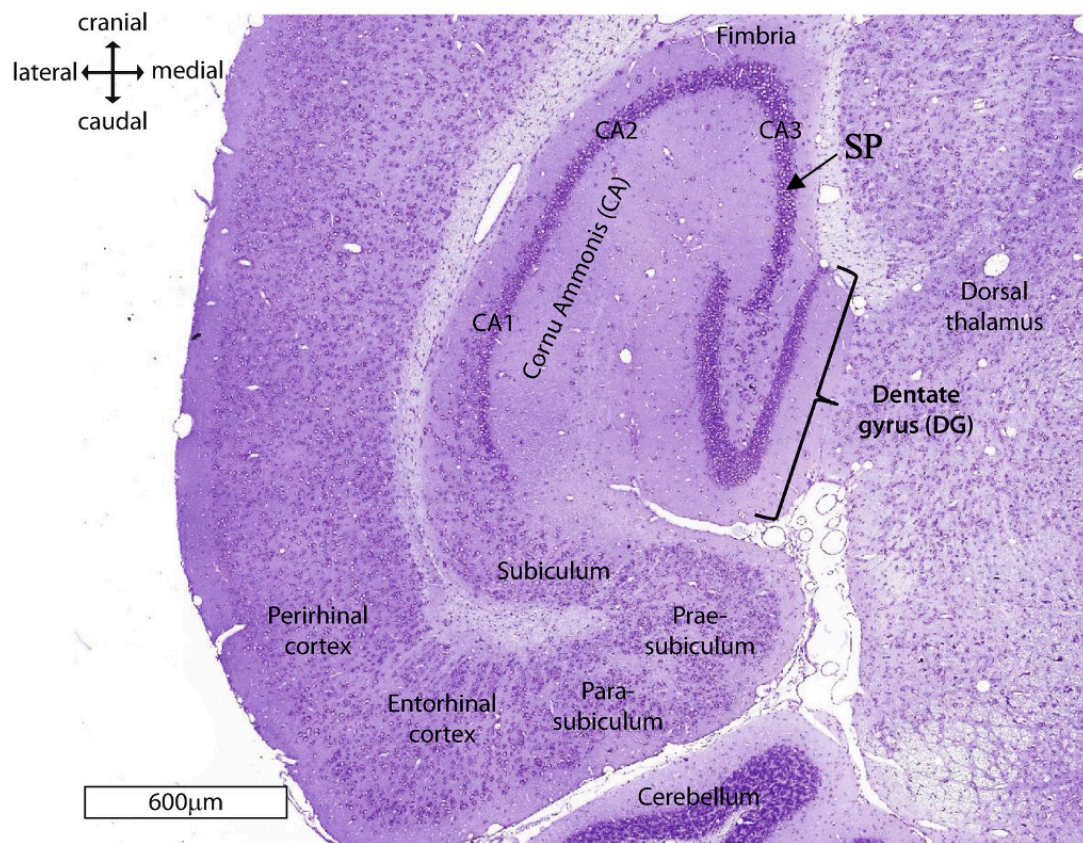


**Figure 2: The hippocampal formation.**

The hippocampus consists of the C-shaped Cornu Ammonis with its subdivisions (CA1-CA3) and the V-shaped dentate gyrus. The defined densely packed cell layer forms the stratum pyramidale, and the c-shape in CA, as indicated by the arrow and "SP" in the image. SP; Stratum pyramidale. Image retrieved from: (Schröder, Moser, & Huggenberger, 2020).

## 1.2 Type 2 diabetes mellitus

### 1.2.1 Epidemiology

Type 2 diabetes mellitus (T2DM) is a growing global health problem, closely associated with the increase of obesity. T2DM is the most common type of diabetes, accounting for approximately 90 % of all cases (DeFronzo et al., 2015; World Health Organization, 2016). The International Diabetes Federation (IDF) estimated that in 2017 the world-wide number of people living with T2DM were 451 million (Cho et al., 2018). Diabetes mellitus (in general) was ranked among the top ten causes of death in 2019 by the WHO (World Health Organization, 2020). Physical inactivity, unhealthy diet, obesity, ageing, and genetic factors are all examples of risk factors for T2DM (Kahn, Cooper, & Del Prato, 2014).

### 1.2.2 Aetiology and pathophysiology

T2DM is a progressive disease characterized by insulin resistance (a condition in which cells are no longer properly responding to circulating insulin), impaired insulin secretion and chronic inflammation, primarily in adipose tissue, liver, and skeletal muscle (Bonadonna & De Fronzo, 1991; Sears & Perry, 2015). Although severe T2DM can also affect every insulin-sensitive organ system in the body, by accumulation and expansion of adipose tissue, promoting immune cells contributing with an expression of pro-inflammatory cytokines and free radicals, and hence, a formation of chronic low-level inflammation (Daryabor, Atashzar, Kabelitz, Meri, & Kalantar, 2020). In the early phases, the pancreatic  $\beta$ -cells are able to counteract the reduced insulin sensitivity by increasing the amounts of insulin they secrete. Clinically, T2DM occurs only when the  $\beta$ -cells are no longer able to secrete sufficient amounts of insulin to compensate for the (partial) insulin resistance. During the development of T2DM, the pancreatic  $\beta$ -cells show progressively impaired insulin secretion, combined with a background of pre-existing insulin resistance in the liver, skeletal muscle and adipose tissue (Kahn et al., 2014). Insulin is one of the key hormones involved in carbohydrate-, protein- and fat metabolism and is secreted by pancreatic  $\beta$ -cells as a response to an increase in blood glucose (i.e., after eating) (Geser, 1976; Leto & Saltiel, 2012). There are several potential molecular causes of insulin resistance, however, they are all either indirectly or directly linked with increased inflammation. Hence, increased inflammation may interrupt the feedback mechanisms for insulin secretion and lead to hyperglycemia, metabolic syndrome,

obesity and finally, T2DM (Sears & Perry, 2015). Lifestyle modifications with exercise and weight loss generally reduce the level of insulin resistance and delay diabetes onset or reduce the severity of the disease, including the risk of long-term complications (DeFronzo et al., 2015; Kahn et al., 2014).

### **1.3 Overlap of pathophysiology in type 2 diabetes mellitus and Alzheimer's disease**

#### **Risk factors**

The main symptoms of T2DM and AD are very different, although the diseases share many of the same risk factors. Ageing, obesity and hypertension are important risk factors for both diseases (Reitz & Mayeux, 2014; World Health Organization, 2016). Based on the similarities in pathology, AD is presented by some authors as “brain diabetes” and T2DM is regarded a risk factor -perhaps even a cause- for AD/dementia (Arnold et al., 2018; de la Monte & Wands, 2008). In fact, epidemiological studies have reported that the incidence of AD is ~ 1.5- to 2-fold higher in patients with T2DM (Gudala, Bansal, Schifano, & Bhansali, 2013; T. Wakabayashi et al., 2019). A high-caloric diet in combination with low levels of physical activity are the most important cause of obesity and T2DM, two significant risk factors for neurodegeneration in the hippocampus and cognitive deficits (T. H. Lee & Yau, 2020). Dietary nutrients, especially saturated fatty acids, sugar and cholesterol have pro-inflammatory effects. Excessive intake of pro-inflammatory nutrients may initiate a chronic low-grade inflammatory response, which further develops to diseases as T2DM or AD (Christ, Lauterbach, & Latz, 2019; Gregor & Hotamisligil, 2011). Insulin resistance is the hallmark of T2DM, and research show that it also appears in the brains of people with AD (Arnold et al., 2018; Blázquez, Velázquez, Hurtado-Carneiro, & Ruiz-Albusac, 2014).

#### **Related mechanisms**

Insulin is a peptide hormone which is involved in several processes within the major cell types in the brain. Insulin receptor substrate 1 (IRS1) and insulin receptor substrate 2 (IRS2) are both expressed in neurons at presynaptic and postsynaptic ends. In the healthy brain, insulin regulates neurogenesis, long-term potentiation (LTP), long-term depression (LTD), and inhibits apoptosis. In microglia and astrocytes, insulin is involved in regulation of inflammatory responses, including cytokine secretion. Finally, in the blood-brain barrier

(BBB), insulin enhances cerebral perfusion through vasodilatation mediated by nitric oxide (NO) (Arnold et al., 2018). Key functions of insulin signaling in neurons, microglia, astrocytes, and the vascular system are illustrated in figure 3. Both peripheral and central insulin resistance have been associated with cognitive impairments and AD pathology, although the mechanism remains unclear (Arnold et al., 2018; T. H. Lee & Yau, 2020; Tomoko Wakabayashi et al., 2019).

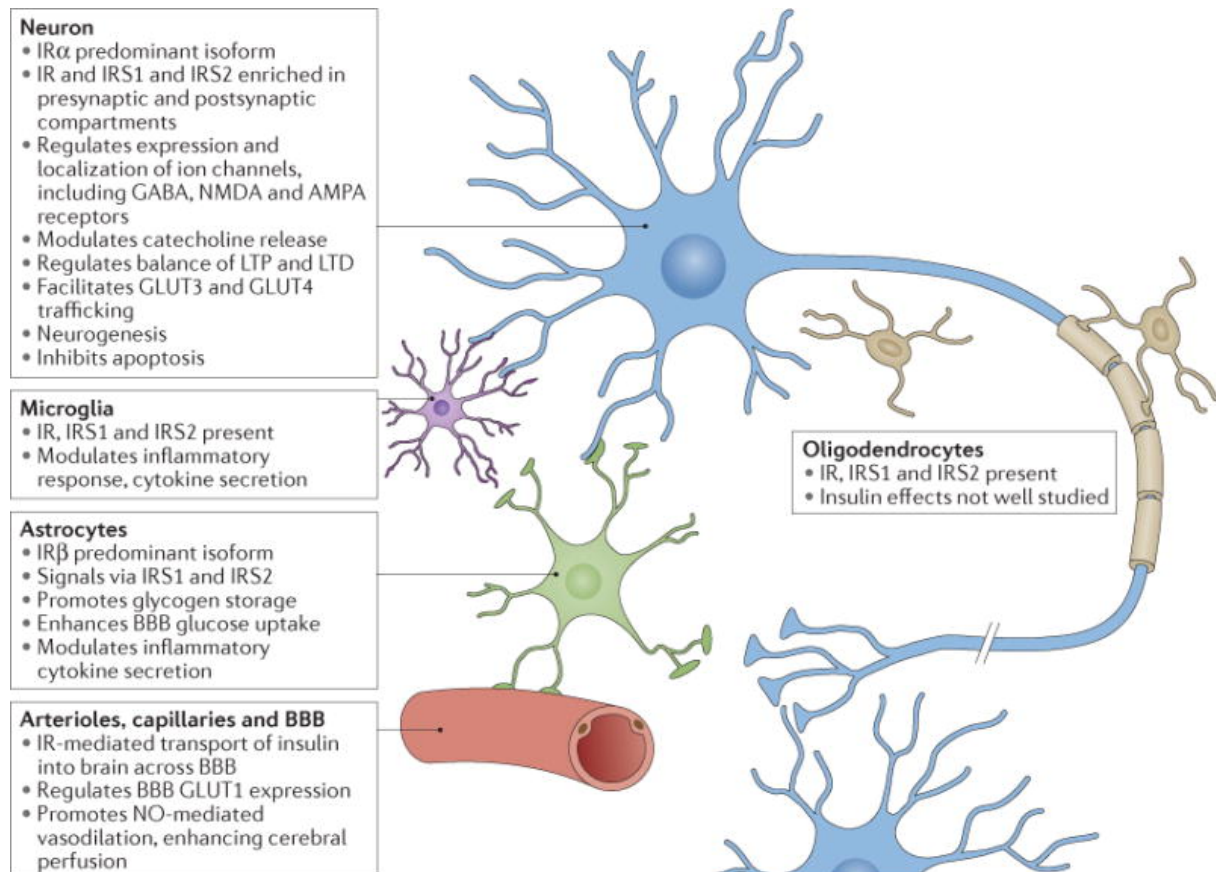


**Figure 3: Suggested effects of insulin on major cell types of the brain.**

Annotations: GABA; Gamma aminobutyric acid, NMDA; N-methyl-d-aspartate, AMPA;  $\alpha$ -amino-3-hydroxy-5-methyl-4-isoxazole propionic acid, BBB; blood-brain barrier, GLUT; glucose transporter type protein, IR; insulin receptor, IRS; insulin receptor substrate, LTD; long-term depression, LTP; long-term potentiation, NO; nitric oxide. Retrieved from: (Arnold et al., 2018).

### Long-term potentiation and long-term depression

Long-term potentiation (LTP) consists of cellular mechanisms enhancing learning and memory by strengthening synaptic plasticity. When the synapses reach a level of “maximum efficiency” (challenging to encode new information), long-term depression (LTD) selectively decrease the “synaptic efficiency” of the synapses which have been poorly stimulated for longer periods. This is to compensate and make the synaptic strengthening useful (Purves D,

Augustine GJ, Fitzpatrick D, & et al., 2001). LTP impairment are linked to learning and memory deficits in AD and diabetic rodents (Kimura & Ohno, 2009; T. H. Lee & Yau, 2020).

### **Insulin signaling and resistance**

Impairment in brain insulin signaling has been reported to worsen the pathology of AD, particularly increasing neuroinflammation (Steen et al., 2005).

Insulin signaling is initiated by insulin binding to its receptors, which belongs to the receptor tyrosine kinase superfamily. The insulin receptor (IR) is located on the membranes of target cells and is a homodimer consisting of two extracellular  $\alpha$ -subunits and two intracellular  $\beta$ -subunits (De Meyts, 2000). When insulin binds the extracellular  $\alpha$ -subunits, a dimerization and autophosphorylation of the  $\beta$ -subunits occur, leading to activation of its kinase activity (Arnold et al., 2018). IRS1 and IRS2 become phosphorylated, they bind and activate intracellular signaling molecules, such as phosphoinositide 3-kinase (PI3K) complex, which further activates AKT and further downstream effects (like translocation of GLUT4). Insulin-binding to IR also stimulates the mitogen-activated protein kinase (MAPK) pathway (DeFronzo et al., 2015).

Insulin is released from pancreatic  $\beta$ -cells as a result of increased levels of blood glucose and substances such as acetylcholine, amino acids, cholecystokinin and incretin hormones (Röder, Wu, Liu, & Han, 2016). An important role of insulin is to stimulate glucose uptake by the translocation of glucose transporter type 4 (GLUT4) protein (particularly in skeletal muscle). Furthermore, insulin inhibits gluconeogenesis and glucose release by the liver, stimulates lipogenesis and inhibits lipolysis of stored fat in the adipose tissue and, in addition, contributes to cellular growth and metabolic availability of various substances important for the brain (DeFronzo et al., 2015; Sears & Perry, 2015). In the CNS, insulin is involved in energy metabolism, regulating eating behavior, neuronal survival and modulating synaptic function. Hence, insulin is important to maintain cognitive function (T. Wakabayashi et al., 2019).

Insulin resistance in obesity is mainly linked to the PI3K/AKT pathway (Huang, Liu, Guo, & Su, 2018; Röder et al., 2016). The causes of insulin resistance are multifactorial, although mechanisms are usually linked with increased serine phosphorylation of IRS proteins, inhibiting tyrosine phosphorylation. Serine phosphorylation may also increase IRS degradation contributing to insulin resistance. Lipid accumulation and inflammation are some

of the factors leading to serine phosphorylation of IRS proteins, inhibition of tyrosine phosphorylation, and hence, the intracellular signaling molecules and effects from insulin (DeFronzo et al., 2015).

### **Insulin resistance in the brain**

The brain has high energy demands, and its primary energy source is glucose from the circulatory blood system (Nave, Tzvetanova, & Schirmeier, 2017). AD-associated brain insulin resistance is putative to resemble the one in the peripheral organs in T2DM, therefore some have proposed to classify AD as “type 3 diabetes” (Blázquez et al., 2014; T. H. Lee & Yau, 2020). Hippocampus is one of the areas in the brain with the highest insulin receptor density (H. J. Lee et al., 2018; Spinelli, Fusco, & Grassi, 2019). Insulin resistance in the brain may lead to impaired insulin signaling and reduce insulin transport through the BBB (Arnold et al., 2018; H. J. Lee et al., 2018). Interestingly, intranasal administration of insulin has been tested in clinical trials for both AD (Craft et al., 2012) and T2DM (H. Zhang et al., 2015), showing that intranasal insulin may briefly improve impaired cognitive function. These observations support that T2DM may cause a decreased cognitive function in AD due to impaired brain insulin signaling (T. Wakabayashi et al., 2019).

A study using asymptomatic, late middle-aged adults, tested the interaction between insulin resistance and glycemic status using PET imaging and found that systemic insulin resistance was associated with brain A $\beta$  deposition (Willette et al., 2015). But whether insulin resistance contributes to the AD plaque pathology remains unknown and require more research.

### **Effects of insulin in glial cells**

Astrocytes are important to maintain the metabolic demand of the brain. They are located surrounding nerve cells and increases their glucose uptake via glucose transporter type 1 (GLUT1) once the neurons require more energy. The astrocytes contribute with lactate (converted from glucose) during high energy demands to fuel oxidative phosphorylation and generate ATP, and during hypoglycemia (Arnold et al., 2018; Liu, MacKenzie, Putluri, Maletić-Savatić, & Bellen, 2017; Wender et al., 2000). Hyperinsulinemia may affect the net flux of lactate to the brain, hence affect the brain energy metabolism (Arnold et al., 2018). Research has found IR and IRS1 expressed in astrocytes and microglia, and insulin contributes to an inflammatory response where it can increase secretion of inflammatory cytokines (Spielman, Bahniwal, Little, Walker, & Klegeris, 2015).



## **Inflammation in adipose tissue**

Lipid dysregulation is considered a metabolic feature of AD pathology (Farmer, Walsh, Kluemper, & Johnson, 2020). The systemic inflammation in T2DM contributes to insulin resistance and a condition of chronic inflammation. Chronic inflammation in adipose tissue could trigger neuroinflammation and impaired neuroplasticity in the hippocampus under diabetic and obese conditions (T. H. Lee & Yau, 2020). Pro-inflammatory cytokines, like tumor necrosis factor (TNF) and interleukin-6 (IL-6), other inflammatory cells and the activation of M1 macrophages are present in adipose tissue. M1 macrophages (“classic macrophages”) are pro-inflammatory and the infiltration stimulates lipolysis (DeFronzo et al., 2015).

## **1.4 Neuroinflammation**

An inflammatory response within the CNS is referred to as neuroinflammation (DiSabato, Quan, & Godbout, 2016). Neuroinflammation can develop in response to brain-intrinsic mechanism that cause dyshomeostasis but can also be induced from the outside. Metabolic- and/or inflammatory conditions may represent brain-extrinsic causes of neuroinflammation (Ransohoff, Schafer, Vincent, Blachère, & Bar-Or, 2015). Neuroinflammation contributes to normal brain development but also include mechanisms for neuropathological processes and depending on the intensity and duration of the inflammation the responses can be helpful or harmful (DiSabato et al., 2016; Ransohoff et al., 2015). Key reactive cells within the CNS which are associated with neuroinflammation includes astrocytes, and microglia. Both cell types are in response to neuroinflammation and contribute to the regulation of the inflammatory response. Infiltrating myeloid cells like granulocytes, monocytes, macrophages and dendritic cells may also contribute to neuroinflammation, but their access to the brain is limited as long as the BBB is intact (Ransohoff et al., 2015).

### **1.4.1 Microglia**

Microglia is the core immune cells in the CNS and have a fundamental role in the maintenance of brain homeostasis. Microglia represent the CNS-resident myeloid cells (Q. Li & Barres, 2018). Microglia obtain a ramified morphology under physiological conditions (figure 4). By having fine processes (branches) covering their micro-environment the cells can control their surroundings and have interactions with neuronal cells (Boche, Perry, & Nicoll,

2013; Wake, Moorhouse, Jinno, Kohsaka, & Nabekura, 2009). The ramified morphology is not permanent as they have significant structural changes when performing any of their activities (Walker et al., 2014). The structures and changes in morphology is similar between mice and humans, creating comparable results between species in research (Torres-Platas et al., 2014).

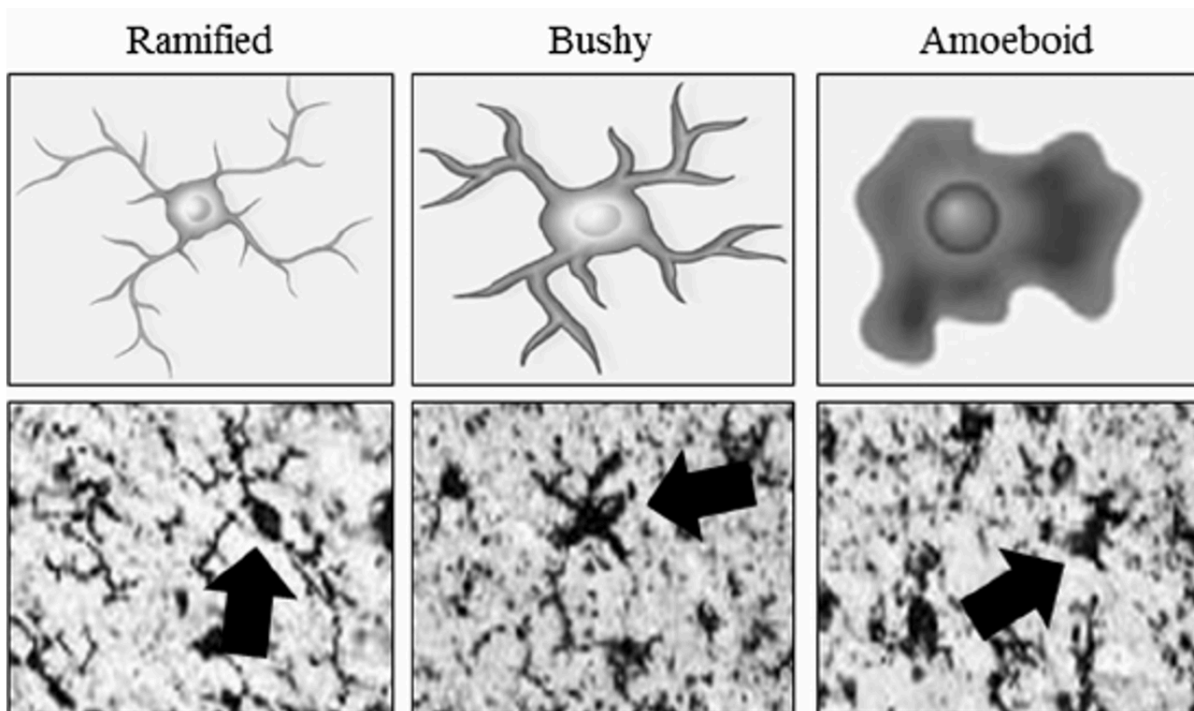


**Figure 4: Morphological changes in microglial.** Schematic and microscopy images of human brain microglia. “Ramified” are microglia in resting state, having long and many processes and a small soma. “Bushy” represents an intermediate activation characterized by retracted, thicker processes and a larger soma than in the resting state. “Amoeboid” represents activated microglia, having an enlarged soma with less and shorter processes. Retrieved from: (Crews & Vetreno, 2015).

### 1.4.2 Microglia activation

The term, microglia activation, is used to describe a functional activation of microglia cells, including the change in morphological structure (Heppner et al., 2015). Under pathological conditions, such as inflammation or altered neuronal function, microglia become activated, proliferate and change towards a more macrophage-like morphology (Wang, Tan, Yu, & Tan, 2015).

Microglia activation occurs along a continuum; the two extreme microglia phenotypes are denoted M1 and M2. The M1 microglia are in a pro-inflammatory state while the M2 microglia represent an anti-inflammatory phenotype. M1 microglia produce pro-inflammatory cytokines, such as interleukin 1 $\beta$  (IL-1 $\beta$ ), interleukin 6 (IL-6), tumor necrosis factor  $\alpha$  (TNF-

$\alpha$ ), interleukin-12 (IL-12), and free radicals, including reactive oxygen species (ROS) (Wang et al., 2015). The M1 activated phenotype of microglia is considered a “classical activation” and is important in the defense against pathogens and tumor cells. The M2 activated microglia produce lower levels of pro-inflammatory cytokines and higher levels of anti-inflammatory cytokines, such as IL-4, IL-13 and TGF- $\beta$ . M2 microglia are known as an “alternative activation” and promote tissue repair and remodeling, and angiogenesis (Boche et al., 2013; Mosser & Edwards, 2008). Research in AD mouse models has shown that both M1 and M2 microglia may be increased in AD, but the M1 microglia appear to be the ones associated with an increase in IL-1 $\beta$ , TNF- $\alpha$ , IL-6 and cytotoxicity (Wang et al., 2015).

### **1.4.3 Neuroinflammation in Alzheimer disease**

**Amyloid cascade hypothesis:** When Alois Alzheimer first described AD in 1906, he described three key pathological hallmarks: neuronal loss, protein aggregations, and accumulation of lipids. The proteinopathy has attracted a lot of interest since then, and the presence of amyloid plaques are currently the main diagnostic marker of AD (Hippius & Neundörfer, 2003; Molinuevo et al., 2018). Consequently, the amyloid cascaded hypothesis has guided the research focus. According to the amyloid hypothesis, extracellular accumulation and deposition of A $\beta$  peptides form A $\beta$  plaques (Hardy & Higgins, 1992; Heppner et al., 2015; Yankner, 1996). A $\beta$  is produced by a two-step cleavage of the amyloid precursor protein (APP), first by beta-site APP-cleaving enzyme (BACE-1), then by  $\gamma$ -secretase (as illustrated in figure 5). The main proteolytic products of APP are A $\beta$ 40 and A $\beta$ 42 (Ohno et al., 2007).

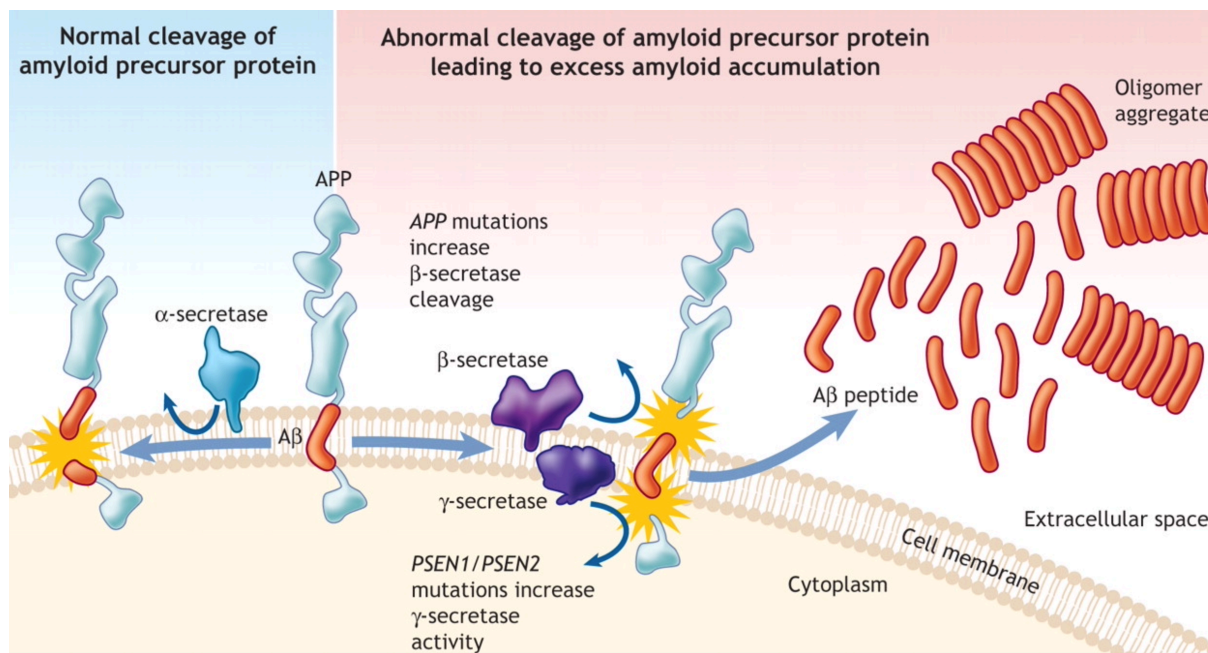


**Figure 5: Formation of Amyloid- $\beta$  plaque by APP-cleaving.**

A normal cleavage of amyloid precursor protein (APP) is illustrated on the blue side, resulting in no amyloid- $\beta$  peptides. An abnormal cleavage of APP is illustrated on the red side. First, the  $\beta$ -secretase cleaves the APP, creating a membrane-bound fragment and a secreted APP domain. Then the  $\gamma$ -secretase cleaves the membrane-bound fragment, which is not a precise cleaving, creating a series of A $\beta$  peptides. The proteolytic products aggregate in the extracellular space and cause the formation of amyloid- $\beta$  plaque. Retrieved from:

<https://jonlieffmd.com/wp-content/uploads/2013/11/Excell-amyloid-.jpg>

The A $\beta$ 42 is the most prone peptide to aggregate, and the A $\beta$  peptides cause the formation of A $\beta$  plaques. These plaques generate a cascade of oxidative stress in neurons, which may contribute to the disruptions of kinase and phosphatase activity, which in turn may lead to hyperphosphorylation of tau proteins and further to the formation of neurofibrillary tangles (Oakley et al., 2006; Ohno et al., 2007). The hypothesis states that the cascade starting with A $\beta$ , leading to synaptic deficiency and neuronal loss, is the central event and the main driver of the pathogenesis of AD (Maia & Sousa, 2019; Oakley et al., 2006). During recent years, the unique importance of amyloid in AD has been challenged. Amyloid pathology is still regarded a key characteristic of AD, but whether it is the main driver of AD pathology is under investigation. In line with this uncertainty, a human monoclonal amyloid antibody, aducanumab, has been shown to cause a clear reduction in A $\beta$  aggregation (Cummings et al., 2021), yet whether the cognitive performance of the patients is enhanced, remains a question of debate. Aducanumab is currently being considered for approval by the FDA but due to the uncertainty regarding the clinical effect, the final decision by FDA has been delayed and is now expected in June 2021 (Campbell, 2021). Our understanding of when the immune system

plays a role in the course of AD, has changes as well. The amyloid cascade hypothesis suggests that the immune response occurs as a consequence of A $\beta$  accumulation, but correlative studies indicate a much earlier activation of the immune response (Heppner et al., 2015; Kinney et al., 2018).

**Neuroinflammatory mechanisms in AD:** The inflammatory reaction in AD pathogenesis is primarily driven by microglia and escalates with progression of the disease (Wang et al., 2015). Microglia are important for homeostasis, synaptic plasticity, and synaptic remodeling (Wake et al., 2009). These cells can sense pathological changes within tissues as “danger signals”, which in AD comprise protein aggregates of A $\beta$  (Heppner et al., 2015). Microglial activation may be a key underlying factor for the impaired synaptic plasticity and cognitive function observed in response to obesity-associated neuroinflammation (Erion et al., 2014). However, the mechanisms for how inflammation in adipose tissue in obesity leads to neuroinflammation and neurodegeneration is still unclear (T. H. Lee & Yau, 2020).

Microglia activation in early stages of AD can contribute to A $\beta$  clearance via scavenger receptors (SRs) and phagocytosis (Yang et al., 2011). With increased age and disease progression, microglia function and the prevalence of the neuroprotective M2 phenotype decrease, leading to a more classically activated M1 microglia (Marschallinger et al., 2020; Wang et al., 2015). Microglia express several receptors which can bind A $\beta$  peptides, such as CD36, SRs and toll-like receptors (TLRs) (Du Yan et al., 1997; Heppner et al., 2015; Wang et al., 2015). Binding of A $\beta$  to some of these receptors generate production of proinflammatory cytokines and neuroinflammation. This creates a vicious circle of microglia activation and A $\beta$  clearance via SRs, A $\beta$  stimulation of receptors, enhanced neuroinflammation and A $\beta$  accumulation (Carty & Bowie, 2011; Yang et al., 2011; Zilka et al., 2012). The hypothesis if this circle is that microglia sense the extracellular accumulations of soluble A $\beta$ , resulting in M1 activated phenotype. Fibrillar A $\beta$  bind receptors expressed on microglia creating intracellular signaling cascades, such as p38 MAPK, and production of pro-inflammatory cytokines and chemokines, such as TNF- $\alpha$ , IL-12, and ROS, and reduce phagocytic capacity. This influences the immune system further, recruiting several microglia, and more pro-inflammatory mediators (Heppner et al., 2015; Reed-Geaghan, Savage, Hise, & Landreth, 2009). The A $\beta$  fibrils keeps binding the receptors and the inflammation continue to increase. TNF $\alpha$ , IL-1 $\beta$  and IL-6 have also been suggested to worsen hyperphosphorylation of tau, hence contribute to formation of neurofibrillary tangles (Dionisio-Santos, Olschowka, &

O'Banion, 2019). This is only a theory, and whether the overexpression of cytokines initiates AD or arise as a result from neurodegeneration remains unclear.

#### **1.4.4 Lipid droplets**

Lipid droplets (LD) are described as lipid-storing organelles which structurally have a neutral lipid core surrounded by a monolayer of phospholipids and surface proteins (Penno, Hackenbroich, & Thiele, 2013). LD are formed by budding off from the endoplasmic reticulum (ER), and the surface layer of phospholipids are therefore derived from the outer membrane of the ER (Farmer et al., 2020). Organelles are defined as intracellular structures having a specific function (William Gahl & M.D., 2021). LD with stored lipids, such as triacylglycerols (TAGs) and cholesteryl esters, provides substrates for energy metabolism and substrates for membrane formation (Walther & Farese, 2012). LD are mostly described in liver, adipose tissues and skeletal muscle where they respond to different signals, including changes in nutrient fluctuations, oxidative stress or other forms of microenvironmental stress to alter the trafficking, storage, or use of lipids in the cell (Farese & Walther, 2009; Itabe, Yamaguchi, Nimura, & Sasabe, 2017; Jarc & Petan, 2020; Murphy, 2001). Despite their simple structure, LD number, size and composition of core lipids and surface lipids and -proteins can vary in individual cells and tissue (Daemen et al., 2018; Krahmer, Farese, & Walther, 2013). For instance, LD in white adipocytes can have diameters up to 100  $\mu\text{m}$  and quickly grow during adipogenesis (Walther & Farese, 2012). Under physiological condition, LD are present in limited numbers and small sizes, however in the presence of excessive lipid accumulation in fatty livers, LD number and size seems to increase (Itabe et al., 2017). The fact that LD are dynamic organelles which have an active role in the regulation of cellular functions and health has emerged over the last ~10 years in peripheral cells. The presence and roles of LD in brain cells is largely undescribed. Research in *Drosophila* (Liu et al., 2015) and mice (Marschallinger et al., 2020; Shimabukuro et al., 2016) has reported LD in the brain, although their origin and functional mechanism in the brain is poorly understood. In the *Drosophila* model, LD were present in cells with elevated levels of ROS, and accumulation of LD were suggested as an early biomarker for neurodegeneration (Liu et al., 2015).

#### **Lipid droplet accumulation in microglia**

Abnormal lipid accumulations have for a long time been associated with immune dysfunction in myeloid cells, much due to the discovery of the “foamy macrophages” contributing to

atherosclerotic lesions (Fowler, Mayer, & Greenspan, 1985). Myeloid cells form LD, containing inflammatory cytokines and eicosanoids, in the presence of inflammation and stress (Marschallinger et al., 2020). The decreased function of the CNS-myeloid cell, the microglia, occurring with age, as well as its change to a more pro-inflammatory phenotype remains poorly understood (Liu et al., 2017). Interestingly, studies show LD accumulation in microglia cells together with high levels of ROS (Liu et al., 2015; Marschallinger et al., 2020).

A study chemically induced high levels of ROS in mice for 8 constitutive days, and the immunohistochemical analyses revealed significant LD accumulation in the glial cells in response to this treatment (Liu et al., 2017). This indicates that high levels of ROS could be causative for the LD accumulation. The very reactive ROS are destructive for the brain tissue, causing damage to all cell components, proteins, lipids and DNA (R. Li, Jia, & Trush, 2016). Elevated levels of ROS have been suggested to induce the production of lipids in neurons; these lipids are then transported to glia cells where they contribute to formation of LD (Liu et al., 2017; Nave et al., 2017). Apolipoproteins contribute to the transport of fatty acids to glia, and in the presence of high levels of ROS and decreased levels of apolipoprotein, a reduction of LD accumulation in glia occurred in *Drosophila* flies (Liu et al., 2017). This is fascinating, due to the role of APOE  $\epsilon$ 4 as a genetic risk factor for late-onset AD (Farmer et al., 2020). Interestingly, ApoE4-containing lipoproteins are less efficient at delivering lipotoxic products to glia than lipoproteins containing other ApoE variants (Farmer, Kluemper, & Johnson, 2019).

LD is associated with inflammation in peripheral myeloid cells (Walther & Farese, 2012) and have grown an interest as a possible mechanism of neurodegenerative diseases (Farmer et al., 2020; Marschallinger et al., 2020).

## **1.5 Exercise and lipid droplets**

Physical inactivity and obesity are important risk factors for both AD and T2DM (Kahn et al., 2014; Reitz & Mayeux, 2014). Physical exercise is reported to protect against T2DM (Balducci et al., 2010). Also, physical activity is considered an effective approach in both the prevention and treatment of T2DM (Sanz, Gautier, & Hanaire, 2010). Exercise is reported to

improve learning and hippocampal neurogenesis, which is especially important in the aging brain (Fordyce & Farrar, 1991; van Praag, Shubert, Zhao, & Gage, 2005).

Exercise also regulate LD dynamics in skeletal muscle: Exercise can induce and increase the lipid storage within LD in skeletal muscle, which reflects an increased LD number and changed morphology (X. Li et al., 2019). This is interesting, as the LD size and accumulation in obese T2DM patients is shown to have a positive correlation with insulin resistance. However, trained athletes which have a high amount of intramyocellular lipids in LD are very insulin sensitive. This is called the “athletes’ paradox” (Daemen et al., 2018; X. Li et al., 2019).

Exercised athletes have a high oxidative capacity during exercise, while people with T2DM have compromised fat oxidation (Gemink, Schrauwen, & Hesselink, 2020). A study of obese people (non-diabetic) during a dietary and exercise intervention showed a reduction in LD size in skeletal muscle, in addition to a positive change in insulin sensitivity (He, Goodpaster, & Kelley, 2004). T2DM patients shown to have larger, but fewer LD in skeletal muscles compared to exercised individuals (Daemen et al., 2018). Research indicates that LD morphology in T2DM patients changes towards an athlete-like phenotype during endurance exercise (Gemink et al., 2020). However, the effect of exercise on LD in the brain is yet to be studied.

## **1.6 Using mice as models for type 2 diabetes mellitus and Alzheimer’s disease**

The absence of *in vitro* models capable of modelling the complex physiology of the brain makes the use of animal models necessary to study microglia activation and lipid droplets, as brain sections are needed for immunohistochemistry (IHC).

The *db/db* mouse model is a popular animal model for research in T2DM (Yeadon, 2015). These mice have a mutation in the *Lepr* gene, encoding the leptin receptor (The Jackson Laboratory, 2021b). Leptin is a hormone produced and secreted by adipose tissue, depending on the amount of body fat (Y. Zhang et al., 1994). Leptin causes reduced food intake and body weight; hence a non-functional leptin receptor leads to an increased appetite and obese phenotype (Dornbush & Aeddula, 2021). The 5xFAD model is a transgenic animal model



with five human AD-linked mutations in the mice, creating a severe Alzheimer's model with an early developed AD pathology (A $\beta$  plaque observation and gliosis around 2 months of age) (Oakley et al., 2006).

## 2 Aims of the study

This study aims to investigate the potential effect of microglia and the accumulation of LD in the brain of mice with T2DM or AD. In this study, we hypothesize that T2DM induces pathological accumulation of lipids in LD in the microglia towards a less healthy phenotype and that this resembles what is found in a mouse model of AD. In addition, the effects of exercise on spatial learning and memory are investigated in diabetic mice. In light of this, we seek to answer the following research questions:

1. Are microglia activation and LD number and size in the brain altered in the 5xFAD model of AD compared to in control mice?
2. Does T2DM affect microglia activation and LD number and size in the brain towards an AD-like phenotype?
3. Does high-intensity interval exercise affect cognitive function in the mouse brain and mice with T2DM?

## 3 Materials and methods

### 3.1 Chemicals and reagents

*Table 1: All the chemicals and reagents used in the study*

<b>Product</b>	<b>Producent</b>
4,6-diamidino-2-phenylindole (DAPI)	Sigma-Aldrich, USA
Alexa Fluor™ 594 goat anti-mouse IgG	Invitrogen, USA
Anti Iba1, Rabbit pAb (for Immunocytochemistry)	FUJIFILM Wako Pure Chemical Corporation, Japan
4,4-Difluoro-1,3,5,7,8-Pentamethyl-4-Bora-3a,4a-Diaza-s-Indacene (BODIPY® 493/503)	Invitrogen, USA
Column Prep Solution	Sigma-Aldrich, USA
Distilled Water DNase/RNase Free	Invitrogen, USA
Dimethyl Sulfoxide	Sigma-Aldrich, USA
Elute Buffer	Sigma-Aldrich, USA
Ethanol	Antibac, Norway
Gel Loading Dye Purple (6X)	New England BioLabs, USA
GelRed® Nucleic Acid Stain, 10,000X in water	Biotium, USA
GenElute Mammalian Genomic DNA Miniprep Kit (G1N350/G1N70)	Sigma-Aldrich, USA
GeneRuler 100 bp Plus DNA Ladder	Thermo Scientific, USA
GFAP, Mouse mAb	Cell Signaling Technology, Netherlands
Goat anti-Rabbit IgG, Superclonal™, Alexa Fluor 647	Invitrogen, India
Isoflurane Baxter	Baxter, USA
Lysis Solution C	Sigma-Aldrich, USA
Lysis Solution T	Sigma-Aldrich, USA
Newborn Calf Serum (NCS)	Invitrogen, USA
OneTaq® Hot Start 2X Master Mix with Standard Buffer	New England BioLabs, USA

Paraformaldehyde (PFA)	Sigma-Aldrich, USA
ProLong Gold	Invitrogen, USA
Proteinase K	Sigma-Aldrich, USA
Sodium acetate (NaAc)	Sigma-Aldrich, USA
Wash Solution	Sigma-Aldrich, USA
ZRF mix	KPM, UiO

## 3.2 Animals

All experiments in this study have been conducted according to a project description approved by the Norwegian Food Safety Authority (FOTS ID: 21282). The animal model chosen for this study were mice originating from the strain, B6.BKS(D)-*Lepr*<sup>db</sup>/J, JAX Stock No: 000697. These mice harbor a point mutation (g→t) in the *Lepr* gene encoding the leptin receptor (*Lepr*). The mutation leads to premature splicing and inclusion of parts from the previous intron, giving rise to a non-functional receptor. This further cause these animals to eat excessively, resulting in an obese phenotype at 3-4 weeks of age (Coleman, 1978; The Jackson Laboratory, 2021b). The gene is recessive and will therefore only lead to a phenotype if the animal is homozygote (*db/db*). The heterozygote (*db/+*) littermates were used as controls (The Jackson Laboratory, 2021b). The phenotype for *db/db* includes weight gain, rise in blood sugar levels and increased insulin resistance, consequently causing the development of Type 2 Diabetes Mellitus (T2DM). Since *db/db* mice are infertile, only *db/+* mice could be used for breeding, and all mice were genotyped prior to the experiment; only *db/+* and *db/db* mice were included in the study (Peng et al., 2018).

To analyze any microglia activation and lipid droplet-containing microglia in mice with Alzheimer's disease, a transgenic (tg) line of mice was used, originating from the strain; B6SJL-Tg(APPswFlon,PSEN1\*M146L\*L286V)6799Vas/Mmjax, JAX Stock No: 034840, also known as 5xFAD. This animal model harbor three mutations in the gene encoding the human amyloid precursor protein (APP): the Swedish (K670N/M671L), Florida (I716V), and London (V717I) mutations, and two mutations in the gene encoding the human presenilin 1 (PS1): the M146L and L286V mutations (The Jackson Laboratory, 2021c). Thus, a total of five mutations resulting in familial Alzheimer's disease (FAD) and hence the name 5xFAD. Wild type (wt) mice were used as controls (The Jackson Laboratory, 2021c). These mice were obtained through a collaboration with Prof. Farrukh A. Chaudhry at the Faculty of Medicine, UiO.

The transgenic mice develop amyloid plaque pathology similar to that found in AD (Oakley et al., 2006). APP is cleaved by secretases encoded by presenilin, resulting in amyloid- $\beta$  formation. Amyloid- $\beta$  42 (A $\beta$ 42) is one of the proteolytic products of APP and is a toxic form of  $\beta$ -amyloid (Yankner, 1996). Mutant APP and PS1 result in increased production of A $\beta$ 42 and plaque development causing FAD. Because of the total of five mutations, the plaque

development is accelerated and the cerebral A $\beta$ 42 levels rapidly accumulate. The 5xFAD mice represent one of the most early-onset and aggressive amyloid mouse models, with A $\beta$ 42 accumulation already at 1.5 months of age and amyloid deposition and gliosis at 2 months of age. The 5xFAD mice acquire massive A $\beta$ 42 burdens, amyloid plaques, gliosis, reduced synaptic markers, memory impairment (observed in Y-maze) and neuron loss (Oakley et al., 2006; Ohno et al., 2006; Ohno et al., 2007). The neuropathology and phenotype characterization of 5xFAD mice are illustrated in figure 6.

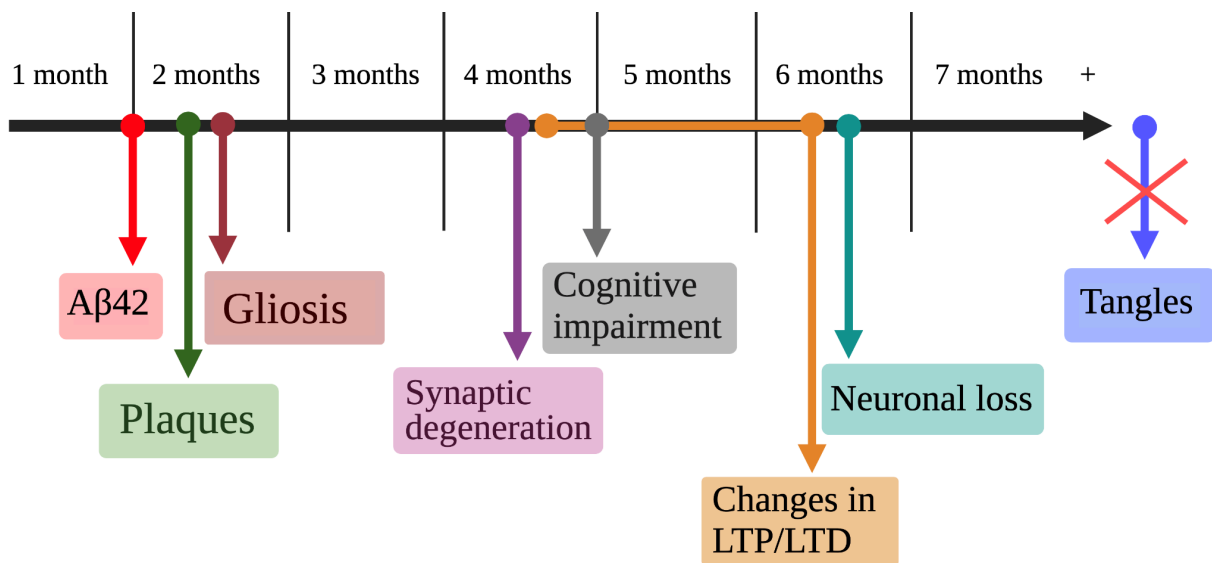


**Figure 6: Phenotype characterization in 5xFAD transgenic mice.**

High levels of intraneuronal A $\beta$ 42 (red) accumulates already around 1.5 months of age in an aggregated form within the neuron soma and neurites. This occurs before plaques (green) start to format 2 months. Plaque formation starts in the subiculum and the deep cortical layers and increases rapidly with age. By 6 months, plaques are found throughout the hippocampus and cortex. At 2 months of age gliosis (dark red) occurs, giving an indication of injury on the brain. By 4 months of age synaptic degeneration (purple) begins. This is indicated by the decline of synaptophysin, a presynaptic marker. Most other synaptic markers decline by 9 months of age. Cognitive impairment (grey) is starting to become evident at approximately 4 to 5 months of age as evident by a reduction in spatial working memory (showed in Y-maze behavior test). Between 4 and 6 months of age the basal synaptic transmission, long-term potentiation (LTP) and long-term depression (LTD) (orange) in the hippocampus begin to deteriorate. At 6 months of age, the loss of neurons (turquoise) begins in the subiculum and cortical layer V (the areas with the most severe amyloid accumulation). A reduction in the number of cholinergic neurons has been observed in the basal forebrain at 6 months of age. The 5xFAD model is an amyloid model, and hence develop amyloid plaque pathology, while tau tangles (blue) are absent (indicated by the red cross).

Breeding and stalling of all the *db/db*, *db/+*, 5xFAD and wt mice took place in the Department of Comparative Medicine, Institute of Basic Medical Sciences, UiO. The *db/db* and *db/+* animals were 9-11 weeks of age at the experiment start, which translates to adult age in humans. They were 17-19 weeks at the end of the experiment. The 5xFAD and wt mice were 39-49 weeks of age when they were euthanized. The animals were housed in standard

GreenLine cages (Sealsafe Plus GM500, Tecniplast Group, USA) with 2 to 8 mice in each cage and separated by sex. The room for housing was light-regulated with a 12:12 hour program; 12 hours of light and 12 hours of darkness. The animals had unlimited access to food and water *ad libitum* and were observed daily by the certified personnel working at the animal facility. If any physical abnormalities, or signs of distress or pain (piloerection, weight loss, lack of grooming, wounds, etc.) occurred, the animals were considered for euthanasia. The mice included in the exercise intervention were weekly weighed during the exercise regime to ensure that no severe weight loss occurred. Handling of the animals were restricted to FELASA (Federation of Laboratory Animal Science Associations Category) certified personnel.

### 3.3 Genotyping

In order to plan breeding and secure an adequate number of animals in each experimental group, the genotype of the animals was determined. Since homozygous *db/db* are infertile, heterozygotes *db/+* were used for the breeding of diabetic mice (Coleman, 1978; Peng et al., 2018). Genotyping is a method used to determine DNA sequences and clarify genetic differences by comparing the DNA sequence to a reference sequence or another sample.

In this study, genotyping was performed by firstly isolating DNA from the tissue samples acquired from ear punch identification of the mice. After isolation, the DNA fragment of interest was amplified by using specific primer in PCR. After DNA amplification by PCR, gel electrophoresis was performed to separate the DNA sequences based on the molecular weight (which is proportional to the number of base pairs). The results were used to determine whether each mouse was wildtype, heterozygote or homozygote of the *Lepr* mutation. Genotyping of the 5xFAD mice was performed by the Chaudhry group before this master project was started. The following therefore describes the genotyping procedure for the B6.BKS(D)-*Lepr<sup>db</sup>/J*, JAX Stock No: 000697 strain.

#### 3.3.1 Extraction and isolation of genomic DNA

##### DNA isolation

Genomic DNA was extracted using the Sigma GenElute Mammalian Genomic DNA Miniprep Kit (G1N350-1KT and G1N70-1KT, Sigma-Aldrich, USA). The kit was based on

isolation of the genetic material by alkaline lysis of tissues and cells, followed by running the samples through a silica-based column which specifically binds genomic DNA. The kit contains the necessary reagents to isolate the DNA, as shown in table 2.

**Table 2:** Reagents in the Sigma GenElute Mammalian Genomic DNA Miniprep kit used for isolating DNA in this study.

Reagents
Lysis Solution T
Proteinase K
Lysis Solution C
Column Preparation Solution
Wash Solution Concentrate
Elution Solution (10 mM Tris-HCl, 0.5 mM EDTA, pH 9.0)
GenElute™ Miniprep Binding Columns in tubes
Collection Tubes, 2.0 mL
3 M sodium acetate (NaAc)

For the ear biopsies to be lysed, they were placed in designated 1.5 mL eppendorf tubes with 180  $\mu$ L Lysis Solution T and 20  $\mu$ L Proteinase K (dissolved in DNase and RNase free water to a 20 mg/mL stock solution). To ensure that the tissue samples were fully covered by the solution, the tubes were vortexed (Minishaker MS2, IKA, Germany). The tubes were then placed in a 55 °C heating block (Grant Boekel BBD, Boekel Scientific, USA) until the tissues was completely dissolved, approximately 2 hours. After tissue digestion by Lysis Solution T and Proteinase K, 200  $\mu$ L of Lysis Solution C was added for cell lysis. A homogeneous solution was essential for efficient lysis; thus, the samples were vortexed (about 15 seconds) before being placed in a 70 °C heat block for 10 minutes. The chaotropic salt-containing solution ensures denaturation of macromolecules, hence exposing the genomic DNA for further extraction. Proteinase K ensures that DNA was not degraded by nucleases during the isolation. Proteinase K is a serine protease that hydrolyzes a variety of peptide bonds and therefore inactivates nucleases (New England BioLabs, 2021b; Sigma-Aldrich, 2021c). To prepare DNA for binding to the silica membrane, 200  $\mu$ L of 95-100 % ethanol was added and mixed by vortexing for 10 seconds (Sigma-Aldrich, 2021b).



Nucleic acid binding columns were placed in collection tubes. Binding columns were activated by adding 500  $\mu\text{L}$  of Column Preparation Solution, the tubes were then centrifuged for 1 minute (Heraeus Pico 17 Microcentrifuge, Thermo Fisher Scientific, USA), and the filtered solution discarded. All centrifuge steps were conducted at 13 000 revolutions per minute (rpm) at room temperature. With a  $\text{pH} < 7$  and positive ions in the solution, Column Preparation Solution maximizes the binding of DNA to the silica, giving more consistent yields of DNA (Sigma-Aldrich, 2021b). Samples were then transferred to the columns and centrifuged for 2 minutes. In this step, DNA bound to the column while the rest of the cell content in the solution was filtered and discarded. To remove contaminants, the samples were washed twice with 500  $\mu\text{L}$  Wash Solution diluted 1:4 with 95-100 % ethanol, centrifuged for 1 minute and the flowthrough liquid was discarded after each washing step. An additional centrifugation step for 3 minutes (without solutions) was performed to remove the remaining Wash Solution, ethanol and any unwanted particles. The collection tubes with flowthrough solutions were discarded and the binding columns were placed in new 2 mL collection tubes.

To the center of the column, 100  $\mu\text{L}$  of Elution Solution (10 mM Tris-HCl, 0.5 mM EDTA,  $\text{pH} 9.0$ ) was added, and after 1 minute, the column was centrifuged for 1 minute at 13 000 rpm at room temperature. The high  $\text{pH}$  and low salt content of the solution caused the bonds between the silica column and DNA to break. After DNA elution, columns were discarded, and the DNA isolate were stored at  $-20\text{ }^\circ\text{C}$ .

### 3.3.2 Precipitation of DNA

To enhance the concentration of DNA in the isolate (which was normally around 2-8  $\text{ng}/\mu\text{L}$ ), DNA precipitation was performed. This was done by adding 3M Na-acetate (1/10 of the final volume) and 2.5x volume of ice-cold 95-100 % ethanol. The added volumes are shown in Table 3. For the DNA to precipitate, the solution needed to have a final salt concentration lower than 0.3 M and have an ethanol concentration of 70 %. To obtain the required salt concentration, the already high salt content in the elution volume was taken into consideration.

*Table 3: Volumes used for precipitation of DNA.*

Substance	Volume ( $\mu\text{L}$ )
3M sodium acetate	35

95-100 % ice-cold ethanol	337
Sample	100
Total	472

After mixing, the DNA-samples were placed at -20 °C for at least 30 minutes to allow for precipitation of the DNA. The samples were then centrifuged at 13 000 rpm at 4 °C, for 30 minutes to form a DNA-pellet. The supernatant was carefully removed using a pipette. DNA-pellets were washed with ice-cold 70 % ethanol and centrifuged at 13 000 rpm at 4 °C, for 15 minutes. Excess ethanol was removed, the samples left to dry at room temperature, and the pellets were resuspended in 30 µL RNase-, DNase and protease free water.

### 3.3.3 Polymerase chain reaction

Polymerase chain reaction (PCR) is a technique used to amplify a specific DNA sequence *in vitro*. The protocol used for PCR was based on the article by Peng and colleagues (Peng et al., 2018). The method was a tetra-primer amplification refractory mutation system-polymerase chain reaction (ARMS-PCR) which employs two pairs of primers (listed in table 4).

**Table 4:** Primer sequences used for identification of G/T point mutation and wilt type alleles of the *Lepr* gene.

Gene	Sense	Genotyping pattern	Sequence
<i>Lepr</i>	Forward outside	610 bp (outer)	5'-TTGTTCCCTTGTTCTTATAACCTATTCTGA-3'
<i>Lepr</i>	Reverse outside	406 bp (T allele)	5'-CTGTAACAAAATAGGTTCTGACAGCAAC-3'
<i>Lepr</i>	Forward inner	264 bp (G allele)	5'-ATTAGAAGATGTTTACATTTTATGATGGA <u>A</u> GG-3'
<i>Lepr</i>	Reverse inner		5'-GTCATTCAAACCATAGTTTATGTTT <u>G</u> TCTA-3'

One set of primers was used to amplify the wild-type allele (G allele) and one to amplify the mutant allele (T-allele) in the PCR reaction. The forward- and reverse outer primer were complimentary to a part of the sequence encoding the *Lepr* gene, forward inner primer was G allele-specific, and the reverse inner primer was T allele-specific. A summary of ARMS-PCR

with all four primers are illustrated in figure 7. The inner primers have a 3' terminus mismatch (A-C mismatch or G-T mismatch) and a mismatch at position -2 from the 3' terminal compared to the same allele-specific primer to increase the specificity of the reaction (marked in bold and underlined in table 4).

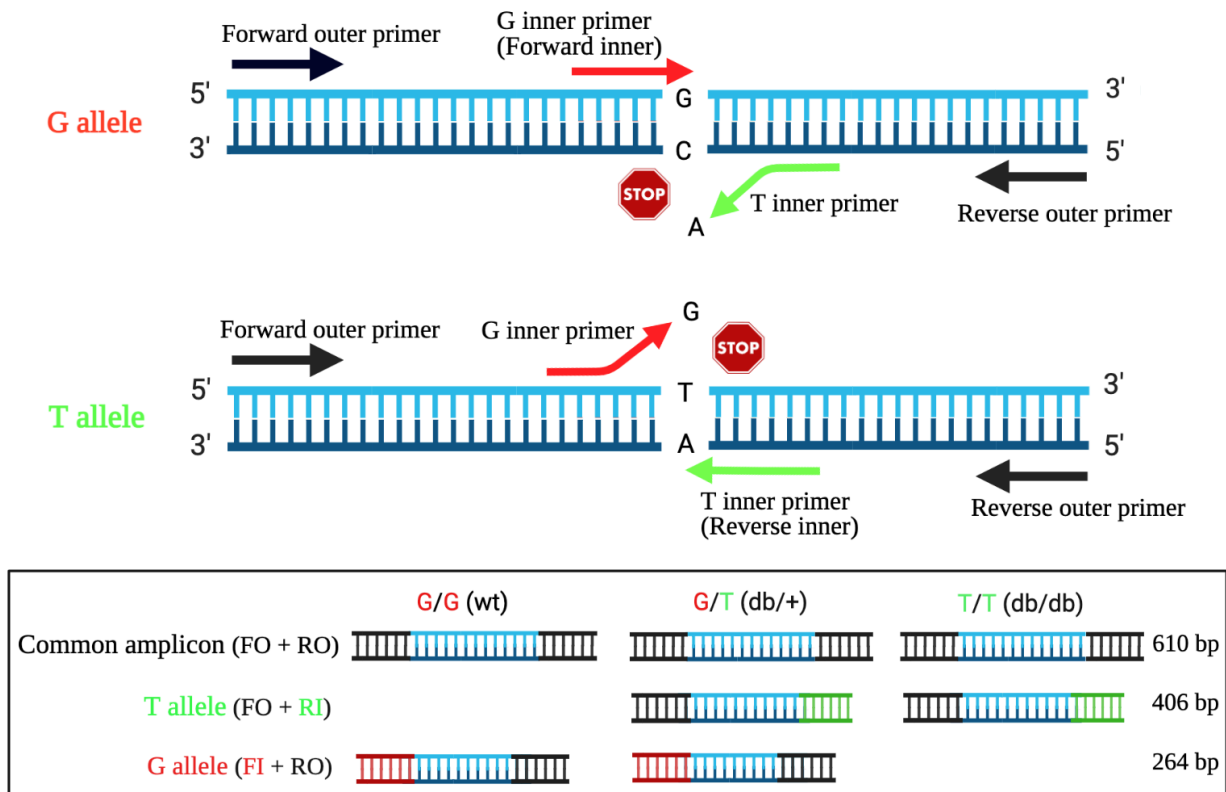


**Figure 7: A schematic summary of ARMS-PCR and DNA gel patterns of the different genotypes.**

Different colors indicate different primers participating in the ARMS-PCR; Black: outer primers, green: reverse inner primer, and red: forward inner primer. The outer primers bind and amplify the corresponding genomic DNA sequence and generate a fragment with 610 bp in all genotypes that acts as an internal control for the PCR reaction. The inner primers are allele specific, which means that the forward inner primer will not bind the T allele as the nucleotide at the 3' end of the primer is not matching with the DNA sequence (see stop sign). But the forward inner primer will amplify the G allele and produce G allele specific bands in combination with the reverse outer primer. The reverse inner primer will produce a T allele specific band along with the forward outer primer. Annotations: FO-forward outer primer; RO-reverse outer primer; FI-forward inner primer; RI-reverse inner primer. (Created with BioRender, 2021)

Principal components needed for PCR are; a template DNA to be amplified, primers complementary to a sequence of target DNA and consequently provides a starting point for DNA synthesis, *Taq* polymerase to make new strands of DNA along with deoxynucleotides

(dNTPs), and buffer to provide optimal conditions (Waters & Shapter, 2014). The PCR sample was made by mixing OneTaq<sup>®</sup> Hot Start Master Mix (containing *Taq* polymerase and Deep Vent<sup>®</sup> DNA polymerases, buffer components, MgCl<sub>2</sub>, dNTPs and stabilizers), DNase-, RNase- and protease free water, primers and DNA sample (volumes are listed in table 5). Everything was put on ice to avoid unwanted activity of *Taq* polymerase and formation of primer dimers. High temperature is frequently used during PCR to denature the DNA strands; therefore, a heat-tolerant DNA polymerase is essential. *Taq* polymerase was retrieved from the *Taq* DNA Polymerase gene from the heat-tolerant bacterium, *Thermus aquaticus* YT-1, thus are heat-stable (New England BioLabs, 2021a).

**Table 5:** Substances and volumes used for PCR samples.

Substance	Volume (μL)
DNase, RNase and protease free water	6 μL
Forward outer primer	1 μL
Reverse outer primer	1 μL
Forward inner primer	1 μL
Reverse inner primer	1 μL
OneTaq <sup>®</sup> Hot Start 2X Master Mix with Standard Buffer	15 μL
DNA sample	5 μL
Total	30 μL

The PCR samples were placed in a PCR apparatus (Applied Biosystems 2720 Thermal Cycler, Thermo Fisher Scientific, USA). The PCR cycles consisted of initial denaturation at 94 °C to provide single-stranded DNA template, followed by 40 cycles of denaturation, annealing and elongation as listed in table 6. For primers used in this protocol, a temperature at 57 °C in the annealing step made the primers bind to their complementary sequences on the DNA template. Next, the temperature was raised to 68 °C in the elongation step, and the *Taq* polymerase began to replicate the DNA sequences by adding nucleotides. Final elongation ensured remaining single-stranded DNA to be entirely elongated before the cooling step. The number of DNA sequences amplified increases exponentially, by doubling in each round of

cycling until sufficient amount of desired DNA was amplified (after 40 cycles) (Peng et al., 2018; Waters & Shapter, 2014).

**Table 6:** PCR cycles for genomic DNA

Number of cycles	Temperature	Step	Time (minutes)
1	94 °C	Initial denaturation	5
40	95 °C	Denaturation	0.5
	57 °C	Annealing	0.5
	68 °C	Elongation	1
1	68 °C	Final elongation	5
1	4 °C	Cooling/end	∞

### 3.3.4 Gel electrophoresis

Gel electrophoresis is a method used to separate DNA based on number of base pairs (bp) and charge. DNA samples were added to a 2 % agarose gel and a charge of 100 mV-110 mV was applied to the chamber for 35-40 minutes. Since the DNA is negatively charged, and the charge is proportional to the number of base pairs, DNA fragments will migrate towards the anode (positive charged side). The agarose in the gel will retain DNA, thus the fragments with short sequences will move longer than fragments with large sequences which will have more resistance within the gel.

A 2 % agarose gel was made by dissolving agarose in 1x TAE (Tris-acetate-EDTA) buffer using a microwave and adding GelRed® (10000x in water) to a final concentration of 1x. GelRed® is a fluorescent nucleic acid dye added to stain the double stranded DNA and make visible bands of DNA at the agarose gel. Samples for gel electrophoresis were prepared by mixing for each sample: 15.8 µL of DNase-, RNase- and protease free water, 4.2 µL of 6x Purple Loading Dye, and 5 µL of PCR product for a total volume of 25 µL. To the standard, 5 µL of GeneRuler 100 bp Plus DNA Ladder was added instead of PCR product. The standard DNA ladder functioned as a control with defined DNA sizes. After 35-40 minutes of gel electrophoresis, the gel was visualized under UV-light in a gel imaging system (Molecular Imager® Gel Doc™ XR+ with Image Lab™ Software, Bio-Rad, USA) and imaged.

### 3.3.5 Interpretation of the results

The two allele-specific amplicons contain different length of base pairs, allowing for separation by gel electrophoresis. The PCR product for G allele (wild-type allele) was 264 bp and the PCR product for T allele (mutant allele) was 406 bp. The forward outer primer and reverse outer primer amplified the region next to the mutation (G→T mutation) in the *lepr* gene, producing non-allele-specific control bands at 610 bp. The samples were compared to the standard DNA ladder with known base pair lengths. The wt mice were identified on the agarose gel by two visible bands at 264 bp and 610 bp. The *db/+* mice had inherited both alleles and therefore showed all the PCR products on the gel, accordingly, being identified by visible bands at 264 bp (encoding G allele), 406 bp (encoding T allele) and 610 bp (non-allele specific positive control). The *db/db* mice were identified by two visible bands at 406 bp (T allele) and 610 bp (non-allele specific positive control) on the agarose gel. Gel electrophoresis and analysis of the results are shown in figure 8.

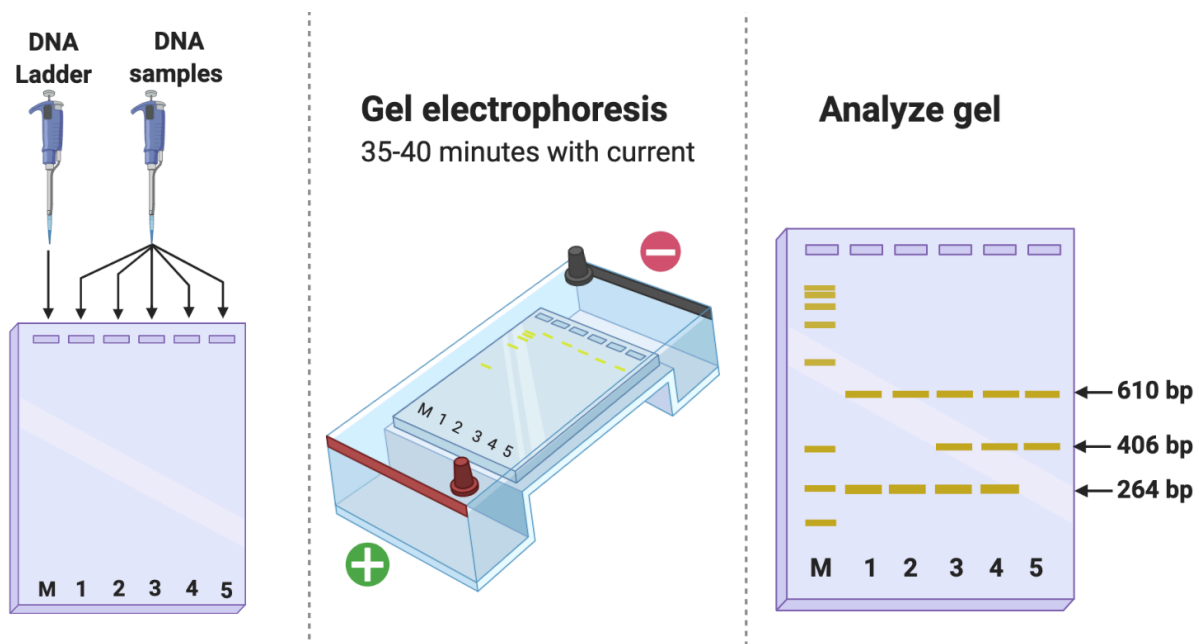


**Figure 8: Gel electrophoresis and interpretation of results.**

First DNA samples and DNA ladder were transferred to wells in a 2 % agarose gel, then current was applied for 35-40 minutes. Finally, wt mice were identified having visible bands at 610 bp and 264 bp, *db/+* mice were identified having visible bands at 610 bp, 406 bp and 264 bp and *db/db* mice were identified having visible bands at 610 bp and 406 bp. (Created with BioRender, 2021)

## 3.4 Open field

To measure the emotional behavior of the mice, an open field test was performed when the mice reached 9-11 weeks of age and before any training and other experiments. In total, 17

*db/db* mice and 22 *db/+* mice performed the open field test. All animals conducted the open field test only once.

The open field test is used to measure spontaneous locomotor activity motivated by exploration. The test can also be used to measure anxiety-like behavior in rodents, although other more specific anxiety tests also exist. In the open field test, the animal was placed in an empty square 40x40 cm arena surrounded by walls (height = 30 cm) and was allowed to freely explore the arena while its movements were tracked for 60 minutes. The level of activity (distance travelled, average speed etc.) during the last 50 minutes of the test were used as measures for the spontaneous locomotor activity of the animal. Locomotor activity during the first 5-10 minutes of the test is usually disregarded, as this is believed to primarily reflect anxiety-driven movements. Hence, the tendency the animals have to “hide” in the corners or along the wall of the arena as opposed to exploring the arena give an insight into the anxiety state of the animal (Bailey & Crawley, 2009; Kuniishi et al., 2017; Seibenhener & Wooten, 2015).

Before performing the open field test, the animals were habituated to the behavior room for at least 60 minutes. The test was performed in a VersaMax Animal activity monitor (AccuScan Instruments, Inc., USA). The mouse was placed in individual arenas and allowed to freely explore it for 60 minutes while movements were tracked by infra-red sensors in the floor of the square activity monitor. Example of heat maps and movement tracking are shown in figure 9. The test was first performed on the female mice because the smell of male mice can make them anxious. To avoid the animals from being distracted by smell, the open field apparatus was disinfected with ethanol (70 %) between each mouse and allowed to dry completely. The light was set at 40 lx, and the lighting was indirect and adjusted to not leave shadows or dark corners in any of the arenas. The experiment was performed in silence. The operators left the room to ensure that there were no sounds or movements that could cause stress or affect the test result.

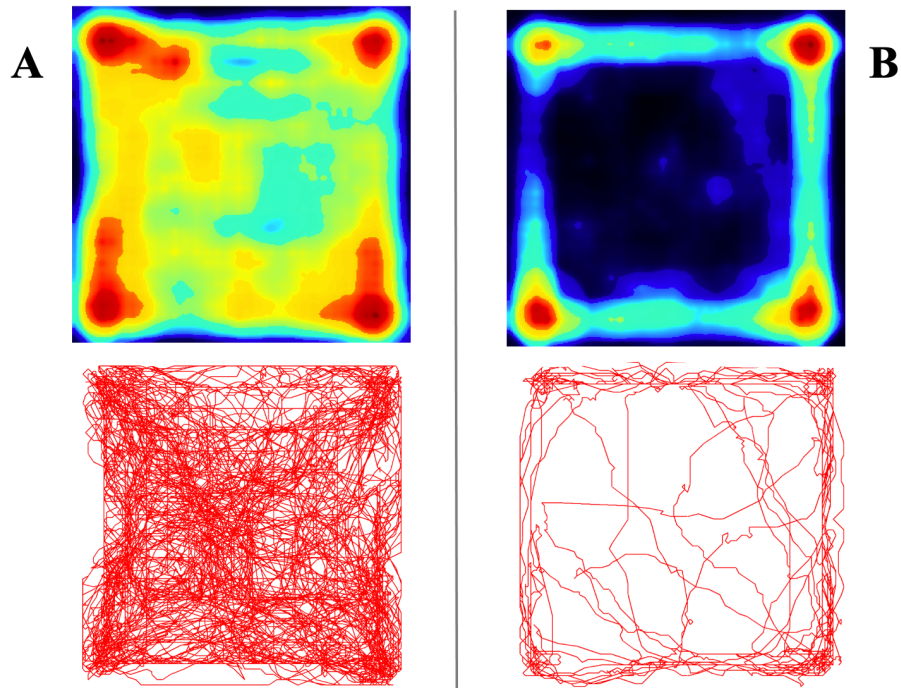


**Figure 9: Example of heat maps and tracking of movement by infra-red sensors.**

*A) Heatmap and movement tracking of a mouse with a lot of activity and exploring of the area in the open field test. B) Heatmap and movement tracking of a mouse which spent most of the time sitting still or moving slowly in the corners and along the walls during the open field test.*

The center region was defined as a 20 cm x 20 cm area at 10 cm away from the walls. The first 10 minutes of the test results was used to gain insight into the anxiety and emotional behavior of the mice. Mice feel exposed in open areas and anxious mice will therefore typically prefer the periphery area of the apparatus and have less movement than a relaxed animal that repeatedly explore the unprotected center area. Less time spent in the central region, increased latency to enter the central part and decreased locomotion are signs of anxiety-like behavior (Bailey & Crawley, 2009; Kuniishi et al., 2017). The following 50 minutes were used to track spontaneous movement. The distance travelled (both in the peripheral and the center area) and the speed of the movements was detected.

### 3.5 Exercise regime

The animals started interval training when they reached 9-11 weeks of age, which translates to adult age in humans. For the interval training, 12 *db/+* mice and 12 *db/db* mice were included but one of the *db/db* mice was later excluded due to absence of an obesity phenotype. The interval training was performed on an Exer 3/6 treadmill (Columbus Instruments, USA) designed for rats and mice. The treadmill had a single belt construction



and 6 individual lanes with a rest podium for each mouse. The training was conducted 5 consecutive days each week for a total of 8 weeks, giving the mice 2 days of rest per week. For each session, 6 mice ran simultaneously on the treadmill, at a 25° incline. When necessary, the operator gently pushed the mice to keep them running during the high-intensity intervals, however, it was often sufficient to touch their tails. Most of the animals ran voluntarily after day 2, yet the resting platform in each lane contained an electrical grid that could provide a gentle footshock at an intensity of <1.5 mA if mice were unwilling to run. The use of electric shock was limited to maximum one shock per animal in one workout session, however, most mice were never subjected to electric shock. After each workout session, the treadmills were washed with soap and disinfected with 70 % ethanol.

The exercise regime consisted of a warm-up and 10 high intensity intervals intermitted by rest periods. Before every interval session there was a 10-minute warm-up, which was performed at 5 m/min for *db/db* mice and 8 m/min for *db/+* mice. The interval protocol consisted of 10 intervals with 4 minutes high intensity running and 2 minutes of low intensity between each interval. The speed used for the intervals were adjusted based on the performance of the mice in a maximal exercise capacity test (MECT; see below), the intensity during active rest for *db/db* mice was set to 5 m/min, and 8 m/min for *db/+* mice. During active rest, the mice could choose between running at a low speed or to sit on the resting podium. One exercise session lasted for 68 minutes.

**Habituation:** On the first day of exercise, the animals got habituated to the treadmill by running at a low speed. The *db/db* mice started running at 5 m/min during intervals and increased to 8 m/min, while the *db/+* mice started running at 8 m/min and increased to 18 m/min. During active rest the treadmill was set to 3 m/min for *db/db* and 5 m/min for *db/+*. On their second day of exercise, a test was performed to determine the maximum capacity of the animals.

**Maximal exercise capacity testing (MECT):** MECT was performed on Tuesdays every other week during the experiment to constantly ensure that the mice were running at high intensity during the intervals. The MECT consisted of a warm-up for 15 minutes at 9.6 m/min followed by an increase of the running speed of 1.8 m/min every two minutes. The test was performed without rest and lasted until exhaustion (table 7). A mouse was considered

exhausted when it jumped with its hind legs and was unable/unwilling to run even despite being gently pushed back onto the band by the operators. When a mouse reached maximal capacity, the elapsed time and maximal running speed was noted. The average maximal running speed for each genotype was calculated and followed from fortnight to fortnight.

**Table 7: The MECT protocol.**

<b>TIME (minutes)</b>	<b>SPEED (meter/minute)</b>
Warm-up: 15	9,6
0-2	11,4
2-4	13,2
4-6	15
6-8	16,8
8-10	18,6
10-12	20,4
12-14	22,2
14-16	24
16-18	25,8
18-20	27,6
20-22	29,4
22-24	31,2
24-26	33
26-28	34,8
28-30	36,6
30-32	38,4

Based on the MECT results, 80 % of the maximum capacity was calculated for each mouse and used to determine the interval speed. However, between test days, if the animals were not tired, the interval speed was gradually increased based on manual observations of the animals, but not more than 0.2 m/min per day and 0.5 m/min per week. To ensure that all mice exercised with 80 % of their maximum capacity, the speed was usually set according to the mice that performed best in the endurance test, and generally on the other exercise days. Those with less endurance were given a 10-second break on the resting podium during the intervals if needed. Nevertheless, the operators used a suitable speed to make sure all the animals completed the exercise protocol with all 10 intervals.

Interval exercise was performed five days a week but was exchanged with MECT test once every second week as described. The training was based on previously used training protocols (Morland et al., 2017) and adapted to the *db/db* animal strain (table 8).

**Table 8:** Exercise regime for the *db/db* and *db/+* mice.

EXERCISE REGIME				
		<i>db/db</i> mice	<i>db/+</i> mice	Time
<b>Warm-up</b>		5 m/min	8 m/min	10 min
<b>Intervals</b>	10 x running	80 % of maximum capacity	80 % of maximum capacity	4 min
	9 x rest time	5 m/min	8 m/min	2 min

Throughout the exercise intervention period, the operators were constantly watching the animals during both the training and the endurance test to see if any animals showed signs of stress or injury. Exclusion criteria based on signs of distress or pain were set *a priori* and described in the approved FOTS: If an animal lost more than 10 % of their weight and/or their fur appeared less shiny over time, as these are signs of discomfort. Animals should also be excluded from the experiment if they displayed stereotypic behavior. Finally, if an animal suddenly appeared to struggle with exercise intensities that it normally did not struggle with, the animal was presumed to be sick or injured, and were given additional breaks during the exercise. If the same animal performed worse than expected in more than two consecutive exercise sessions, the animal was believed to be injured or sick, and should therefore be excluded from further experiment. None of the animals met these exclusion criteria.

On the second test day (day 22 of exercise), the belt on the treadmill stopped during the test, creating noise and stress for the two *db/+* mice running on that treadmill. In addition, the operators had to move the mice to a functional treadmill giving them a few seconds of break. The test results from this day may therefore be incorrect for two of the *db/+* mice. On day 23 of exercise (the day after maximum capacity test), a *db/+* mouse refused to run after the second interval and therefore was allowed to rest the remaining time that day. This was most likely due to exhaustion and stress from the MECT the day before.

### 3.6 Body weight and body composition measurements

The mice were weighed every week. In addition, to examine the development of the body composition of the mice during the intervention period, their body composition was measured once every week for a total of 8 weeks using Bruker's minispec LF90II (Germany). The apparatus is based on Time Domain Nuclear Magnetic Resonance (TD-NMR) which provides a strong magnetic field resulting in signals from all protons in the sample volume, hence

making it possible to calculate fat, free body fluid and lean tissue values (Bruker, 2021). Lean tissue includes muscle, internal organs, connective tissue, bone and water, and therefore gave an insight into the development of muscle mass in the animals. The instrument was calibrated for measurements of mice. Measurements were taken on 3 *db/db* sedentary mice, 6 *db/+* sedentary mice, 12 *db/+* exercised mice and 11 *db/db* exercised mice.

Before starting the body composition measuring, an instrument check was performed on the minispec LF90II using minispec Plus software (Bruker, Germany). A check sample (glass bottle containing seeds) was placed into the machine and after 2-3 minutes the instrument was validated for 24 hours.

Female mice were measured first to avoid being stressed or anxious by the smell of male mice. The instrument did not measure all body components (for instance, bones were not measured), and therefore the mice were weighed prior to the analysis. The weight was noted in the software system. One mouse at a time was placed in a special circular restrainer probe designed for use in minispec LF90II. The inside space of the restrainer could be adjusted by moving a plunger up and down. The restrainer was adjusted so that the mouse could not move around in the tube, but not so much that the mouse was squeezed. Then, the animal was placed into the minispec probe (in the center of the instrument) for 2-3 minutes to acquire data of the body composition. After each mouse, the restrainer was cleaned with mild soap in water and paper to remove any urine, feces, fur or dirt. When the restrainer was completely dry, the next mouse was placed inside for measuring. Finally, the data was exported to Microsoft Excel and used to monitor the physical state of the exercised and sedentary mice.

### **3.7 Morris Water Maze**

Morris water maze (MWM) is a behavioral test that is used to evaluate hippocampal-dependent memory in rodents. The hippocampus plays a key role when it comes to learning and spatial navigation, which is characterized by the ability to navigate using cues and objects at some distance from the organism, so called distal cues (Vorhees & Williams, 2014). MWM is conducted in a circular pool filled with opaque water and with a hidden platform below the water surface. Cues and objects are placed in the environment surrounding the pool, making it possible for the animals to navigate within the pool. One mouse at a time is placed in the pool from different drop points and swim for a certain time, before being placed on the platform.

The experiment is performed over a maximum of 14 days with the hidden platform staying at the same place during the training days, making it possible for the animals to learn the location of the platform using the cues and objects in the testing room. To test the capacity of the animals to remember and use learned information to find the platform location, the platform is removed on the last day of the experiment.

MWM test was performed in parallel with the last days of training for the exercised mice. To avoid that the mice were tired during the MWM, this test was performed in the morning and running was performed in the afternoon. In total, 11 exercised *db/db* mice, 12 exercised *db/+* mice, 3 sedentary *db/db* mice and 12 sedentary *db/+* mice were included in the MWM test.

Prior to the MWM test, the animals were acclimatized in the behavior room for at least 60 minutes before the experiment started. The time the animals were placed for acclimation was noted. MWM test was performed in a circular pool (diameter = 150 cm, height = 29.7 cm) filled with water up to 21.5 cm and made opaque with non-toxic paint that did not adhere to the animals (SENS 3i1 Vegg/Panel/List 30, Jotun, Norway). A circular platform (diameter = 11 cm) was located at the north end of the pool. The distance from the center of the platform to the north wall of the pool was 29.5 cm (see figure 10). This platform was hidden below the water surface, and to give the obese *db/db* mice the opportunity to climb the platform, it was submerged 1 cm below the water surface (0.5-1 cm is customary in these experiments). The water temperature was maintained at  $26 \pm 1$  °C, and was measured before the experiment started, during the experiment and again after the test to ensure that the temperature was within the temperature range throughout the experiment. Keeping the water temperature consistent for all animals is essential, as the aversiveness of the water increases motivation to find the platform. To low temperatures, however decrease the ability to focus and learn while higher water temperature may cause the mice to find it comfortable, and float instead of search for the platform (Morgan, 2009). The light at the water surface was adjusted to 35-45 lux and was measured every day before starting the test, halfway through-, and after the test. The lighting was indirect to avoid reflections and shadows to affect the navigation of the animals. Various figures and objects were surrounding the pool, such as pictures and taped objects placed on the walls outside of the water maze, which made it possible for the animals to learn and memorize the location of the platform.

By using the behavioral tracking software, ANYmaze (Stoelting Group, Ireland) and a camera above the pool, the MWM pool was divided into virtual quadrants denoted; north, south, west and east zones. The platform was located within the north zone, and a platform zone (a 11 cm in diameter circular area just above the platform) and a peri-platform zone (the 3 cm surrounding the hidden platform) were defined in the program (see figure 10).

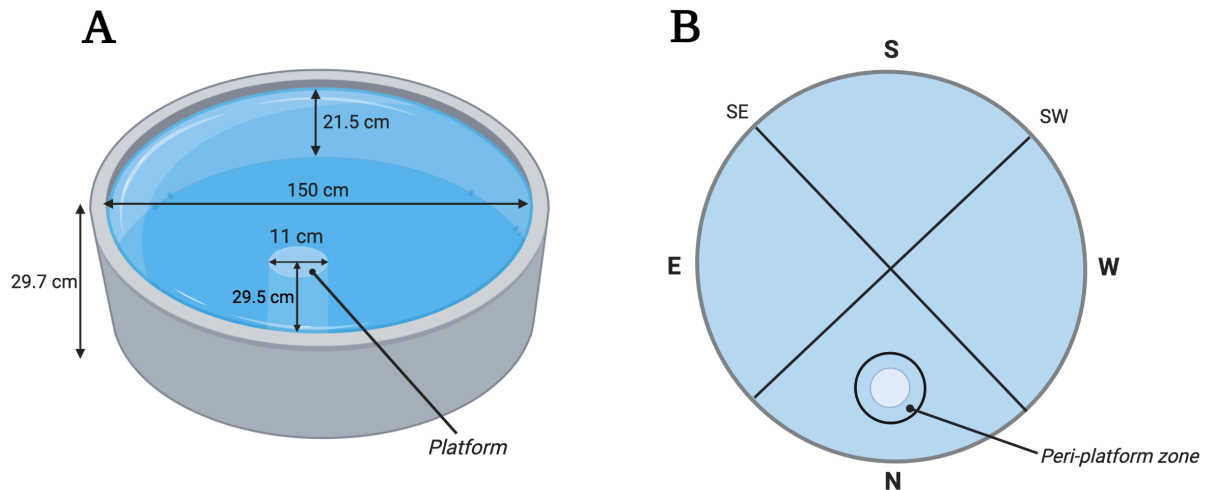


**Figure 10: MWM pool.**

**A)** The circular pool had a diameter of 150 cm, height of 29.7 cm, water height of 21.5 cm and the diameter of the platform (and hence of the platform zone defined in the ANYmaze program) was 11 cm. The length from the center of the platform to the north end of the pool was 29.5 cm. **B)** The pool had 6 zones, south (S), west (W), north (N), east (E), platform and a peri-platform zone within the north zone. (Created with BioRender, 2021)

Two operators were required to perform the MWM experiment, operator 1 (OP 1) monitored data using ANYmaze and kept track of the time, while operator 2 (OP 2) handled the mice. For both training days and the test day, ANYmaze assembled data on test duration, total distance travelled, average swimming speed, number of entries to the different zones, time in the zones and latency to the first entry to the north-, peri-platform- and the platform zone. For animals who did not enter the zone of interest during the 60 seconds probe trial, the latency was set to 60 seconds. Track plot and video-tracking were also recorded. Frequent entries- and extensive time spent in the platform- and peri-platform zone during the test day (probe trial) was considered an indication of learning.

The MWM test was performed for 10 days, where the first 9 consecutive days consisted of training and the last day was a probe trial without the platform. On the training days, each mouse swam 4 trials for 60 seconds, or until they found the platform (within the 60 seconds). For the 4 trials, the mice were introduced into the pool from each of the four different drop points: south-west (SW), south-east (SE), west (W) and east (E). The order of these drop

points was equal for all the mice but was randomized between each training session (see table 9), so that the animals should navigate based on visual cues and not based on a specific swimming pattern. After each trial, the animals were placed on the platform, either by climbing up themselves or by OP 2, to learn the surroundings in relation to the platform. Each mouse stayed on the platform for 30 seconds before being placed back in the pool (facing the wall), to perform the next trial. If the mice floated, jumped off the platform or showed other deviant behavior, OP 1 registered it on an MWM-form (an example of an MWM form are attached as an appendix). After the mice had finished their trials, they were placed in a heating cage (one for females, and one for males) where they dried before being placed back in their cages.

**Table 9:** Randomized drop points into the MWM pool. On day 10 it was only one trial starting from the south.

	<b>Trial 1</b>	<b>Trial 2</b>	<b>Trial 3</b>	<b>Trial 4</b>
<b>Day 1</b>	SW	SE	E	W
<b>Day 2</b>	E	W	SW	SE
<b>Day 3</b>	W	SE	E	SW
<b>Day 4</b>	SE	W	SW	E
<b>Day 5</b>	E	SW	SE	W
<b>Day 6</b>	W	E	SW	SE
<b>Day 7</b>	SE	E	W	SW
<b>Day 8</b>	SW	SE	W	E
<b>Day 9</b>	E	W	SE	SW
<b>Day 10</b>	S			

On the test day, the mice were dropped from the south point. This was a drop point that had not been used during the training, and which was directly opposite to the platform location. The mice were tested on day 10 in a single 60 second trial, in which the platform was removed. The mice were gently placed into the pool and swam continuously for the 60 seconds, before being placed in the heating cage. Mice floating more than 10 seconds were noted on the MWM-form and mice floating more than 30 seconds were excluded from the result.

Behavioral experiments are sensitive to all kinds of changes; therefore, the experiment was performed as similar as possible from day to day, in terms of workflow, locations, placement of cages, clues and objects, start time and silence. The order of mice placed in the pool was kept constant. To further minimize disturbances that could affect the animal's performance or

learning process, the same person was appointed as OP 2, with an exception on day 4. Due to the SARS-CoV-2 (COVID-19) outbreak, day 5 of training were postponed 3.33 hours for 3 sedentary *db/db* mice and 6 sedentary *db/+* mice because the two operators where in quarantine until negative test results for SARS-CoV-2.

### 3.8 Perfusion fixation

Fixation is used to preserve the cytoarchitecture of the tissue even after being extracted from the animal, and prevent degradation, bacterial growth, autolysis and hypoxia. Transcardial perfusion was performed by pumping paraformaldehyde (PFA) 4 % in 0.1 M sodium phosphate buffer, pH 7.4 (NaPi) as fixative directly into the arterial system of deeply anesthetized animals, using an external peristaltic pump (Watson-Marlow 323 pump, Watson-Marlow, UK) to replace the blood in the animal with fixative fluid. Formaldehyde prevents tissue decomposition by forming intra- and intermolecular cross-links between amino groups in the side chains of proteins, resulting in formation of methylene bridges (Howat & Wilson, 2014). PFA (4 %) fixative was prepared in a laminar flow cabinet the day before perfusion, because to solve and depolymerize PFA it must be heated (70° C) in NaPi overnight. Formaldehyde can crystallize spontaneously, so to remove crystals that could other ways occlude blood vessels, the solution was filtered using funnel and filter paper (VWR, qualitative filter paper, 403, medium filtration rate) to ensure good perfusion (Kiernan, 2000).

Associate Professor Cecilie Morland and PhD student Gezime Seferi performed the perfusion on all exercised and sedentary *db/db* and *db/+* mice (17-19 weeks old) at 6 hours after the last training session (and after the MWM test).

An additional set of sedentary *db/db*- and *db/+* mouse brains at 16 weeks of age was a gift from the CERG group (NTNU, Trondheim), led by Prof. Ulrik Wisløff. These animals were perfused by members of the CERG group. The 5xFAD mice were perfused by Associate Professor Cecilie Morland at 39-, 42- or 49 weeks of age.

The peristaltic pump was prepared and emptied for air bubbles by letting the PFA fixative flow through the system, and animals were anaesthetized with intraperitoneal (i.p.) injection of 0.1 ml/10 g bodyweight ZRF cocktail (3.3 mg/mL zolazepam, 3.3 mg/mL tiletamine, 0.5 mg/mL xylazine and 2.6 µg/mL fentanyl). Toe pinch test was performed to make sure the



depth of anesthesia was sufficient. When there were no reflexes and pain-responses to the toe pinch, the mouse was fastened lying on its back on a polystyrene block using 4 needles.

The following steps were performed in a fume hood to avoid exposing the operators to formaldehyde fume: An incision was made to open the abdominal cavity and the diaphragm was perforated. This step was critical as puncturing of the diaphragm interrupts the intrapleural pressure and therefore the gas exchange in the lungs and may induce hypoxia. Further steps were therefore conducted as fast as possible. The thorax was carefully opened while avoiding to damage heart or arteries, and the heart was exposed. A small incision was made in the right atrium and the perfusion cannula connected to the peristaltic pump was inserted into the left ventricle. The pump transferred fixative at 5 mL/min (equivalent to the animal's cardiac output), and blood and perfusate left the circulation by the punctured atrium. The perfusion lasted for 8 minutes/animal; during this time the body turned stiff and the organs were emptied of blood; the liver quickly turned pale, which was used as a sign for good perfusion. After the perfusion, the animal was decapitated, and the brains were gently removed from the skull and placed in 4 % PFA in NaPi at 4 °C over night. The brains were then transferred to 0.4 % PFA in NaPi and stored at 4 °C.

### **3.9 Cryostat sectioning**

Cryostat sectioning is a method for sectioning snap-frozen tissue by using a cryostat instrument. The cerebellum was removed from the fixated brains in a fume hood using a razor blade and the forebrain was divided along the midline as illustrated by lines in figure 11. The hemisphere designated for sectioning was transferred to a falcon tube containing 30 % sucrose in NaPi, overnight in refrigerator to saturate the brain tissue and prevent cell damage when frozen. Sucrose increased the risk of bacterial growth; therefore, sectioning was performed consecutively after the brains sank to the bottom of the falcon tube (the latter was regarded as a sign that they were fully saturated with sucrose).

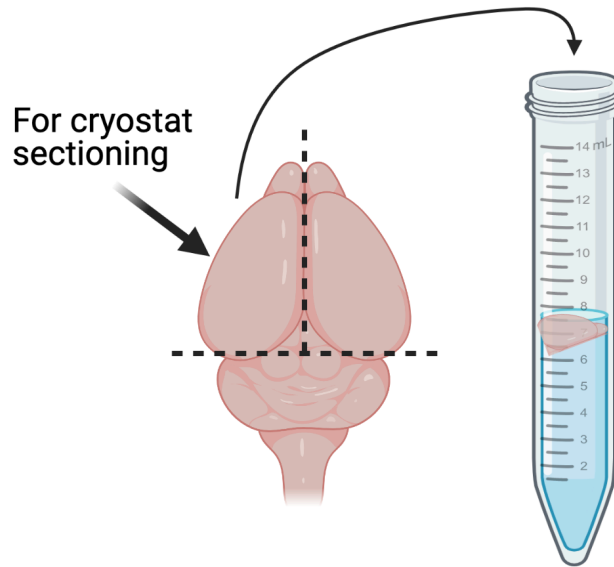


**Figure 11: Preparation of brain tissue for sectioning.**

*The cerebellum was removed from the perfusion fixed brain with a razor blade (indicated by the horizontal dotted line), and the forebrain was cut in half along the midline (illustrated by the vertical dotted line). The brain tissue for sectioning was transferred into 30 % sucrose in a falcon tube and left to sink overnight. (Created with BioRender, 2021)*

Microtome sectioning was performed using a Microtome HM450 (Thermo Scientific, USA) connected to a freezing unit, KS 34 (Thermo Scientific, USA). While the microtome plate cooled to  $-40\text{ }^{\circ}\text{C}$ , 12-well cell culture plates (Thermo Fisher Scientific, USA) were prepared by filling roughly 3-4 mL NaPi with 0.05 % azide into each well. A wedge-shaped steel knife was attached to the microtome, and 30 % sucrose was added to the tissue block using a pasteur pipette to make an ice platform (about 2 x 2 x 1 cm). Every time the microtome knife passes the tissue, a section the pre-set thickness is made. The ice platform was trimmed to a flat surface, followed by placing the hemisphere with the medial side down on the flat platform. The brain was gradually fixed by pipetting 30 % sucrose on the base and on top of the brain. When frozen, this kept the brain still and prevented separation from the platform during sectioning. A styrofoam box were placed over the brain till it was completely frozen. The temperature was then set to  $-22\text{ }^{\circ}\text{C}$  and  $20\text{ }\mu\text{m}$  sections were made by moving the knife horizontally over the frozen tissue. Exercised and sedentary *db/db* and *db/+* mice (17-18 weeks old) were sectioned sagittally, while the 5xFAD mice (tg and the wt controls) were sectioned coronally. The sedentary *db/db* and *db/+* mice given from the CERG group were already sectioned along the sagittal plane by Gezime Seferi before this master project started.

Sections were moved from the knife and placed in the 12-well plates using a suitable soft paintbrush (Brush Watercolor Round No. 0 and 3/0 pine marten hair, Panduro Hobby, Norway) starting from left to right (A1→A4 and ending at C1→C4) and with 5 serial sections in each well. This was repeated until the entire brain tissue was sectioned. Well plates with sections were covered with Parafilm M PM996 (Bemis, USA) and stored at 2-8 °C.

### 3.10 Immunohistochemistry

Immunohistochemistry (IHC) is a method based on specific bindings between antibodies and the antigen of interest in the tissue. The procedure consists of three main steps: antigen retrieval, incubation with primary antibodies and incubation with secondary antibodies. The secondary antibody, with specificity for the primary antibody, is conjugated to a fluorescent molecule making it possible for visualization under laser light (Ramos-Vara, 2005). This is called fluorescent IHC and is illustrated in figure 12.

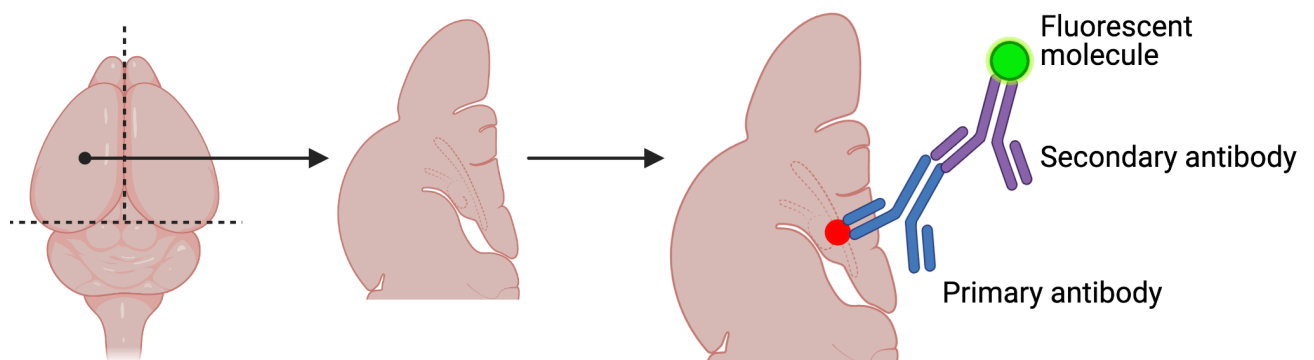


**Figure 12: Fluorescent IHC.**

*Immunolabeling with primary antibodies (blue) recognizing the antigen (red) and secondary antibodies (purple) conjugated to a fluorescent molecule (green). (Created with BioRender, 2021)*

To examine neuroinflammation in the hippocampal region of mouse brain, antibodies directed against markers of astrocytes and microglia were applied to the fixated brain sections. Microglia were labeled using antibodies directed against the widely used microglia marker, ionized calcium binding adaptor molecule 1 (Iba1), a macrophage- and microglial specific calcium binding protein. Astrocytes were labeled using antibodies against glial fibrillary acidic protein (GFAP), a class-III intermediate filament that is specifically expressed in astrocytes (abcam, 2021a). A fluorescent dye, 4,6-diamidino-2-phenylindole (DAPI), that binds selectively to double-stranded DNA was used to stain the nuclei (Sigma-Aldrich, 2021a).

Lipid droplets were labeled using BODIPY<sup>®</sup> 493/503 (4,4-Difluoro-1,3,5,7,8-Pentamethyl-4-Bora-3a,4a-Diaza-s-Indacene), a hydrophobic, fluorescent dye.

### **3.10.1 Buffers and solutions**

#### **Phosphate-buffered saline (PBS) pH 7.4**

9.8 mM Na<sub>2</sub>HPO<sub>4</sub>

137 mM NaCl

2.7 mM KCl

2 mM KH<sub>2</sub>PO<sub>4</sub>

in milli-Q water

#### **Citrate buffer pH 8.6**

114 mM sodium citrate

in milli-Q water

#### **Blocking solution**

3 % newborn calf serum (NCS)

1 % bovine serum albumin (BSA)

0.05 % triton X-100, in PBS

### **3.10.2 Procedure for immunohistochemistry along with BODIPY labeling**

The protocol for staining the 20 µm brain sections consisted of two days and are given in table 10 and 11. The selected coronal sections were from 1.46 mm posterior of bregma (Paxinos & Franklin, 2004) and the selected sagittal sections were from 2.35 mm lateral of bregma (Allen Institute for Brain Science, 2008). One section from each mouse was placed in 6 x 4 well plates (Nunclon 24-well cell culture plates, Thermo Fisher Scientific, USA) prepared with 1 mL PBS. An additional section (from one animal) was included and served as a negative control.

The methylene bridges caused by formaldehyde fixation may mask epitopes, and therefore limit antigen-antibody binding. Heat-induced epitope retrieval was therefore performed to expose antigen sites and allow antibodies to bind. The sections were exposed to citrate buffer at 80 °C for 30 minutes to break the methylene bridges. A two-step wash (each for 5 minutes) was performed to remove the citrate buffer.

To prevent non-specific antibody binding and reduce background, the sections were exposed to blocking solution for 2 hours. The sections were then incubated over night with 300 µL of primary antibodies diluted in blocking solution; Anti Iba1 Rabbit polyclonal antibody (FUJIFILM Wako Pure Chemical Corporation, Japan; Ref: 019-19741) diluted 1:500 and GFAP Mouse monoclonal antibody (Cell Signaling Technology, Netherlands; Ref: 02/2020) diluted 1:1500 (table 10). The negative control was incubated in blocking solution without primary antibodies overnight.

**Table 10:** Protocol for immunolabeling day one.

Step	Description	Time
1	Rinse in 1 mL PBS	2 x 10 minutes
2	Antigen retrieval with 500 µL Citrate buffer (pH 8.6) in an 80°C water bath	30 minutes
3	Rinse in 1 mL PBS	2 x 5 minutes
4	Block with 500 µL Blocking solution (3% NCS, 1% BSA, 0.5% triton in PBS)	2 hours
5	Incubate with 300 µL primary antibodies (1:500 Iba1) (1:1500 GFAP) in blocking solution (only blocking solution for the negative control)	Overnight

Day 2 started with rinsing the sections (6 x 10 minutes) in PBS followed by incubating with 300 µL of species-specific secondary antibodies diluted 1:500 in blocking solution; Goat anti-Rabbit IgG, Superclonal™ Alexa Fluor 647 (Invitrogen, India; Ref: A27040) and Alexa Fluor™ 594 goat anti-mouse IgG (Invitrogen, USA; Ref: A11032) as described in table 11. The secondary antibodies were added to visualize the location of the primary antibodies by

fluorescent molecules excited at different wavelengths (647 nm and 594 nm). For all remaining steps, the well-plates were covered in aluminum foil to prevent bleaching of the fluorescence signal. After rinsing, the sections were incubated with BODIPY in dimethyl sulfoxide (DMSO). BODIPY dissolves in lipids in the tissue and is therefore used for visualization of lipid droplets by presenting excitation at 493 nm and emission at 503 nm (Thermo Fisher, 2021). To rinse after applying BODIPY, the solution was first exchanged with 1 mL PBS three times, before washing with 1 mL PBS for 10 minutes a total of three times. To make sure all excess BODIPY was removed, the plates were kept at an angle making it easier to pipette out all the liquid. After the last rinse, the plates were held on both a black and a white surface to check if the fluid still was not still yellow. If there were traces of the yellow BODIPY in some wells, another rinse-step was conducted for 10 minutes with 1 mL PBS. In order to see the location of the antibodies in relation to the cellular structures within the tissue, DAPI (1:5000) was used as a counterstain. A last, 3 x 10 minutes wash with PBS was performed before the brain sections were mounted on 25x75x1.0 mm Thermo Scientific, SuperFrost Plus™ Adhesion slides (Thermo Fisher Scientific, USA). The brain sections were placed in a droplet of PBS on the adhesion slides using a paint brush (Paintbrush WaterColour Round nr 0, Panduro Hobby, Norway). By operating under a microscope (M60 stereo, Leica Microsystems, Germany) the brain sections were gently straightened in the PBS droplets. Finally, fluid droplets were removed, and cover glasses (Corning® cover glasses, thickness 1, 24x60 mm, Merck, Germany) were mounted using 10-17 µL ProLong Gold mounting medium. Mounted sections were stored shielded from light at 4 °C until confocal imaging.

*Table 11: Protocol for immunolabeling day two.*

Step	Description	Time
6	Rinse in 1 mL PBS	6 x 10 minutes
7	Incubate with 300 µL secondary antibodies (1:500) in blocking solution (3% NCS, 1% BSA, 0.5% triton in PBS) (647 Goat anti-Rabbit IgG and 594 Goat anti-mouse)	2 hours
8	Rinse in 1 mL PBS	3 x 10 minutes
9	Incubate with 300 µL 0.1 mg/mL BODIPY 493/503 (in DMSO). In the dark.	30 minutes

10	Exchange medium with 1 mL PBS (pipette off, pipette on)	3 x
11	Rinse in 1 mL PBS	3 x 10 minutes
12	Incubate with 500 $\mu$ L DAPI (1:5000) in PBS	15 minutes
13	Rinse in 1 mL PBS	3 x 10 minutes
14	Mount with ProLong Gold and add cover glass	

### 3.10.3 Image acquisition with confocal microscopy

Immunolabeled sections were imaged with a Zeiss LSM 880 Airyscan confocal microscope (Carl Zeiss Microscopy, Germany). Images were acquired as Z-stacks at 63x magnification from 2 areas in the hippocampal region of the mouse brain: cornu ammonis 1 (CA1) and cornu ammonis 3 (CA3) (as illustrated in figure 13). The lasers for visualizing DAPI, BODIPY, Iba1 and GFAP had wavelengths of 405, 488, 561 and 594, respectively. The laser intensities were optimized for each channel independently. The imaging settings were saved as a pre-setting and reused for all sections in the same experiment to ensure consistent intensity in all images. A 134.1 $\mu$ m x 134.1 $\mu$ m x 20 $\mu$ m three-dimensional scan was performed at each region of interest (ROI). Due to the COVID-19 outbreak, the acquisition of images was performed by PhD student Gezime Seferi from our Neurobiology and Toxicology group.

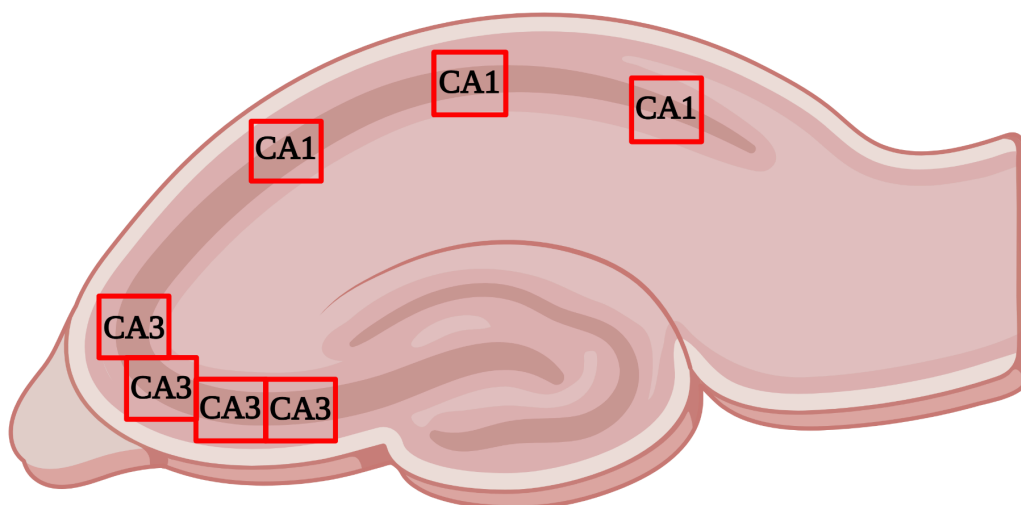


**Figure 13: Overview of hippocampal areas in mouse brains used for quantitative measurements of microglia and lipid droplets.**

*Three images were taken in the CA1 region, and up to five images was taken in the CA3 region depending on the length of the hippocampal CA3 area in each section. (Created with BioRender, 2021)*

## **3.11 Image analysis of microglia activation and lipid droplets**

The Fiji software (Image J, version 2.1.0, USA) was used to analyze confocal images for differences in microglia count, microglia activation and lipid droplets (LD) located in microglia in the CA1 and CA3 area in *db/db*, *db/+*, *5xFAD* and *wt* mice. Trainable Weka Segmentation (TWS), which is a machine learning tool, was used to automatically mark regions of interest (each individual microglia). The WEKA segmentation plugin (Arganda-Carreras et al., 2017) was used to segment Iba1+ and DAPI+ cells for further analysis. Morphological analysis and quantification of microglia was performed by using Fiji macros (see attached) made by PhD student Gezime Seferi, followed by manually counting and marking microglia. BODIPY+ lipid droplet numbers and size were analyzed manually. Quantification of Iba1+ and DAPI+ microglia and BODIPY+ lipid droplets were performed by an observer who was blinded to the genotypes and treatments.

### **3.11.1 Preparation and processing of the images for quantification of microglial cells**

The analysis of microglia consisted of three main parts: preparation and processing of images, adjusting threshold to segment microglia from the background, and using skeletonize plugin to create a skeleton construction.

The first macro (figure 14) opened with Fiji and the raw confocal images were edited for further analysis. The macro merged the channels (wavelengths) of Iba1 and DAPI staining from all the optical section of the 3D z-stack, resulting in a maximum intensity projection 2D image of microglia and nuclei combined in the images. The macro also removed background by converting the confocal images to 8-bit greyscale images where foreground intensity was higher than background (light cells on a dark background) and maximizing the pixels in each image. Nuclei that were not associated with Iba1 labeling and fragments of microglia that were not associated with a nucleus were removed, as the analysis was performed on microglia



with a visible nucleus only, to ensure that the cell was actually microglia.

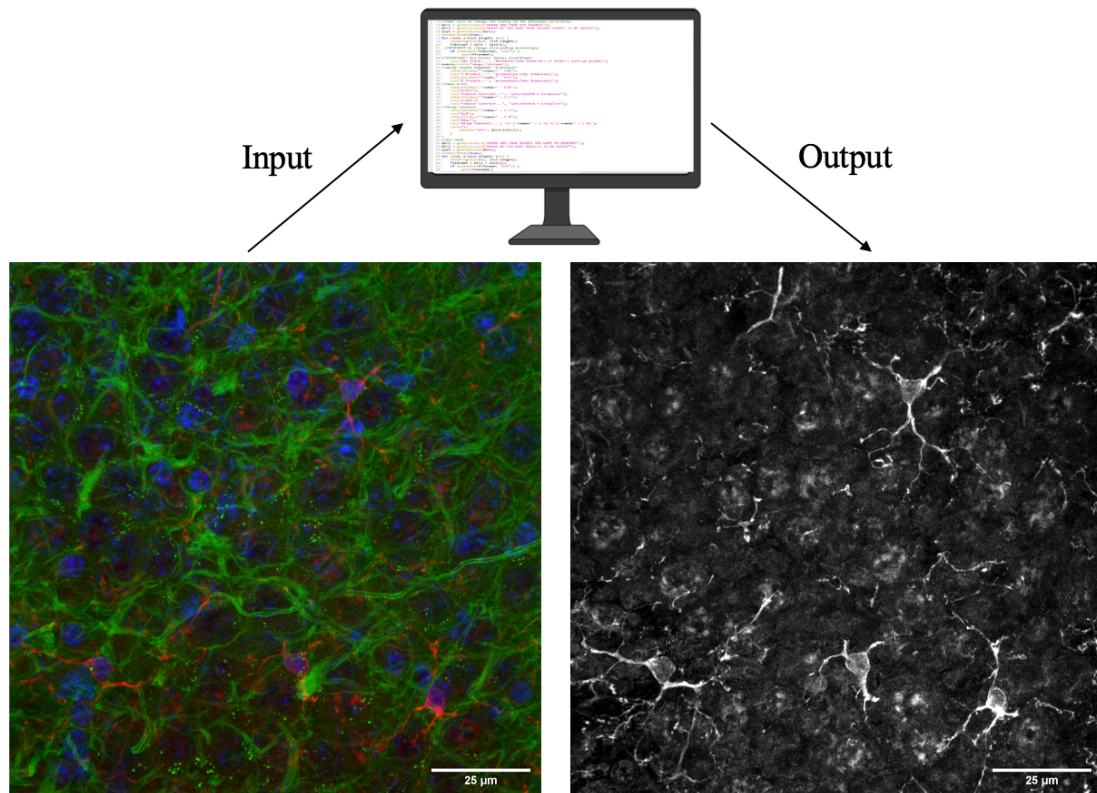


**Figure 14: Visualization of the first macro to extract Iba1 and DAPI channels.**

*Confocal images with 4 channels were run through the macro and the two channels for Iba1 and DAPI were merged and from these merged 2D projection, grey scale images with light cells on a dark background were created. Scale bar = 25 µm.*

As a control that only Iba1+ and DAPI+ microglia were marked, a second macro (figure 15) was run to form red (microglia) and blue (nuclei) 16-bit images using “split channel” and merging channels for Iba1 and DAPI together as red and blue. The images were used to compare with the greyscale images, as a visual (manual) control that all Iba1+ and DAPI+ microglia were marked and counted.

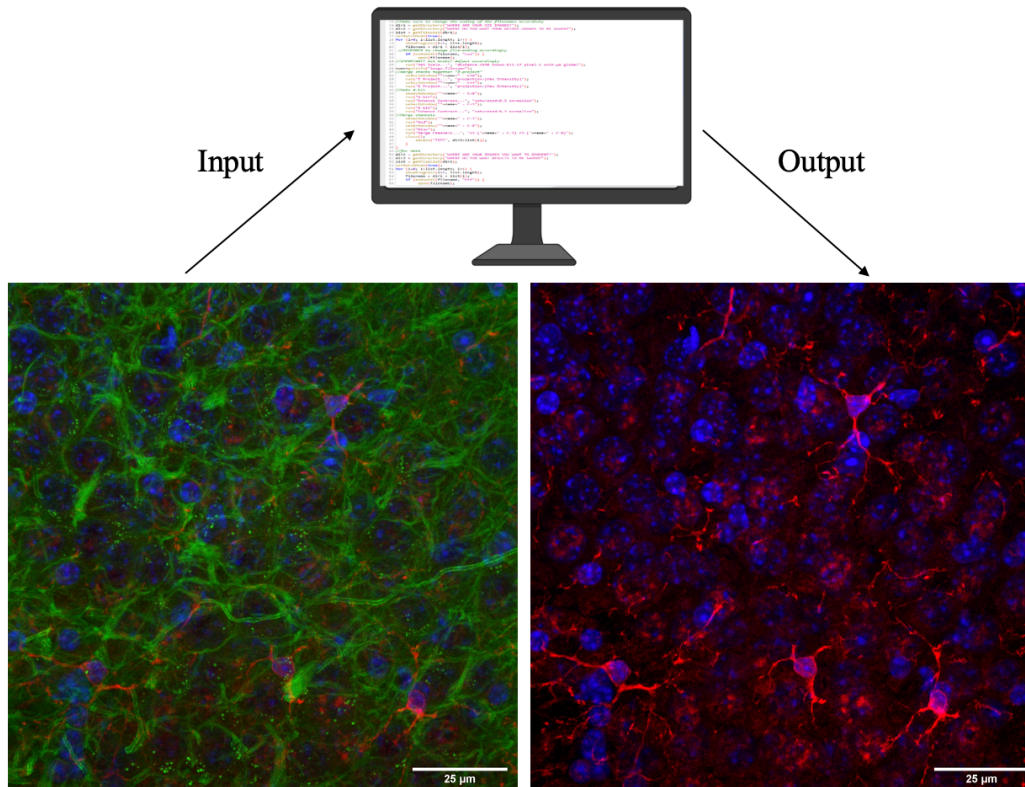


**Figure 15: Visualization of microglia and nuclei staining in mouse brain.**

A macro was used to merge the red and blue channels together, showing DAPI+ and Iba1+ microglia. This was used to visually compare with the grey-scale images where both nuclei and microglia processes were white, to ensure only microglia with nuclei within the soma were included. Scale bar = 25  $\mu\text{m}$ .

### 3.11.2 Segmentation of microglia

The microglia were segmented from the background by using Fiji software with a third macro (figure 16) which adjusted the threshold (67-255) and used pixel classification to create ROIs (individual microglia containing nuclei within the soma). Only structures between the size of 30-200  $\mu\text{m}^2$  were detected by the macro to avoid bringing small or large segmented processes without nuclei further in the analysis. When ROIs and area per ROI was obtained, manual reconstruction and quantification of the microglia cells were performed.

Despite removal of microglial fragments and non-microglial nuclei by the mentioned macros, the images still contained quite a bit of labeled structures and/or background labeling. Due to this, manual reconstruction was necessary to obtain all microglial cells, and delete ROIs that did not contain microglia with nuclei. The manual marking of microglia was performed by adjusting “Threshold” on the 8-bit greyscale images. By comparing the greyscale image to the corresponding red and blue image, the threshold was adjusted, based on the image intensity histogram, until the microglia cells were marked red. But, by only regulating threshold,

processes may be missed or gaps between crossing processes may be filled resulting in a false area and structure of the microglia. Therefore, after applying a threshold value, the “pencil”-function was used to manually add missing parts of the microglia or remove background attached to the microglia. When the microglia were correctly marked compared to the original confocal image, the “wand”-function was used to add the microglia as a “ROI”. The workflow for creating images containing masks of microglia is shown in figure 16.

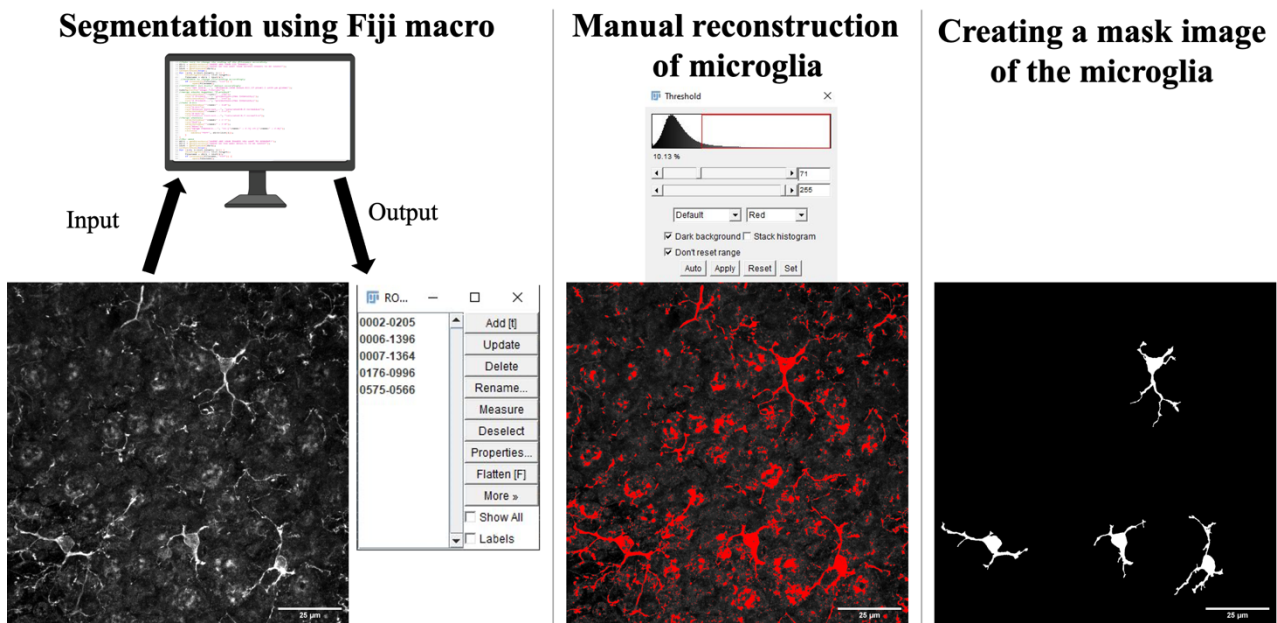


**Figure 16: Segmentation of microglia.**

*A macro was run to create ROI windows for the images; however, fragments of microglia were also marked as ROIs. Therefore, manually reconstruction was performed by adjusting the threshold and correctly mark the microglia. Finally, mask images of the microglia cells, like the one shown to the right in this figure, was created. Scale bar = 25 µm.*

### 3.11.3 Skeletonize

To investigate the degree of microglial activation, the last macro used the plugin “skeletonize 2D/3D” followed by “Analyze skeleton (2D/3D)” to create skeletons of microglia (figure 17).

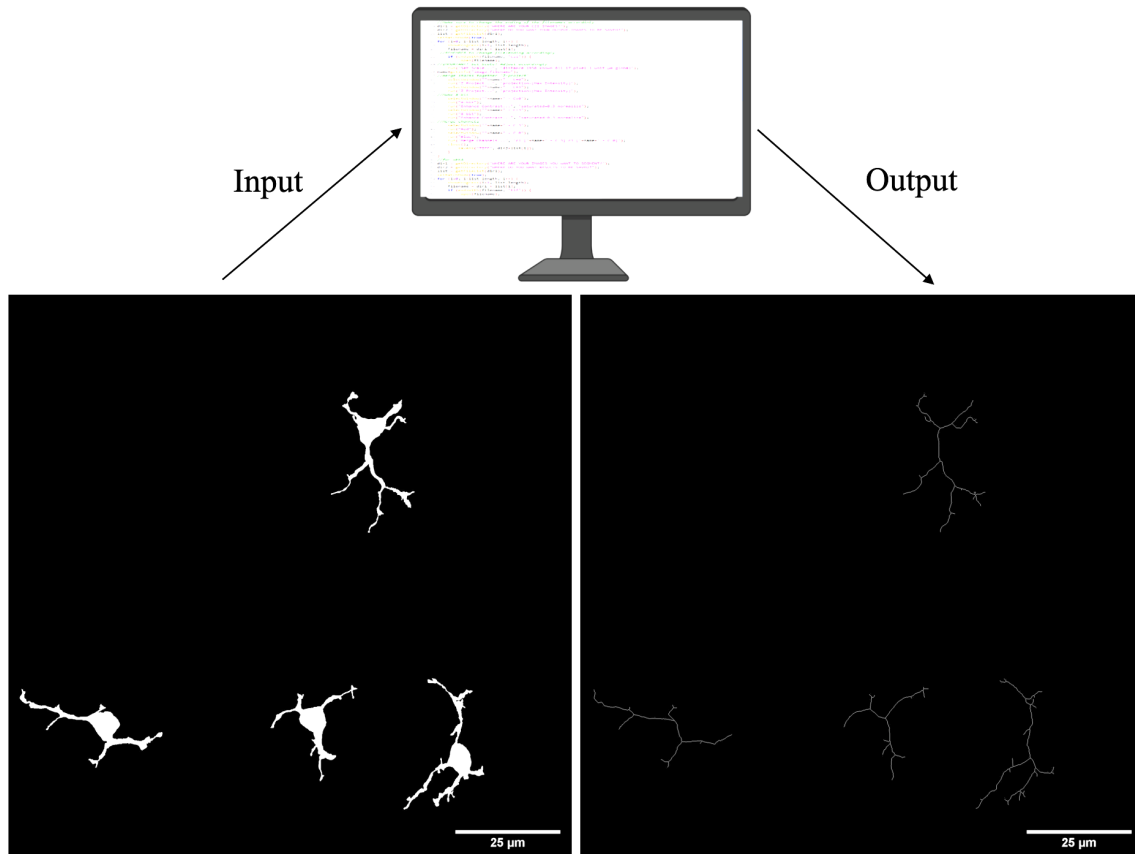


**Figure 17: Skeletonize.**

The plugin “Skeletonize 2D/3D” was used on the masked images to create a skeletonized form of the microglia cells. The skeletonized images were used for further analysis. Scale bar = 25 $\mu$ m.

After running the skeletonize macro, images with skeletonized microglia were created and the “Analyze skeleton (2D/3D)” plugin identified the branches (orange in figure 18) as microglial processes, junctions (purple in figure 18), as points where two branches split, and end-point voxels (blue in figure 18) as the endpoint of a branch. The count of branches, junctions and end-point voxels combined were used to assess degree of microglia activation.

After the “Analyze skeleton (2D/3D)” macro was performed on the skeleton images, a “Result” window was made for each image, as shown in figure 18. To study microglia structure, either at resting state or activated, three parameters were measured: Average branches, average junctions, and average end-point voxels. The code script for all macros is given in the appendix; figure 46-48).

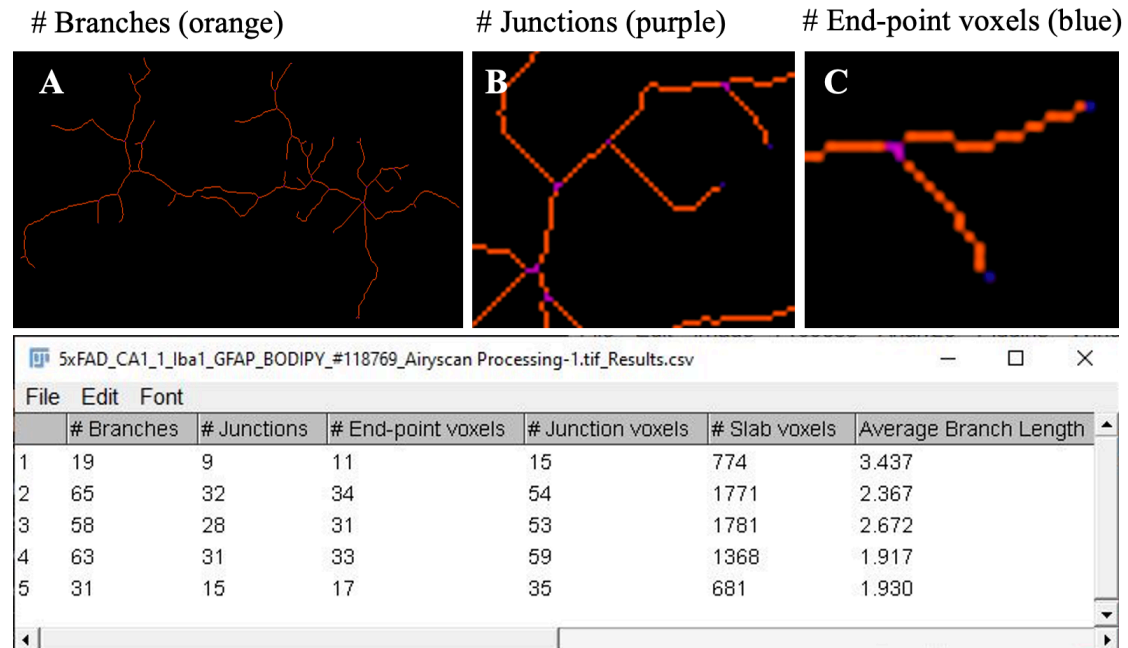


**Figure 18: Result from analysis.**

Example of branches (red) (A), junctions (purple) (B), end-point voxels (blue) (C) and a result window after skeleton analysis of one image with five microglia (each line represents data from one microglia).

### 3.11.4 Quantitative analysis of lipid droplets

After creating ROIs and analyzing the microglial cells, BODIPY+ lipid droplets in the microglial cells were quantified manually. Although I performed the immunolabeling and contributed to the initial analysis of LD, most of these analyses were performed by Gezime Seferi. Identification of LD stained with BODIPY was based on their abundant fluorescence intensity maxima and their circular shapes. In the brain, however, BODIPY also label the lipid-rich myelin.

The raw confocal images were opened with Fiji and the channels for DAPI and GFAP were removed. The channel for Iba1 were made red by using “lookup Tables” in Fiji before being “flattened” to a 2D image with maximum intensity using Z-projection. The channel for BODIPY was also “flattened” by Z-projection, followed by merging the BODIPY (green) and Iba1(red) channels together to a 2D image. The previous ROIs made for each microglia were used to create a new individually mask image for every microglia, now containing only a single green (BODIPY) and red (Iba1) microglia per image. LD were visible as green circles with intense fluorescence (figure 19). To ensure that only LD was counted and analyzed, the raw confocal images was opened with ZEISS Efficient Navigation (ZEN) imaging software (Carl Zeiss Microscopy, version 3.0 blue edition, Germany). The z-stack image was then used

to verify the 3D spherical structure of the LD that each LD included in the analysis was localized within the borders of the microglia. If the green sphere appeared to “move” when going through the z-stack, it was considered as a part of the myelin and not as a LD. These were excluded from the analysis.

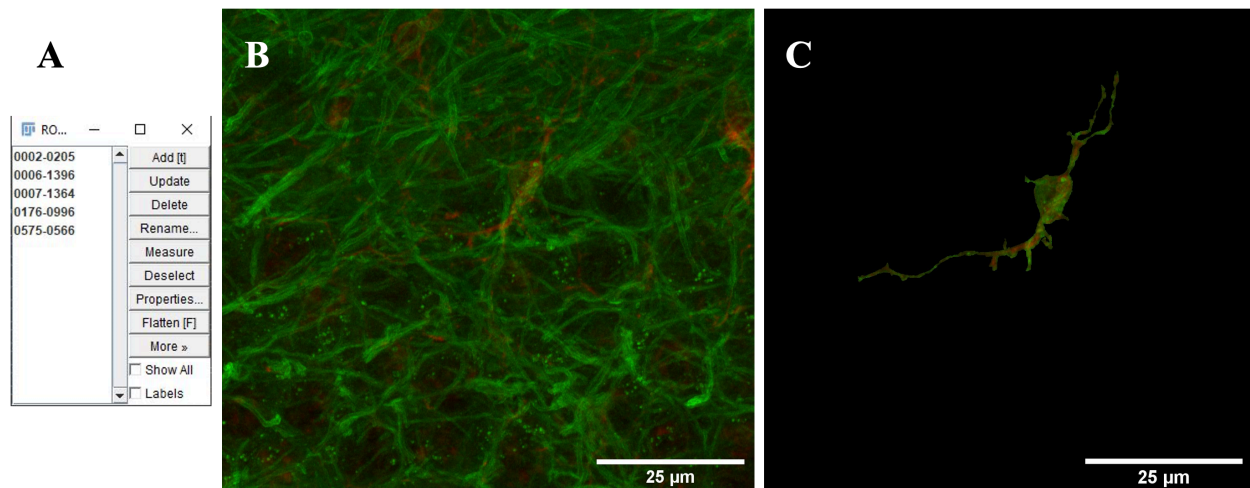


**Figure 19: Visualization of how a masked image was created from the raw image using previous ROI.**  
**A)** ROI windows for microglia were used to make new individual masked images from microglia with BODIPY and Iba1 channels. **B)** Z-projection images of BODIPY and Iba1 channels merged together to identify any lipid-droplet-containing microglia. **C)** Images with isolated microglia were created. This mask from one microglia is containing LD within its soma. Scale bar = 25  $\mu$ m

If the microglia contained any LD, the channels were split (after creating the microglia mask) using “split channels” and the 2D image for BODIPY were adjusted to an 8-bit greyscale image. In the greyscale image the LD were shown in white on a dark background. The “Threshold” function was then used to mark the LD inside the microglia, by adjusting the intensity histogram. The threshold was applied, creating a black (LD and background noise) and white (background) image. The LD were counted, marked as ROIs using the “wand” function and the area of each LD was measured.

### 3.12 Statistics

All statistical analyses were performed by GraphPad Prism Version 9.0 or Microsoft Excel. The value “n” represents the number of animals. For comparison of two groups, statistical significance was analyzed by unpaired students t-test when the data met the requirement for normal distribution and equal variance. The datasets that did not meet the requirement for normal distribution and/or equal variance were analyzed using the non-parametric Mann-Whitney U test. For comparison of more than two groups, statistical significance was

analyzed by one-way analysis of variance (ANOVA) when the dataset was normally distributed and had equal variance, and further analyzed using Tukey's post hoc test. The non-parametric Kruskal-Wallis test was used for datasets that did not meet the requirement for normal distribution and/or equal variance, and further analyzed using Dunn's multiple comparisons test. P-values  $< 0.05$  was considered statistically significant. Data are presented as mean  $\pm$  standard deviation (SD). Normal distribution was tested using the normal distribution test; Shapiro-Wilk test and by creating quantile-quantile plots (Q-Q plots) to check if the points formed a roughly straight line. It was considered equal variance when a p-value  $> 0.05$  in the F-test (for two groups) or Brown-Forsythe test (for more than two groups) was obtained. Outliers were removed; an animal was considered an outlier if it gave a value that deviated from the average by more than 2 x the SD (average  $\pm 2*SD$ ).

## 4 Results

### 4.1 Genotyping

Genotyping of mice from heterogenous breeding of *db/+* mice resulted in one or two DNA bands: one at 264 bp (representing wild-type allele) and/or one at 406 bp (representing mutant allele) in addition to a DNA band at 610 bp (non-allele-specific positive control band). Wt mice, expressing the wild-type allele were recognized by two bands– at 264 bp and 610 bp– for the non-allele-specific control band. Homozygous *db/db* mice, expressing the mutant allele were identified by two bands– at 406 bp and 610 bp–, while *db/+* mice, expressing both alleles were recognized by the presence of bands at 264 bp and 406 bp in addition to the positive control band at 610 bp. An example of a result from genotyping with gel electrophoresis containing the three genotypes is shown in figure 20. Homozygous *db/db* mice and heterozygous *db/+* mice were used for experiments.

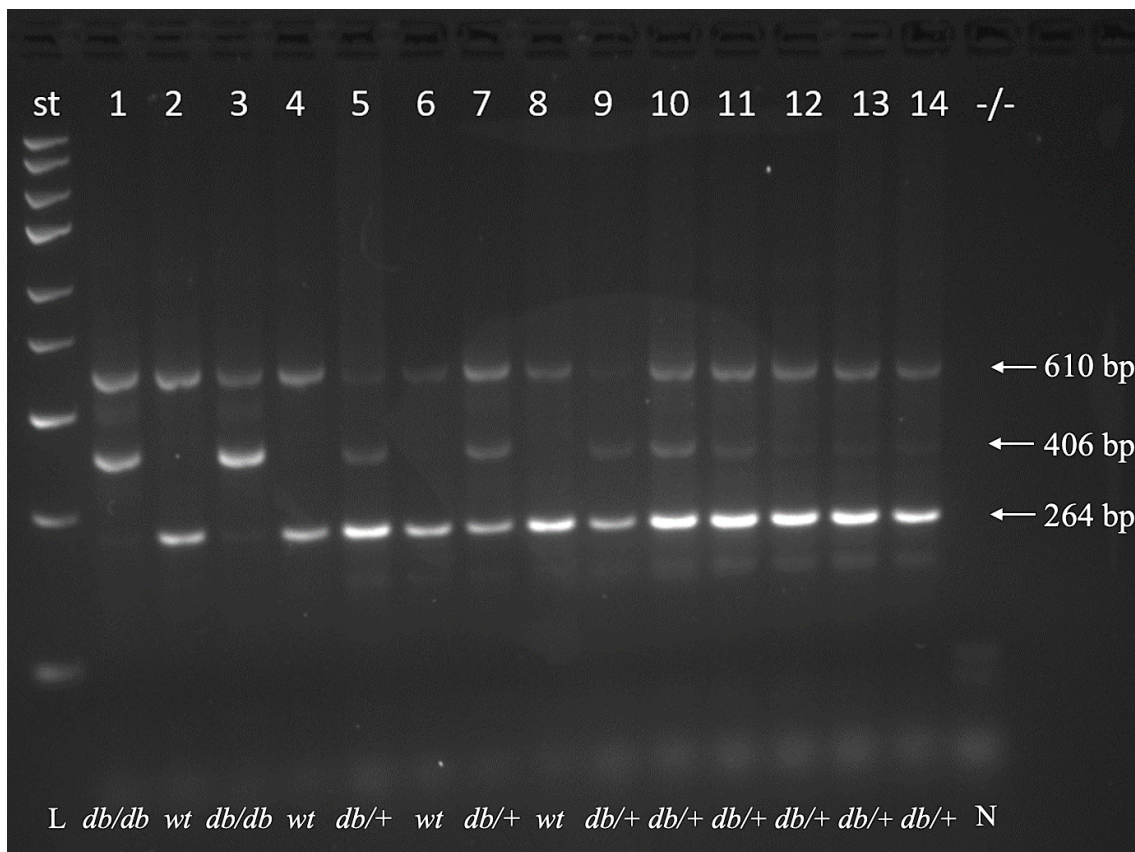


**Figure 20: Genotyping of mice using gel electrophoresis.**

Visualization of an agarose gel, with PCR products (DNA samples) filled in the wells, after current was applied. The DNA ladder with samples of known bp were added in the well labeled “st” and the negative control were added in the lane labeled N. Arrows indicate the size of the PCR products visualized in the gel. Wt mice were



identified as having visible bands at 610 bp and 264 bp (indicated by upper and lower arrow and the lanes labeled “wt”), *db/+* mice were identified as having all bands; 610 bp, 406 bp and 264 bp bands (indicated by all arrows and the lanes labeled “*db/+*”). The *db/db* mice were identified by the display of two bands; one at 610 bp and one at 406 bp (indicated by the two upper arrows and the lanes labeled “*db/db*”). Annotations: *st* (standard); *L* (Ladder); *wt* (wild type); *N* (Negative control).

## 4.2 Body weight

The mice (*db/db* and *db/+* mice) who participated in the exercise regime and behavioral experiments (interval regime, MWM and open field) were weighed weekly during the active parts of the experiments (a total of 8 weeks) with the exception of 6 sedentary *db/+* mice. These 6 sedentary *db/+* mice only performed the MWM test and their wellbeing was monitored by the personnel working at the animal facility at the Department of Comparative Medicine, UiO. The body weight in this study was used to monitor the animal’s health, investigate whether high interval exercise had impact on the body weight, and was also used to calculate the body composition (fat percentage, lean percentage and free body fluid percentage) of the animals. The development in body weight for each group; *db/+* sedentary, *db/+* exercised, *db/db* sedentary and *db/db* exercised are shown graphically in figure 21.

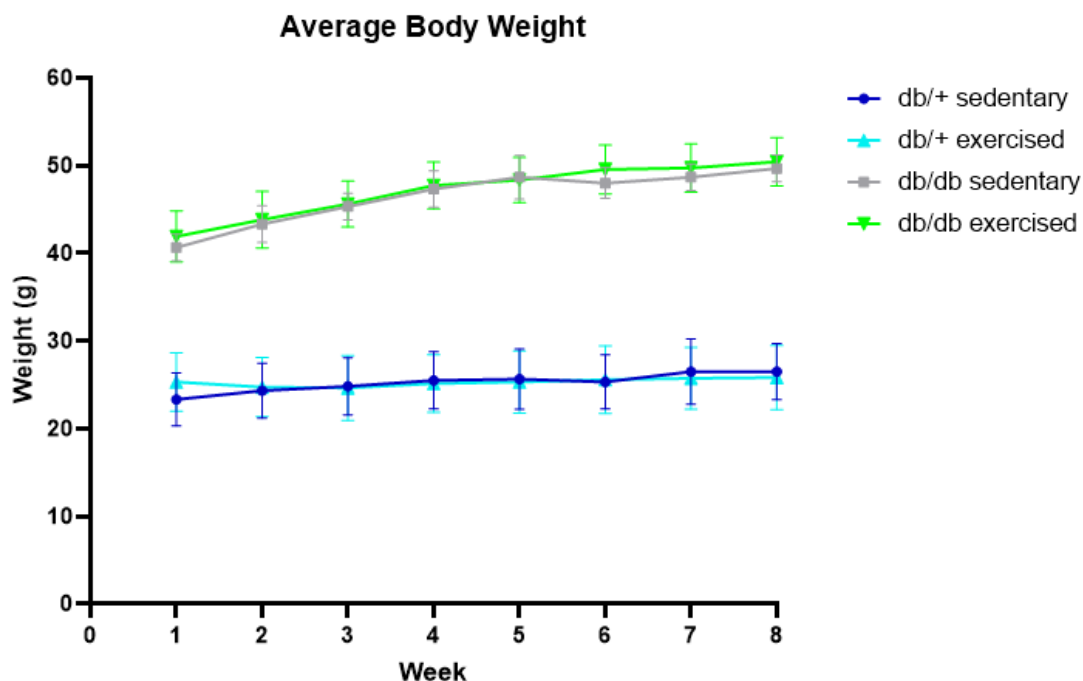


**Figure 21: Average body weight of the mice included in the intervention period.**

Body weight was measured once a week for a total of 8 weeks. Already from the start of the experiment the *db/db* mice (*db/db* sedentary; grey, *db/db* exercised; green) had a particularly high body weight compared to the *db/+* mice (*db/+* sedentary; blue, *db/+* exercised; turquoise) and they also had a gradual increase in their body weight throughout the study. The weight of the *db/+* mice was more constant during the 8 weeks and, despite high intensity intervals, the exercise groups did not differ from their corresponding sedentary groups. Data are

presented as mean  $\pm$  SD. Number of animals: *db/+* sedentary ( $n=12$ ), *db/+* exercised ( $n=12$ ), *db/db* sedentary ( $n=3$ ) and *db/db* exercised ( $n=11$ ).

As expected, *db/db* mice had significantly higher bodyweight than the *db/+* mice throughout the experiment ( $p < 0.0001$ , Kruskal-Wallis test, GraphPad Prism). The *db/+* exercised and *db/+* sedentary mice had fairly equal body weight during the 8-week time. At the start of the study, the average weight was slightly higher for the *db/+* exercised group, but during the exercise intervention the weight evened out and at week 7 and 8 the weight was slightly higher in the *db/+* sedentary mice. There was little difference in the body weight between the *db/db* groups and both *db/db* sedentary and *db/db* exercised showed a nearly 10 % of weight gain during the intervention period, despite high interval exercise. Although the *db/+* mice had small variations in their body weight, the *db/db* mice showed a steady increase, which fits to the extreme animal model where the mutation in the *Lepr* cause the animals to eat excessively (Peng et al., 2018). Average increase in body weight over the 8 weeks were  $3.17 \pm 1.07$  g for the *db/+* sedentary mice,  $0.5 \pm 0.43$  g for the *db/+* exercised mice,  $9.00 \pm 3.11$  g for the *db/db* sedentary mice and  $8.55 \pm 3.07$  g for the *db/db* exercised mice (average  $\pm$  SD).

### 4.3 Body composition

To investigate the development in the body composition during high interval exercise and observe the differences between the treatment groups, body composition measurements were taken once a week for a total of 8 weeks. Measurements were performed on 6 of the *db/+* sedentary mice, 12 *db/+* exercised mice, 3 *db/db* sedentary mice and 11 *db/db* exercised mice. The average percentage of “lean tissue” (e.g., muscles), fat, and fluid are shown in figure 22.

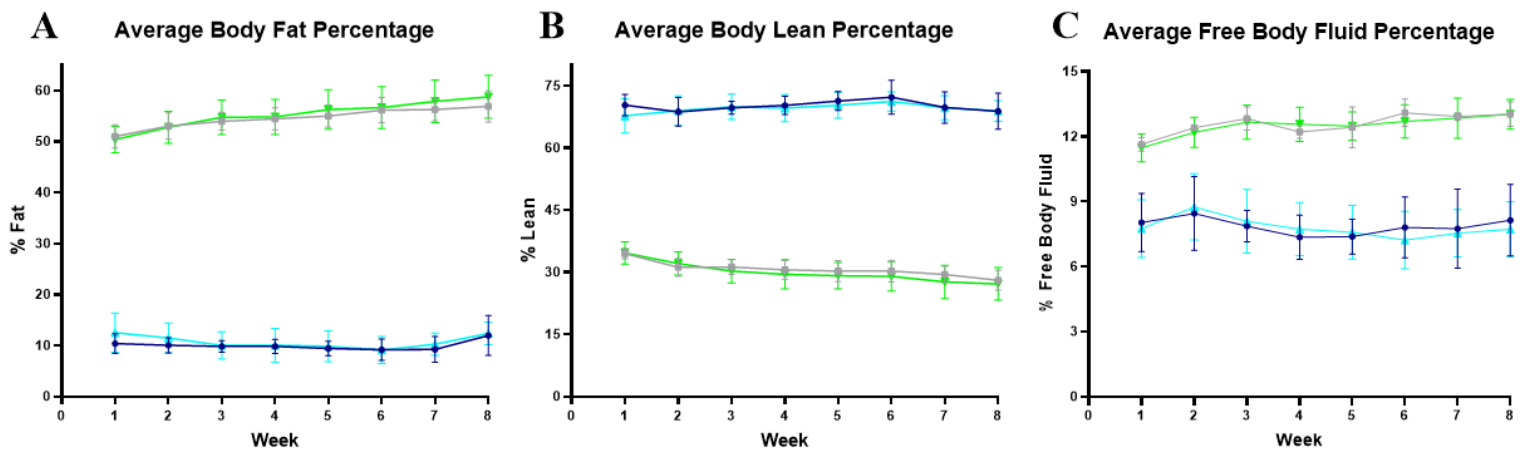


**Figure 22: Development in body composition throughout the intervention period.**

Body composition of the mice were measured once a week for a total of 8 weeks for: *db/db* sedentary (grey; n= 3), *db/db* exercised (green; n= 11), *db/+* sedentary (blue; n= 12) and *db/+* exercised (turquoise; n= 12). **A)** The phenotype of the *db/db* mice was obvious at the start of the intervention period, as indicated by the higher percentage of body fat in the *db/db* mice compared to the *db/+* mice. The *db/db* mice gradually increased their percentage of fat throughout the experiment, and despite high intensity exercise 5 days a week, the *db/db* exercise group did not deviate from the *db/db* sedentary group. The percentage of body fat in the *db/+* mice was constant throughout the intervention period, both in exercised and sedentary mice. **B)** In line with the high percentage of fat in the *db/db* mice, their percentage of “lean tissues” was lower than in the *db/+* groups and decreased slightly though the intervention period. The *db/+* groups did not change their “lean” content though the intervention. Exercise did not affect the percentage of lean mass in any of the genotypes. **C)** Free body fluid was higher in *db/db* mice at the start of the experiment compared to the *db/+*, and despite small week-to-week fluctuation, *db/db* mice showed a slight increase in body fluids through the intervention period. The *db/+* mice did not change their content of free body fluids through the intervention period. The content of free body fluids was unaffected by exercise in both genotypes. Data are presented as mean  $\pm$  SD.

The percentage of body fat in *db/+* mice remained steady throughout the intervention period and the *db/+* exercised mice did not deviate from the *db/+* sedentary mice. Already at 9-11 weeks of age the *db/db* mice had an average of over 50 % body fat and the percentage kept increasing during the next weeks. Interestingly, the percentage of body fat increased regardless of exercise (figure 22A). In addition to the increasing fat percentage in the *db/db* mice, the percentage of “lean” decreased over the 8 weeks, also for the exercised *db/db* mice (figure 22B). “Lean” tissues included the muscle mass which, despite high interval running with a 25-degree incline, decreased in percent for both *db/+* exercised and *db/db* exercised. The *db/db* mice had much lower lean percentage than the *db/+* mice. Exercise did not affect the lean mass resulting in no observed differences in percentage of lean between the same genotypes in the sedentary and exercised group. The *db/+* sedentary mice had higher percentage of body fluid than the *db/db* mice during the entire intervention time. The body fluid in the *db/+* mice stayed constant during the 8 weeks, although the *db/db* mice had a slight increase in the percentage of body fluid during the intervention period. No noteworthy differences of body fluid between the two *db/+* groups or between the two *db/db* groups were observed during the 8-week time (figure 22C).

## **4.4 Physical performance in the maximal exercise capacity test**

All the 23 mice in the exercise regime participated in the maximal exercise capacity test (MECT) every other week during the experiment. To study effect of high interval exercise on neuroinflammation in the mouse brain, all the mice ran at 80 % of their maximum capacity the entire intervention period. The average result from the MECT was therefore used to set

the running speed (80 % of their maximum capacity) for the next two weeks of intervals. The genotype of the mice affected the physical performance, where *db/+* mice had a much higher running speed (and hence test duration) than the *db/db* mice, however, both genotypes improved their maximal capacity during the exercise period (figure 23).

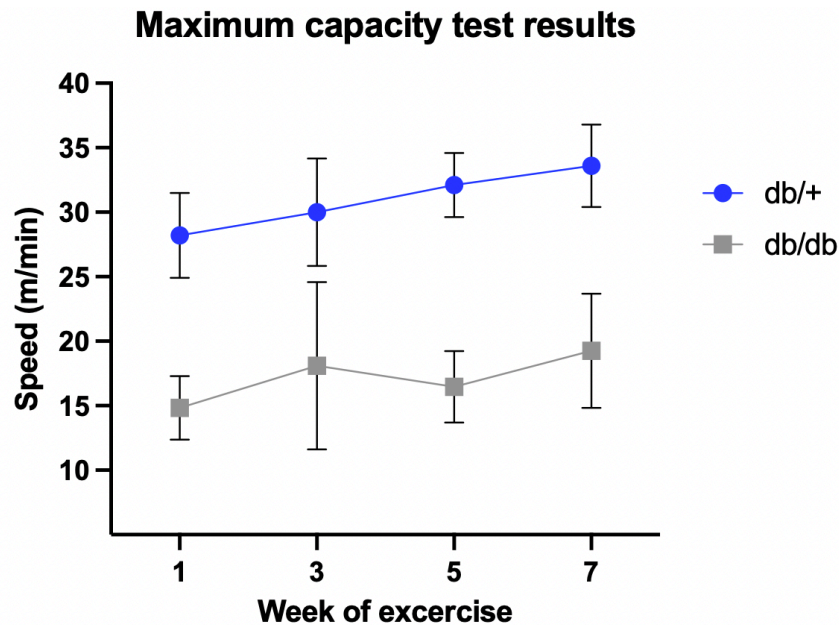


**Figure 23: Average results of maximal exercise capacity test.** The average performance in the maximum exercise capacity test over the 8-week intervention for the *db/+* (blue) and the *db/db* (grey) mice. During the period, the performance increased by 5.4 m/min for *db/+* and 4.5 m/min for *db/db* mice. As expected, the *db/+* mice ran at a higher speed (and, hence, for a longer time) in the MECT than the obese *db/db* mice. Data are presented as mean  $\pm$  SD. Number of animals included in the exercise regime throughout the study; *db/+* (n= 12), *db/db* (n= 11).

## 4.5 Open Field Exploration test

The open field test for used to assess locomotor activity and anxiety-like behavior. Therefore the test was separated in two parts: the first 10 minutes to assess anxiety-like behavior, and the last 50 minutes to assess spontaneous locomotor activity. The dataset for one of the *db/db* mouse was deleted by mistake during the open field testing. Therefore, only data from 16 *db/db* mice were assessed.

**Assessing anxiety-like behavior:** In the first 10 minutes of the test, the duration time in the center and periphery area was assessed to measure any anxiety behavior in the mice. There was no statistically significant difference between the genotypes in the center duration nor the peripheral duration. Although, the *db/db* mice tended to spend less time in the center zone ( $p=$

0.1108, unpaired students t-test, GraphPad Prism) and more time in the periphery area ( $p=0.0666$ , Mann-Whitney U test, GraphPad Prism) compared to the *db/+* mice (figure 24).

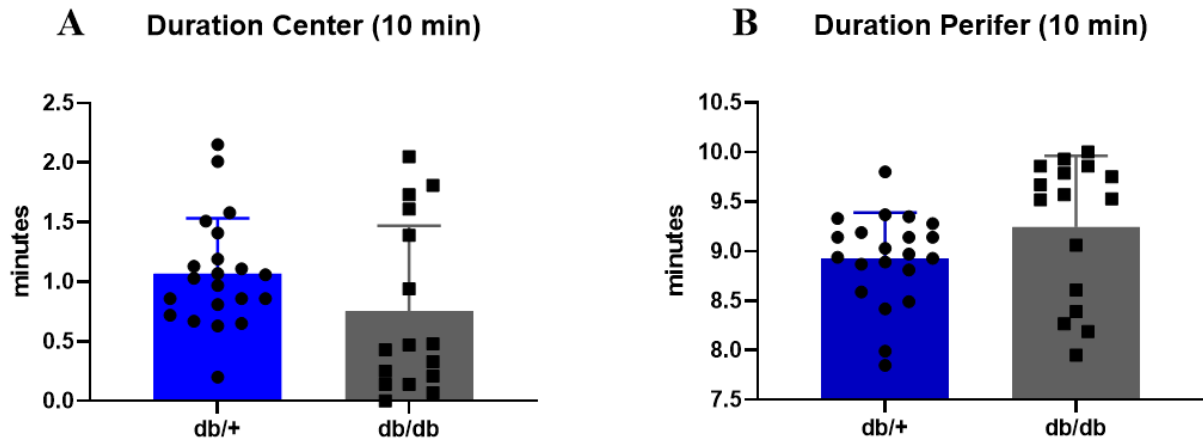


**Figure 24: Total duration from the first 10 minutes of the test spent in the center and the peripheral zone of the open field arena.**

The first 10 minutes of the open field test was assessed to investigate the anxiety state of the animals. **A)** The total duration spent in the center of the open field arena for *db/+* (blue) and *db/db* (grey) mice. The *db/db* mice tended to spend less time in the center zone compared to the *db/+* mice ( $p=0.1108$ , unpaired students t-test, GraphPad Prism). **B)** The total duration spent in the peripheral zone of the open field arena for *db/+* and *db/db* mice. The *db/db* mice tended to spend more time in the periphery zone compared to the *db/+* mice ( $p=0.0666$ , Mann-Whitney U test, GraphPad Prism). Annotations: Perifer; periphery. The bars represent mean  $\pm$  SD; individual values for each mouse are given as black circles or squares. Outliers removed: **A, B** (*db/+*;  $n=1$ ). Number of animals included: **A, B** (*db/+*;  $n=21$ , *db/db*;  $n=16$ ).

**Assessing spontaneous locomotor activity:** The last 50 minutes was considered as spontaneous movements of the mouse. The total distance traveled in both zones, as well as measurements for velocity, were assessed as metrics for spontaneous ambulatory activity. The *db/db* mice had significantly shorter distance traveled, in both the center zone ( $p<0.0001$ , unpaired students t-test, GraphPad Prism) and peripheral zone ( $p<0.0001$ , Mann-Whitney U test, GraphPad Prism) compared to the *db/+* mice during the 50 minutes in the arena (figure 25).

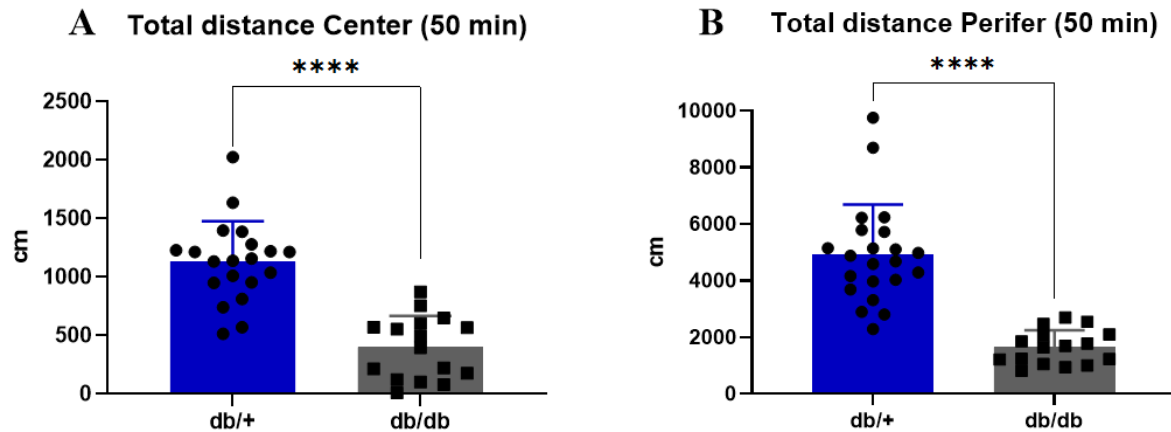


**Figure 25: Total distance traveled in the last 50 minutes of the open field test in the center and peripheral zone of the open field arena.**

The last 50 minutes of the open field test was assessed to investigate any differences in locomotor activity. Total distance in centimeters from the center zone and peripheral zone were combined and statistically analyzed to visualize any differences in ambulation. **A)** The total distance travelled in the center zone was significantly lower for the *db/db* mice (grey) compared to the *db/+* mice (blue) ( $p = <0.0001$ , unpaired students t-test, GraphPad Prism). **B)** The total distance travelled in the peripheral zone was significantly lower for the *db/db* mice compared to the *db/+* mice ( $p = <0.0001$ , Mann-Whitney U test, GraphPad Prism). Annotations: Perifer; periphery. The bars represent mean  $\pm$  SD; individual values for each mouse are given as black circles or squares. \*\*\*\*  $p < 0.0001$ . Outliers removed: **A** (*db/+*;  $n = 2$ ). Number of animals included: **A** (*db/+*;  $n = 20$ , *db/db*;  $n = 16$ ), **B** (*db/+*;  $n = 22$ , *db/db*;  $n = 16$ ).

To gain insight on the speed of the ambulatory movements, two parameters for velocity were assessed: (1) ambulatory episode average velocity, which represent the average speed (cm/s) when in motion, (2) ambulatory episode peak average velocity, which represents the speed (cm/s) of the mice's fastest movement. The *db/db* mice had significantly lower ambulatory episode average velocity in both the center area ( $p = <0.0001$ , unpaired students t-test, GraphPad Prism) and the peripheral area ( $p = <0.0001$ , unpaired students t-test, GraphPad Prism) compared to the *db/+* mice (figure 26A-B). The ambulatory episode peak average velocity was also significantly lower for the *db/db* mice in both center ( $p = <0.0001$ , unpaired students t-test, GraphPad Prism) and peripheral zone ( $p = <0.0001$ , Mann-Whitney U test, GraphPad Prism) compared to the *db/+* mice (figure 26C-D).

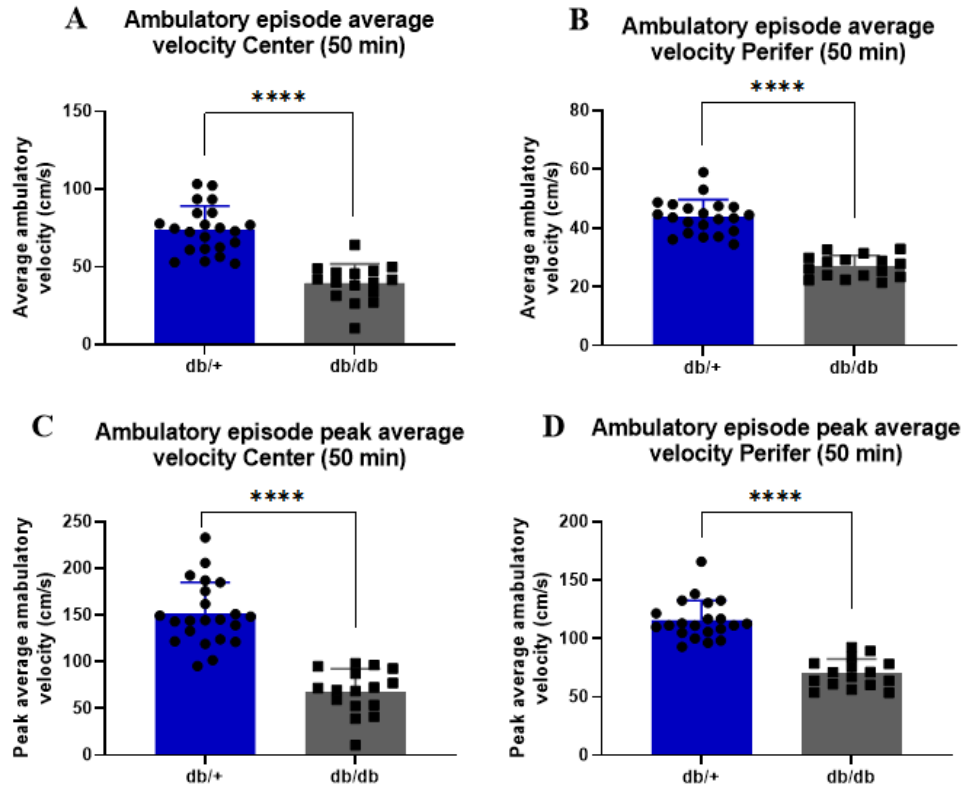


**Figure 26: Ambulatory episode average velocity and ambulatory episode peak average velocity in the last 50 minutes of the open field test from the center and peripheral zone of the open field arena.**  
**A)** The ambulatory episode average velocity in the center zone was significantly lower for the db/db mice (grey) compared to the db/+ mice (blue) ( $p = <0.0001$ , unpaired students *t*-test, GraphPad Prism). **B)** The ambulatory episode average velocity in the peripheral zone was significantly lower for the db/db mice compared to the db/+ mice ( $p = <0.0001$ , unpaired students *t*-test, GraphPad Prism). **C)** The ambulatory episode peak velocity in the center zone was significantly lower for the db/db mice compared to the db/+ mice ( $p = <0.0001$ , unpaired students *t*-test, GraphPad Prism). **D)** The ambulatory episode peak velocity in the peripheral zone was significantly lower for the db/db mice compared to the db/+ mice ( $p = <0.0001$ , Mann-Whitney *U* test, GraphPad Prism). Annotations: Perifer; periphery. The bars represent mean  $\pm$  SD; individual values for each mouse are given as black circles or squares. \*\*\*\*  $p < 0.0001$ . Outliers removed: **B, D** (db/+;  $n = 1$ ). Number of animals included: **A, C** (db/+;  $n = 22$ , db/db;  $n = 16$ ), **B, D** (db/+;  $n = 21$ , db/db;  $n = 16$ ).

## 4.6 Learning and memory performance in the Morris

### Water Maze test

The Morris water maze (MWM) test was performed for a total of 10 days, with 9 days of training followed by one day of a single probe trial. A total of 36 animals performed the MWM test: db/+ sedentary ( $n = 12$ ), db/+ exercised ( $n = 12$ ), db/db sedentary ( $n = 3$ ) and db/db exercised mice ( $n = 11$ ). For the first 9 days of the MWM test, each mouse swam 4 trials to learn and memorize the location of the platform located in the north zone. If the mouse found the platform within the 60-second trial, the time was stopped. Despite some day-to-day fluctuations, all groups improved their ability to find the platform, as expected (figure 27).

The db/db mice had a higher average test duration in the training days than the db/+ mice and

the *db/db* sedentary mice showed the smallest decrease in test duration indicating little learned behavior.

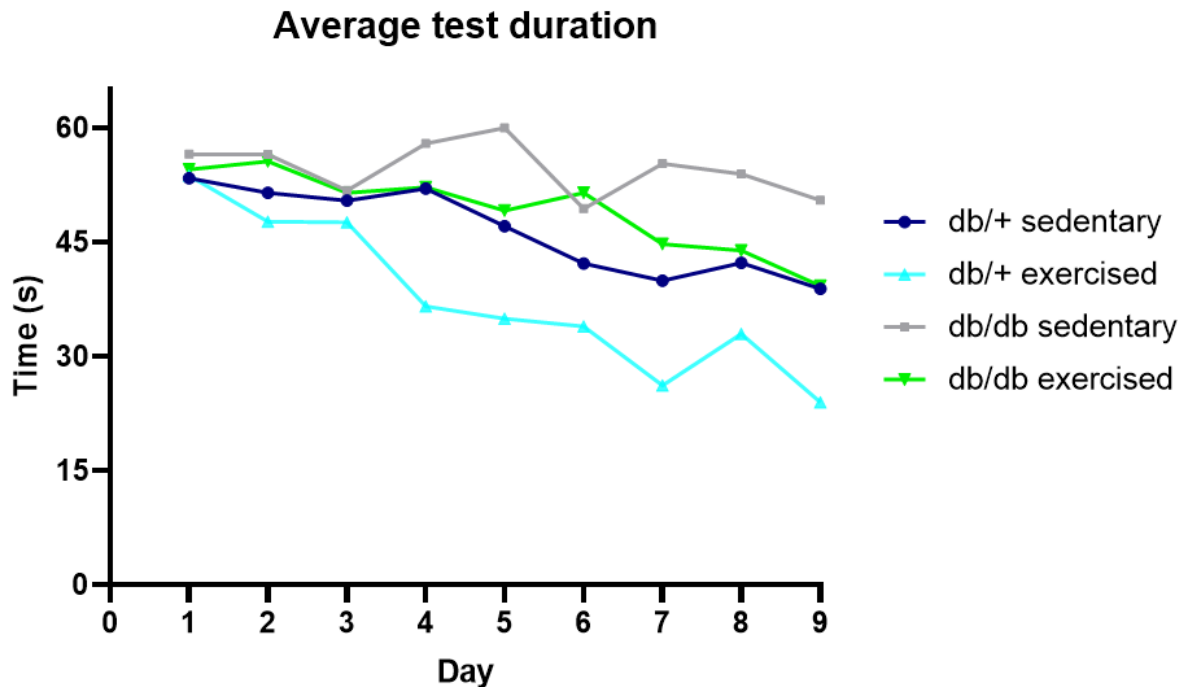


**Figure 27: Average test duration in the training days for the MWM test.**

During the 9 training days in the MWM test the animals swam 4 trials. The test duration represented the time used to find the platform and until they climbed on the platform. Animals who did not find the platform were placed on the platform by the operator after 60 seconds, which in their case represented the test duration. The graph shows the average of the 4 trials for each mouse in each experimental group; *db/+* sedentary (blue), *db/+* exercised (turquoise), *db/db* sedentary (grey), and *db/db* exercised (green). The test duration decreased for all groups during the training days, as an indication of learned behavior. The *db/db* sedentary mice had the highest test duration during the 9 days, followed by *db/db* exercised and *db/+* sedentary mice. The exercised *db/+* mice had the shortest test duration. Number of animals included: *db/+* sedentary ( $n=12$ ), *db/+* exercised ( $n=12$ ), *db/db* sedentary ( $n=3$ ) and *db/db* exercised ( $n=11$ ).

On the tenth day, the platform was removed, and only a single 60-second trial was performed by each mouse. Two of the *db/db* exercised mice were floating (just moving enough to keep their head above the water, but not actively swimming to search for the platform) for more than 30 seconds during the probe trial and were therefore excluded from the results. The ANYmaze software was tracking the animals making a track plot of the movement of the animals (figure 28). In general, the *db/+* animals had the longest tracked paths and presence in the north zone. The *db/+* exercised mice had the highest average presence in the peri-platform- and platform zone (as exemplified in figure 28B). The *db/db* sedentary mice were the treatment group with the least presence in the platform area (as exemplified in figure 28C).



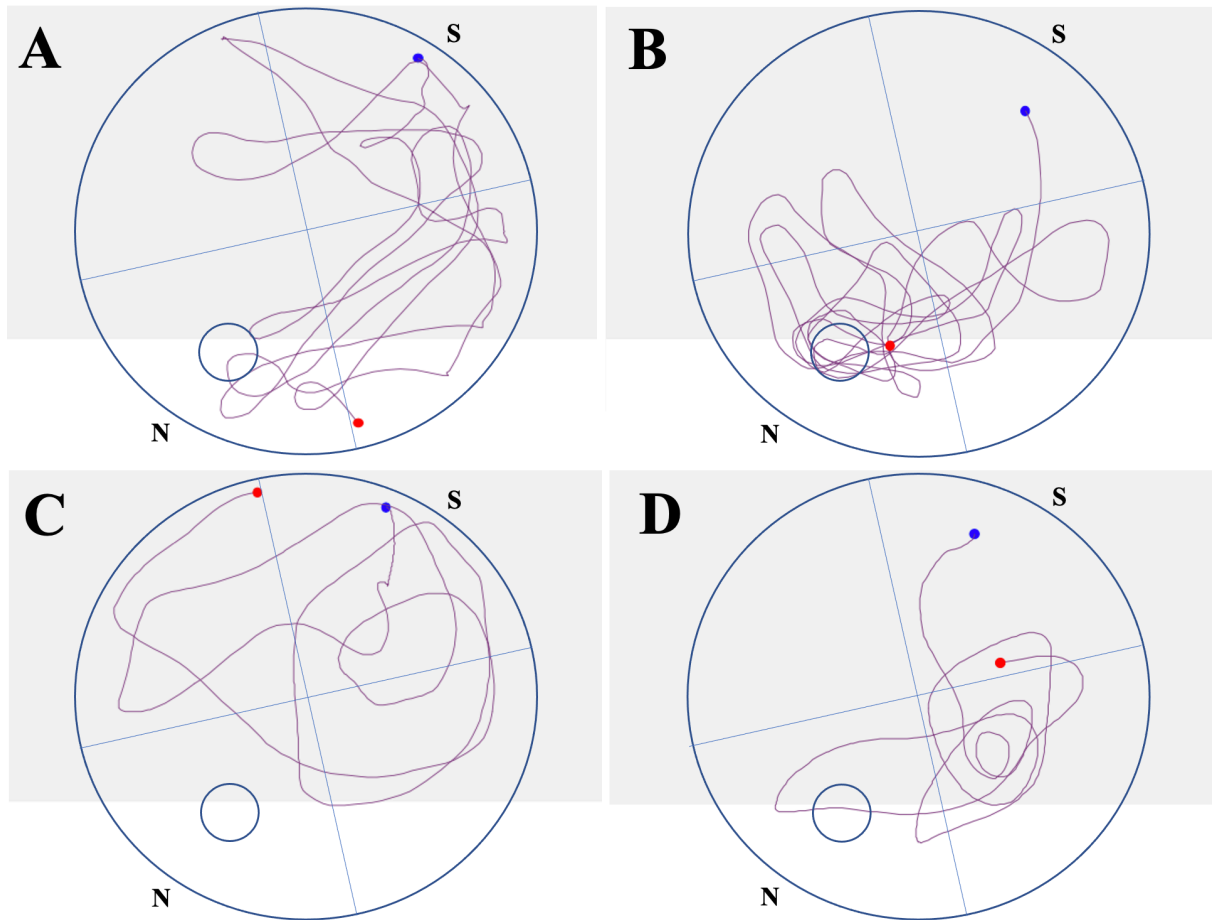


**Figure 28: Track plots showing the swimming path of the animals on the probe trial.**

The blue point indicates the track start (from south in the MWM pool) and the red point indicate the track end (after the single 60-second trial). The borders of the MWM arena (large circle) and the platform zone (small circle) are inserted by hand for illustration, and hence their location and size may not be 100 % accurate. The lines inside the MWM arena are to illustrate the approximate dimensions of the four quadrants. Representative track plots from a *db/+* sedentary mouse (**A**), a *db/+* exercised mouse (**B**), a *db/db* sedentary mouse (**C**), and a *db/db* exercised mouse (**D**) are presented. N= north zone; S= south zone.

At the probe trial, swimming speed, travel distance, latency to the first entry-, number of entries-, and time in the north zone-, peri-platform zone- and platform zone were used as parameters for learning and memory (figure 29, 30, 31, 32). Some of the mice did not enter all of the zones, and hence were given a 60-second latency time for the zone of interest. Average swimming speed (figure 29A) and distance travelled (figure 29B), together with the data from the open field test, was also used to interpret the MWM results.

The swimming speed of the *db/db* exercised mice was significantly lower than that of the *db/+* sedentary mice ( $p= 0.022$ , Kruskal-Wallis test, Dunn's test, GraphPad Prism) and the *db/+* exercised mice ( $p= 0.014$ , Kruskal-Wallis test, Dunn's test, GraphPad Prism) (figure 29A). As a reflection of the lower average path speed, the *db/db* exercised mice had considerably

less travel distance than the *db/+* sedentary ( $p=0.023$ , Kruskal-Wallis test, Dunn's test, GraphPad Prism) and the *db/+* exercised ( $p=0.015$ , Kruskal-Wallis test, Dunn's test, GraphPad Prism) (figure 29B). The sedentary *db/db* mice also had less average speed and distance travelled compared to the *db/+* mice, but this was not statistically significant; probably due to the low number of animals in the *db/db* sedentary group.

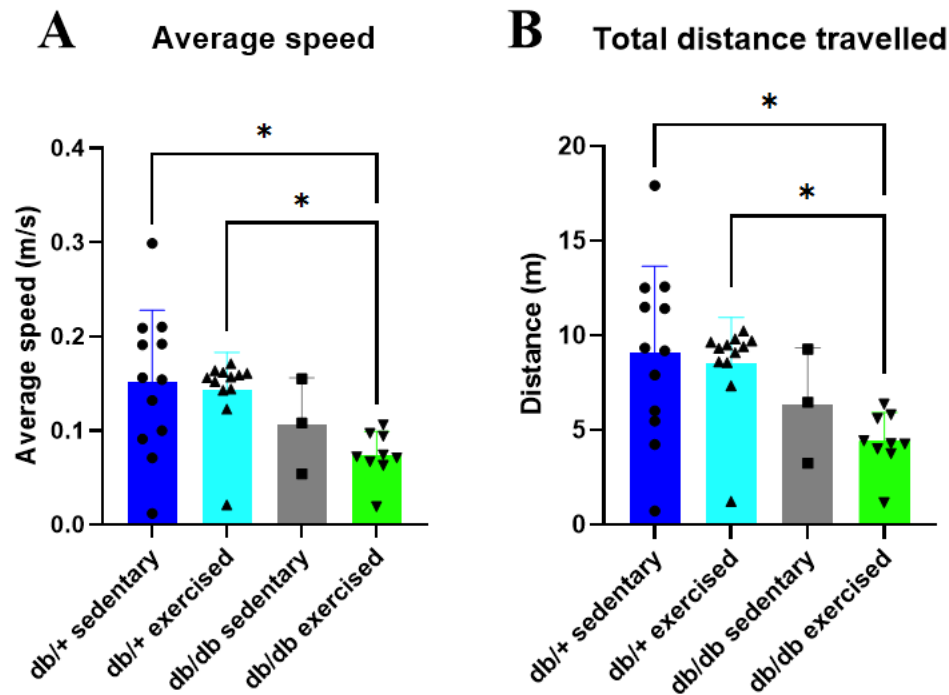


**Figure 29: Average swimming speed and total distance travelled for the animals at the MWM test day.** On the tenth day of the MWM test, the probe trial was performed where the platform was removed, and mice swam only once for 60 seconds. **A)** The average speed was significantly lower for the *db/db* exercised mice (green) than for the *db/+* sedentary mice (blue) ( $p=0.022$ ). The *db/+* exercised mice (turquoise) also had a significantly higher swimming speed than the *db/db* exercised ( $p=0.014$ ). **B)** Similarly, the total distance travelled was significantly lower in the *db/db* exercised than in the *db/+* sedentary mice ( $p=0.023$ ) and the *db/+* exercised mice ( $p=0.015$ , Kruskal-Wallis test, Dunn's multiple comparisons test, GraphPad Prism). The bars represent mean  $\pm$  SD; individual values for each mouse are given as black circles, upward triangles, squares, or downward triangles. \*  $p < 0.05$ . Number of animals included: *db/+* sedentary ( $n=12$ ), *db/+* exercised ( $n=12$ ), *db/db* sedentary ( $n=3$ ) and *db/db* exercised ( $n=9$ ).

The platform zone (platform location during the training sessions) was within the north zone, hence the time spent in the north zone at the probe trial (figure 30C) may indicate that the mouse was searching for the platform. A low latency to the first entry- in addition to a high number of entries to- or a high percentage of time spent in the north zone may indicate that the mouse had learned that the platform location was within that zone. These three parameters were therefore some of the used metrics of learning.

Both of the *db/+* groups had <13 seconds as average latency to the first entry to the north zone (figure 30A). The three *db/db* sedentary mice had the lowest latency to the first entry to the north zone and had a statistically lower latency than the *db/db* exercised mice ( $p=0.015$ , Kruskal-Wallis test, Dunn's test, GraphPad Prism). The *db/+* exercised mice entered the north zone a significantly higher number of times than the *db/+* sedentary and the *db/db* sedentary mice ( $p=0.037$  and  $p=0.026$ , respectively; Kruskal-Wallis, Dunn's test, GraphPad Prism; figure 30B). The *db/+* exercised mice spent the most time in the north zone (figure 30C), but this did not reach statistical significance.

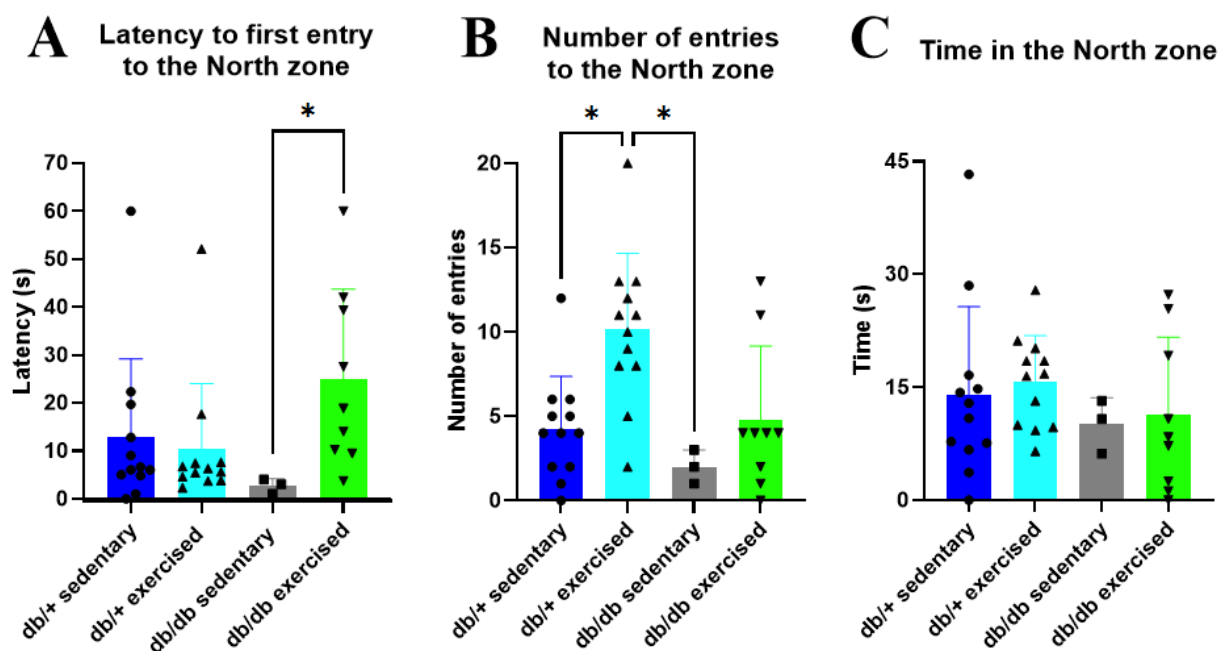


**Figure 30: Average latency to the first entry to the north zone, number of entries to the north zone and time in the North zone during the test day at MWM.**

**A)** The average latency to the first entry to the north zone ( $p=0.015$ , Kruskal-Wallis test, GraphPad Prism) was significantly lower for the *db/db* exercised mice (green) than the *db/db* sedentary mice (grey) ( $p=0.016$ , Dunn's multiple comparisons test, GraphPad Prism). **B)** The average number of entries to the north zone ( $p=0.004$ , Kruskal-Wallis test, GraphPad Prism) were significantly higher for the *db/+* exercised mice (turquoise) compared to the *db/+* sedentary (blue) ( $p=0.037$ ) and the *db/db* sedentary mice ( $p=0.026$ , Dunn's multiple comparisons test, GraphPad Prism). **C)** There were no statistically significant differences between the four groups in the average time spent in the north zone ( $p=0.404$ , Kruskal-Wallis test, GraphPad Prism). The bars represent mean  $\pm$  SD; individual values for each mouse are given as black circles, upward triangles, squares, or downward triangles. \*  $p < 0.05$ . Number of animals included: *db/+* sedentary ( $n=12$ ), *db/+* exercised ( $n=12$ ), *db/db* sedentary ( $n=3$ ), *db/db* exercised ( $n=9$ ).

The peri-platform zone was defined as the 3 cm surrounding the platform zone, hence a lot of presence in this area was measured as an attempt to find the platform zone. The *db/+* mice (exercised and sedentary) had the lowest average latency to the first entry to the peri-platform zone, while the *db/db* exercised mice had the longest latency time before their first entry to

the peri-platform zone (figure 31A). The *db/db* sedentary had the lowest average number of entries to the peri-platform zone, but this was not statistically lower than what was observed for the *db/db* exercised mice. The *db/+* exercised mice had a significantly higher number of entries than the *db/+* sedentary mice ( $p=0.042$ , Kruskal-Wallis, Dunn's test, GraphPad Prism) (figure 31B). Although no statistical differences were found between the groups in the time spent in the peri-platform zone, the two exercised groups had the highest average of time in the peri-platform zone (figure 31C). On average, the *db/db* sedentary spent slightly less time in the peri-platform zone than the *db/+* sedentary mice.

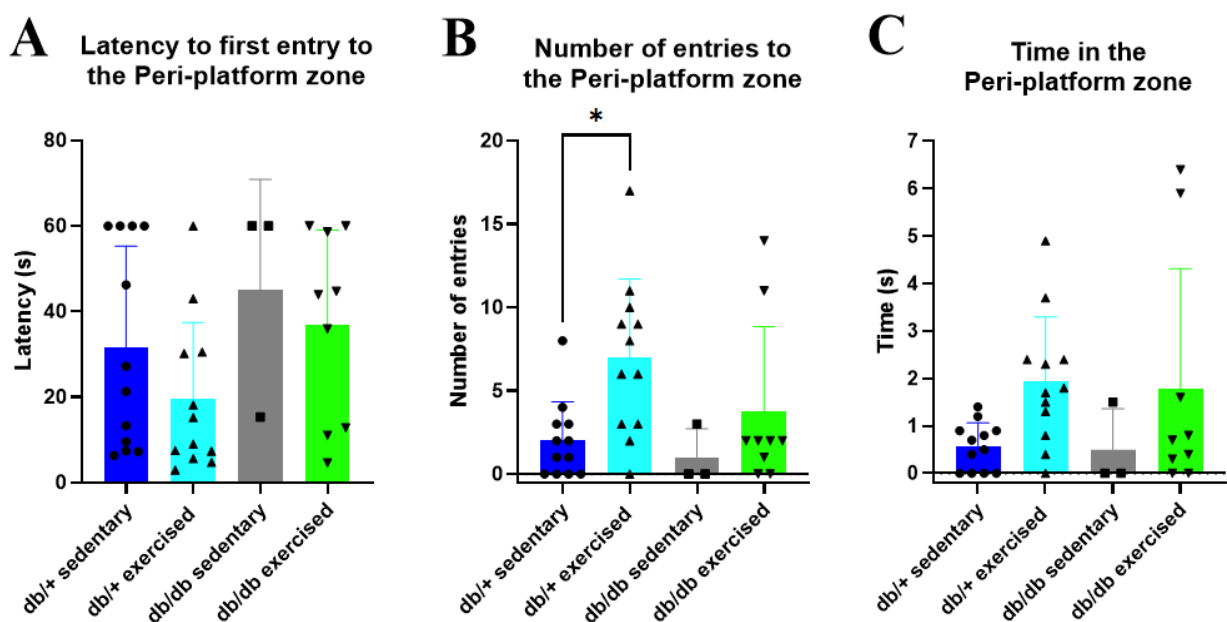


**Figure 31: Average latency to the first entry to the peri-platform zone, number of entries to the peri-platform zone and time spent in the peri-platform zone during the MWM test day.**

**A)** During the 60-second test time, the *db/db* sedentary (grey) had the highest latency to the first entry to the peri-platform zone ( $45.1s \pm 25.8$ ). The average latency for the three other groups; *db/+* sedentary (blue), *db/+* exercised (turquoise) and *db/db* exercised (green), were all  $< 37$  seconds. **B)** The average number of entries to the peri-platform zone was significantly higher for the *db/+* exercised mice than the *db/+* sedentary mice ( $p=0.042$ , Dunn's multiple comparisons test, GraphPad Prism). **C)** The average time spent in the platform zone was higher for the exercised mice compared to the sedentary mice. The *db/+* exercised mice spent more time in the peri-platform zone than *db/+* sedentary ( $p=0.053$ ) and *db/db* sedentary ( $p=0.301$ ) but this was not statistically significant. The bars represent mean  $\pm$  SD; individual values for each mouse are given as black circles, upward triangles, squares, or downward triangles. \*  $p < 0.05$ . Number of animals included: *db/+* sedentary ( $n=12$ ), *db/+* exercised ( $n=12$ ), *db/db* sedentary ( $n=3$ ), *db/db* exercised ( $n=9$ ).

To assess the MWM learning and memory performance, three metrics of learning was retrieved from the platform zone (11 cm in diameter circular area). These were 1) latency to the first entry-, 2) number of entries-, and 3) time spent on the platform zone. In the probe trial the *db/+* exercised mice had the lowest average latency to the first entry to the platform

zone (figure 32A), the highest number of entries- (figure 32B) and spent the most time in the platform zone (figure 32C) compared to the other groups of mice.

As the platform zone was within the peri-platform zone, the data from the platform zone showed the same patterns as those obtained from the peri-platform zone. The data from the platform zone, however, showed more statistically significant differences. The *db/db* sedentary had the longest latency to the first entry to the platform zone, with only one in three mice entering the platform zone at all (hence, the two square points at 60 seconds in figure 32A). Four of the *db/db* exercised mice did not find the platform zone at all (thus the four downward triangles at 60 seconds in (figure 32A) and used a slightly longer time before entering the platform zone than the two *db/+* groups (figure 32A). It was observed a slightly higher average number of entries to the platform zone for the *db/db* exercised mice than for the *db/+* sedentary mice; due to two of the *db/db* mice entering the zone a total of five times (figure 32B). The *db/+* exercised animals tended to have a higher number of entries to the platform zone than the *db/+* sedentary mice ( $p = 0.056$ , Kruskal-Wallis test, Dunn's test, GraphPad Prism) (figure 32B). The Kruskal-Wallis test showed significant differences among the groups from "Time in the Platform zone" ( $p = 0.027$ , Kruskal-Wallis test, GraphPad Prism) where the *db/+* exercised mice spent a significantly higher amount of time in the platform zone than the *db/+* sedentary mice ( $p = 0.020$ , Dunn's test, GraphPad Prism) (figure 32C).

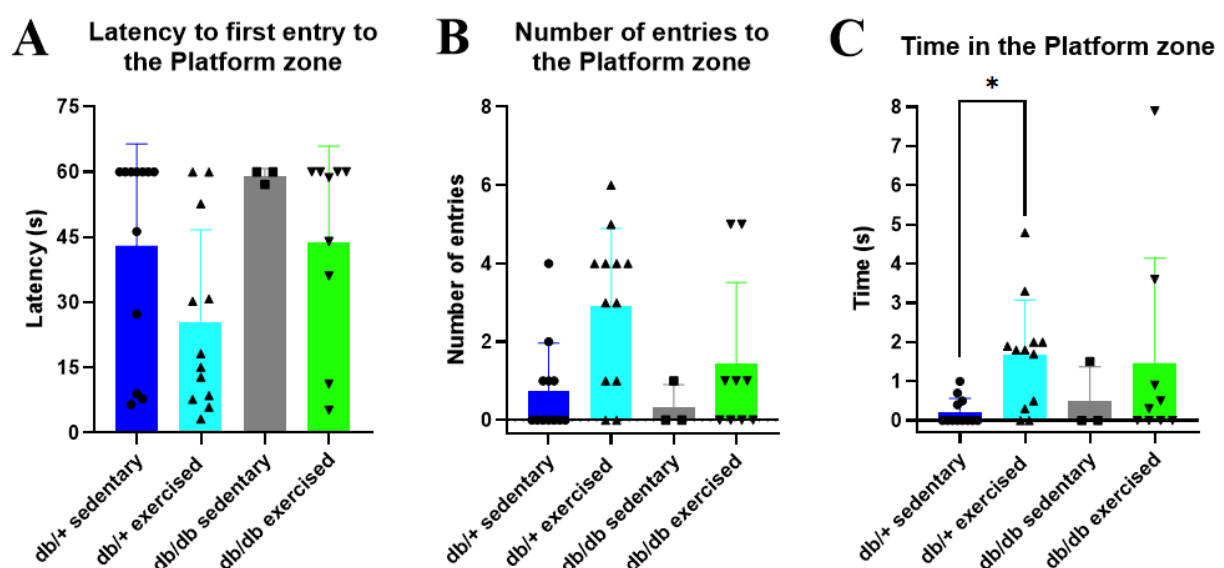


**Figure 32: Average latency to the first entry to the platform zone, number of entries to the platform zone and time in the platform zone during the test day at MWM.**

A) There were no statistically significant differences in the latency to the first entry to the platform zone between

the groups ( $p = 0.101$ , Kruskal-Wallis test, GraphPad Prism). The *db/+* exercised mice (turquoise) had the shortest latency, followed by *db/+* sedentary (blue), *db/db* exercised (green) and *db/db* sedentary (grey), respectively. **B)** The average number of entries to the platform zone were higher for the *db/+* exercised mice than for the *db/+* sedentary mice ( $p = 0.056$ , Dunn's multiple comparisons test, GraphPad Prism). Although there were not significant differences, the *db/+* exercised mice entered the platform zone the most average times compared to the other groups. **C)** The average time in the platform zone ( $p = 0.027$ , Kruskal-Wallis test, GraphPad Prism) was significantly higher for the *db/+* exercised mice than for the *db/+* sedentary mice ( $p = 0.020$ , Dunn's multiple comparisons test, GraphPad Prism). The *db/db* exercised spent a slightly longer average of time in the platform zone compared to the *db/db* sedentary. The bars represent mean  $\pm$  SD; individual values for each mouse are given as black circles, upward triangles, squares, or downward triangles. \*  $p < 0.05$ . Number of animals included: *db/+* sedentary ( $n = 12$ ), *db/+* exercised ( $n = 12$ ), *db/db* sedentary ( $n = 3$ ), *db/db* exercised ( $n = 9$ ).

In total, the test results indicate that the *db/+* exercised mice had the best memory of the platform location compared to the other groups. Between the two obese *db/db* groups it was observed slightly better results in the MWM test for the *db/db* exercised than the sedentary mice, but with no statistical differences.

## 4.7 Microglia activation in sedentary *db/db* and *db/+* mice

Confocal images from 3 *db/+* and 4 *db/db* mice were included in the microglia activation analysis. In each  $134.1\mu\text{m} \times 134.1\mu\text{m} \times 20\mu\text{m}$  image from the hippocampal areas Cornu Ammonis 1 (CA1) and Cornu Ammonis 3 (CA3), microglia were counted, and the average density of microglia per animal (number of microglia divided by the areas of CA1 and CA3, respectively) was calculated. A higher number of microglia cells was observed in the CA1 area in *db/db* mice compared to *db/+* mice (figure 33A). The area of the microglia in the CA1 tended to be higher in the *db/+* than *db/db* mice (figure 33B), suggestive of a more activated phenotype. In the CA3, on the other hand, the average density of microglia in the *db/db* mice did not deviate from the *db/+* mice (figure 33C) and the average area of these microglia was almost the same in both genotypes (figure 33D).

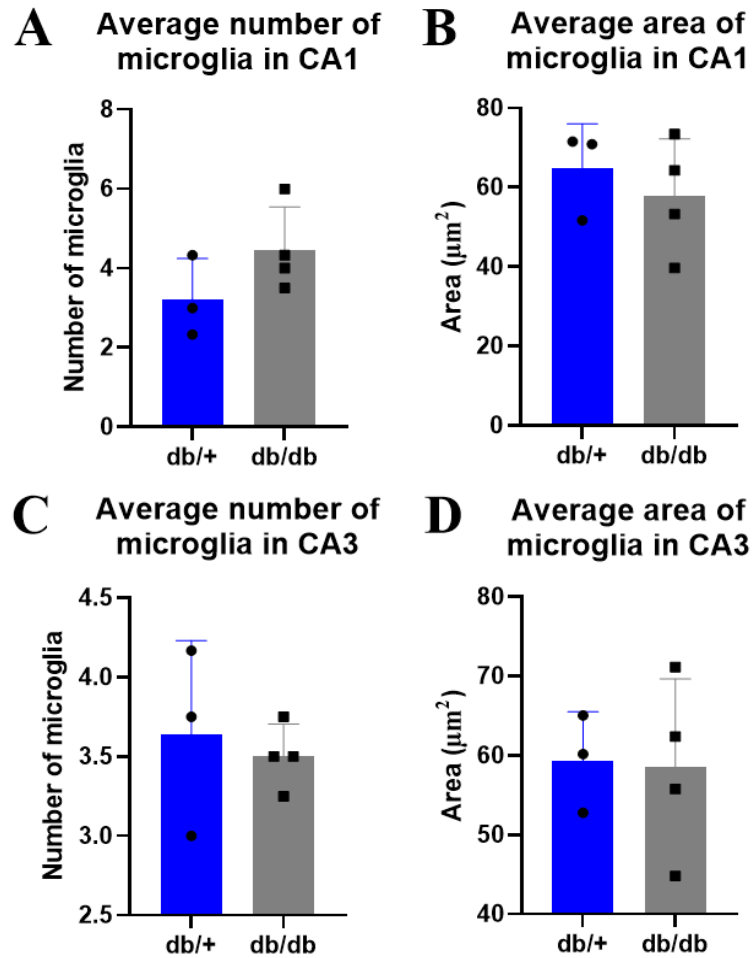


**Figure 33: Density of microglia in the hippocampus and average area of each microglia.**

**A)** The average number of microglia in the CA1 in db/db mice (grey) was observed to be slightly higher than in db/+ mice (blue), but not statistically significant ( $p=0.187$ , unpaired students t-test, GraphPad Prism). **B)** The average area of microglia in the CA1 ( $p=0.520$ , unpaired students t-test, GraphPad Prism). **C)** The average number of microglia in the CA3 ( $p=0.673$ , unpaired students t-test, GraphPad Prism). **D)** The average area of microglia in the CA3 ( $p=0.915$ , unpaired students t-test, GraphPad Prism). The bars represented mean  $\pm$  SD; individual values for each mouse are given as black circles or squares. Number of animals included: db/+ mice ( $n=3$ ), db/db mice ( $n=4$ ).

The skeletonized microglia were analyzed for metrics for microglia activation.

Interestingly, the results indicated a trend towards a lower number of branches ( $p=0.094$ , unpaired students t-test, GraphPad Prism), junctions ( $p=0.095$ , unpaired students t-test, GraphPad Prism) and end-point voxels ( $p=0.093$ , unpaired students t-test, GraphPad Prism) on the microglia cells in the CA1 in db/db mice compared to the db/+ mice (figure 34A-C).

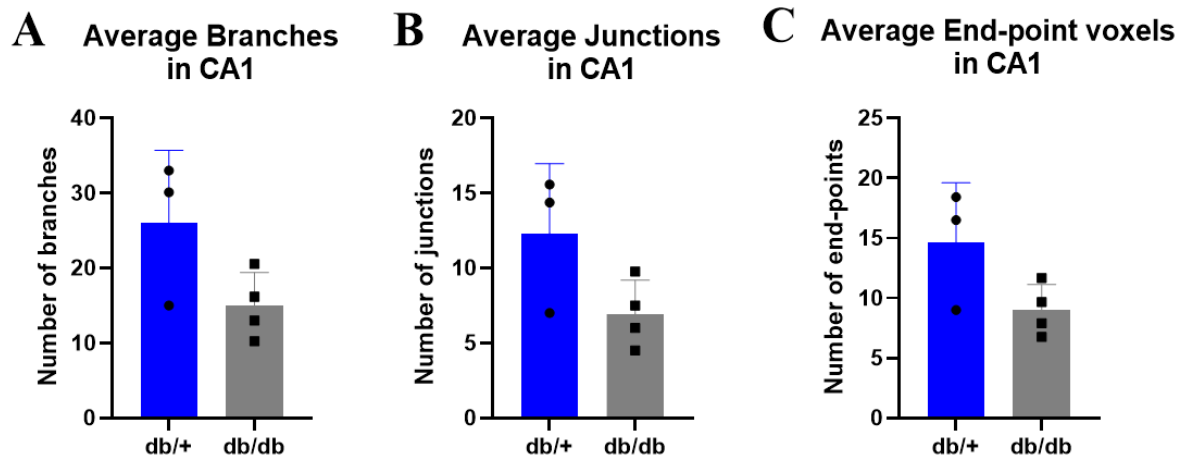


**Figure 34: Microglia activation in the hippocampal CA1 area.**

All three measures of microglia activation tended to be more pronounced in the *db/db* mice (grey) than in the *db/+* mice (blue). **A)** The average number of branches ( $p=0.094$ , unpaired students *t*-test, GraphPad Prism). **B)** the average number of junctions ( $p=0.095$ , unpaired students *t*-test, GraphPad Prism). **C)** The average number of end-point voxels ( $p=0.093$ , unpaired students *t*-test, GraphPad Prism). The bars represent mean  $\pm$  SD; individual values for each mouse are given as black circles or squares. Number of animals included: *db/+* mice ( $n=3$ ), *db/db* mice ( $n=4$ ).

Microglia activation in the CA3 showed the same pattern as what was observed in the CA1 region, but the tendency towards a difference between the genotypes was farther from being statistically significant. The microglia in the CA3 of *db/db* mice trended towards lower average number of branches ( $p=0.629$ , Mann-Whitney U test, GraphPad Prism), junctions ( $p=0.335$ , unpaired students *t*-test, GraphPad Prism) and end-points ( $p=0.629$ , Mann-Whitney U test, GraphPad Prism) compared to the *db/+* mice (figure 35A-C).

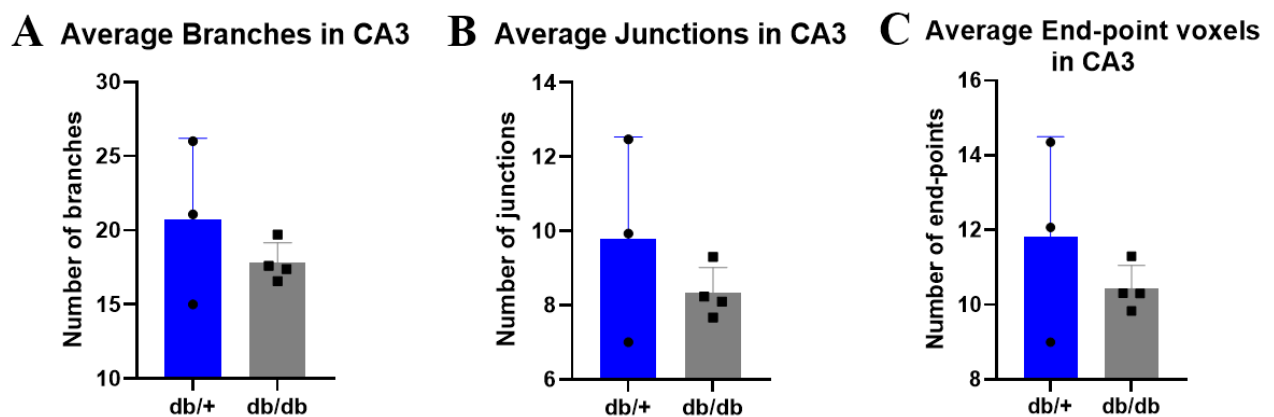


**Figure 35: Microglia activation in the hippocampal CA3 area.**

All three measures of microglia activation tended to be more pronounced in the *db/db* mice (grey) than in the *db/+* mice (blue). **A)** The average number of branches ( $p=0.629$ , Mann-Whitney U test, GraphPad Prism). **B)** The average number of junctions ( $p=0.335$ , unpaired students *t*-test, GraphPad Prism). **C)** The average number of end-point voxels ( $p=0.629$ , Mann-Whitney U test, GraphPad Prism). The bars represent mean  $\pm$  SD; individual values for each mouse are given as black circles or squares. Number of animals included: *db/+* mice ( $n=3$ ), *db/db* mice ( $n=4$ ).



## 4.8 Microglia activation in 5xFAD and wild type mice

Confocal images from 9 transgenic (tg) 5xFAD and 8 wt mice were included in the microglia activation analysis. The 5xFAD mice had a significantly higher average number of microglia in the CA1 area than the wt mice (Figure 36A;  $p=0.013$ , unpaired students t-test, GraphPad Prism). The same effect was seen in the CA3 area (Figure 36C;  $p=0.002$ , Mann-Whitney U test, GraphPad Prism). There were no significant differences in the average area of the microglia in the CA1 area (Figure 36B;  $p=0.384$ , unpaired students t-test, GraphPad Prism) or CA3 area (Figure 36D;  $p=0.383$ , unpaired students t-test, GraphPad Prism).

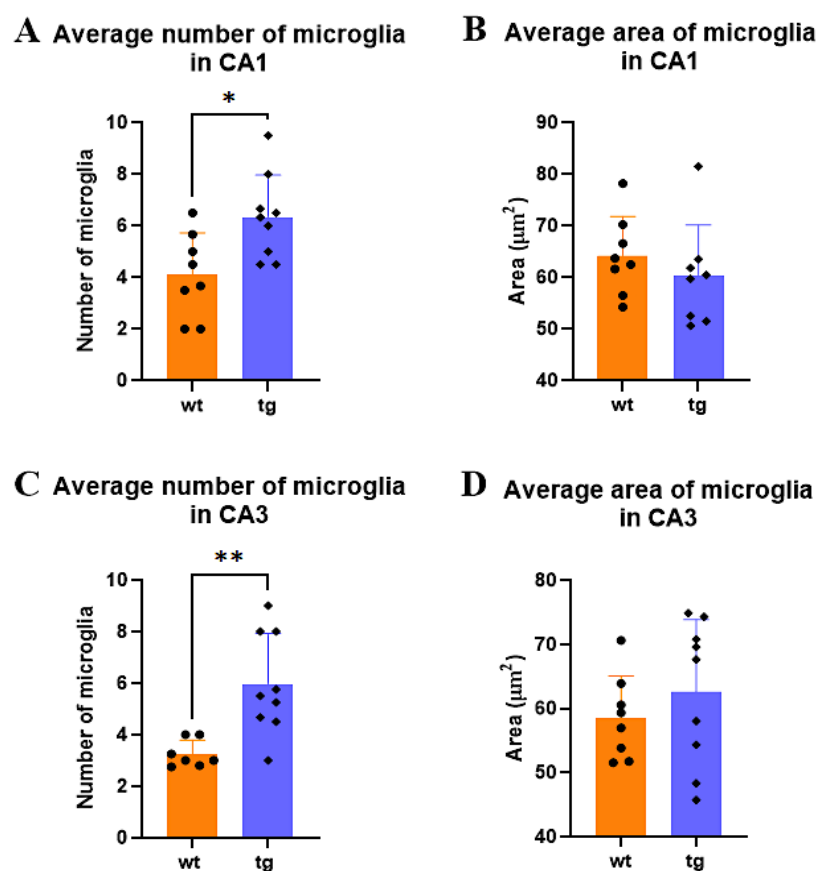


**Figure 36: Density of microglia in the hippocampus and average area of each microglia.**

The density of microglia (number of cells/hippocampal area) and the area covered by each microglia was analyzed in 5xFAD (tg) mice (purple) and wt mice (orange). **A**) The average density of microglia in the CA1 was significantly higher in tg mice than wt mice ( $p=0.013$ , unpaired students t-test, GraphPad Prism). **B**) The average area of each microglia in the CA1 was not different between the genotypes ( $p=0.384$ , unpaired students t-test, GraphPad Prism). **C**) The density of microglia in the CA3 was significantly higher in tg than wt mice ( $p=0.002$ , Mann-Whitney U test, GraphPad Prism). **D**) The average area of each microglia in CA3 did not differ between tg and wt mice ( $p=0.383$ , unpaired students t-test, GraphPad Prism). The bars represent mean ± SD; individual values for each mouse are given as black circles or diamonds. \*  $p < 0.05$ . Outliers removed: **B** (tg;  $n=1$ ). Number of animals included: **A, C, D** (wt;  $n=8$ , tg;  $n=9$ ), **B** (wt;  $n=8$ , tg;  $n=8$ ).

When measuring the number of branches, junctions and end point voxels for each microglia of the CA1 area, we found that the tg animals had a significantly lower average number of branches (figure 37A;  $p=0.013$ , unpaired students t-test, GraphPad Prism), junctions (figure 37B;  $p=0.015$ , unpaired students t-test, GraphPad Prism) and end-points (figure 37C;  $p=0.012$ , unpaired students t-test, GraphPad Prism) compared to the wt mice. A reduction in any of these parameters are regarded as signs of enhanced microglia activation.

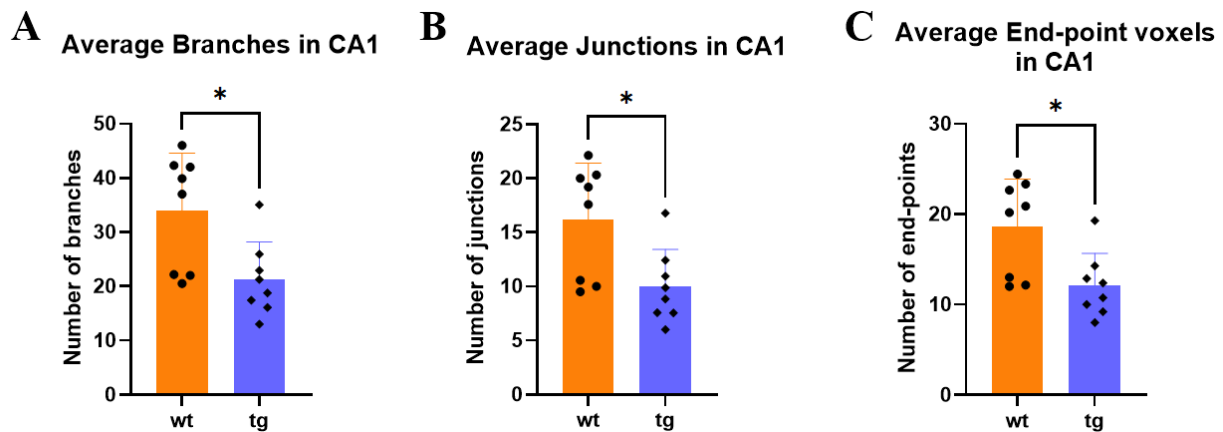


**Figure 37: Microglia activation in the hippocampal CA1 area.**

All three measures of microglia activation were more pronounced in the 5xFAD (tg) mice (purple) than in the wt mice (orange). **A**) The average number of branches was reduced in the tg mice compared to the wt controls ( $p=0.013$ , unpaired students t-test, GraphPad Prism). **B**) The average number of junctions was lower in the tg mice than in the wt controls ( $p=0.015$ , unpaired students t-test, GraphPad Prism). **C**) The average number of end-point voxels was reduced in the tg mice compared to the wt control ( $p=0.012$ , unpaired students t-test, GraphPad Prism). The bars represent mean  $\pm$  SD; individual values for each mouse are given as black circles or diamonds. \*  $p < 0.05$ . Outliers removed: **A, B, C** (tg;  $n=1$ ). Number of animals included: (wt;  $n=8$ , tg;  $n=8$ ).

In the CA3 area of hippocampus there were no statistically differences in the average number of branches ( $p=0.170$ , unpaired students t-test, GraphPad Prism), junctions ( $p=0.214$ , unpaired students t-test, GraphPad Prism) or end-points ( $p=0.164$ , unpaired students t-test, GraphPad Prism). However, the tg mice tended to have lower average number of branches, junctions and end-point voxels compared to the wt (figure 38A-C).

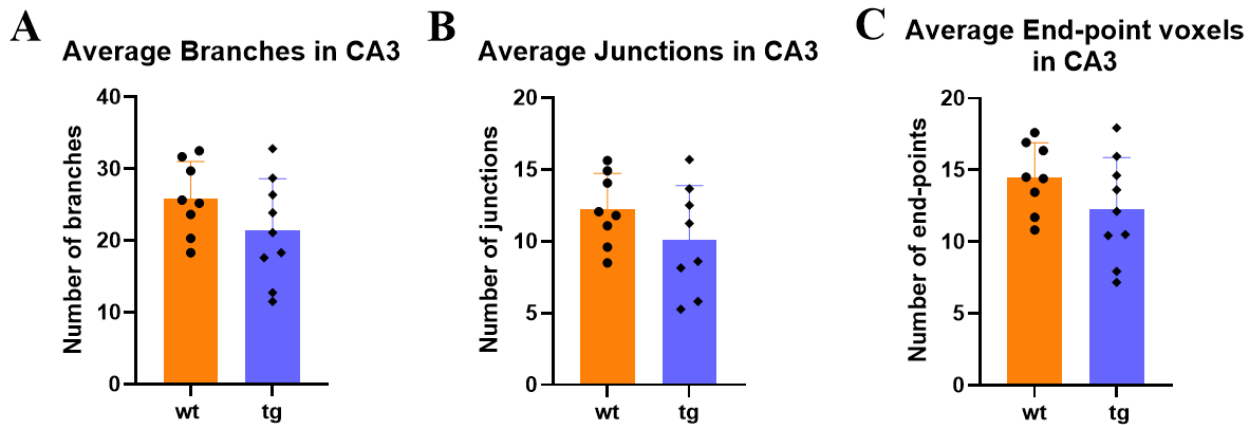


**Figure 38: Microglia activation in the hippocampal CA3.**

There were no statistically significant differences in the three measures of microglia activation between the 5xFAD (tg) mice (purple) and the wt mice (orange), but all measures tended to be lower in the tg mice. **A)** The average number of branches ( $p = 0.170$ , unpaired students t-test, GraphPad Prism). **B)** The average number of junctions ( $p = 0.214$ , unpaired students t-test, GraphPad Prism). **C)** The average number of end-point voxels ( $p = 0.164$ , unpaired students t-test, GraphPad Prism). The bars represent mean  $\pm$  SD; individual values for each mouse are given as black circles or diamonds. Outliers removed: **B** (tg;  $n = 1$ ). Number of animals included: **A, C** (wt;  $n = 8$ , tg;  $n = 9$ ), **B** (wt;  $n = 8$ , tg;  $n = 8$ ).

#### 4.8.1 Microglia activation and lipid droplets in exercised and sedentary *db/db* and *db/+* mice

To investigate whether high-intensity interval exercise affects microglia activation or LD dynamics in the brain, the *db/db* and *db/+* mice exposed to 8 weeks of exercise intervention were also immunolabeled. Despite several attempts, the antibody against Iba1 labeled the astrocytes in addition to microglia. Due to the limited time frame for this master project, these mice were not analyzed for microglia activation and LD.

An example of the immunohistochemistry labeling with antibodies for Iba1 and GFAP and BODIPY, where some processes are labeled both white and red, is shown in figure 39. With Iba1 labeling the astrocytes in addition to the microglia, the Iba1+ and DAPI+ microglia could not be separated, hence would give an incorrect microglia activation analysis.

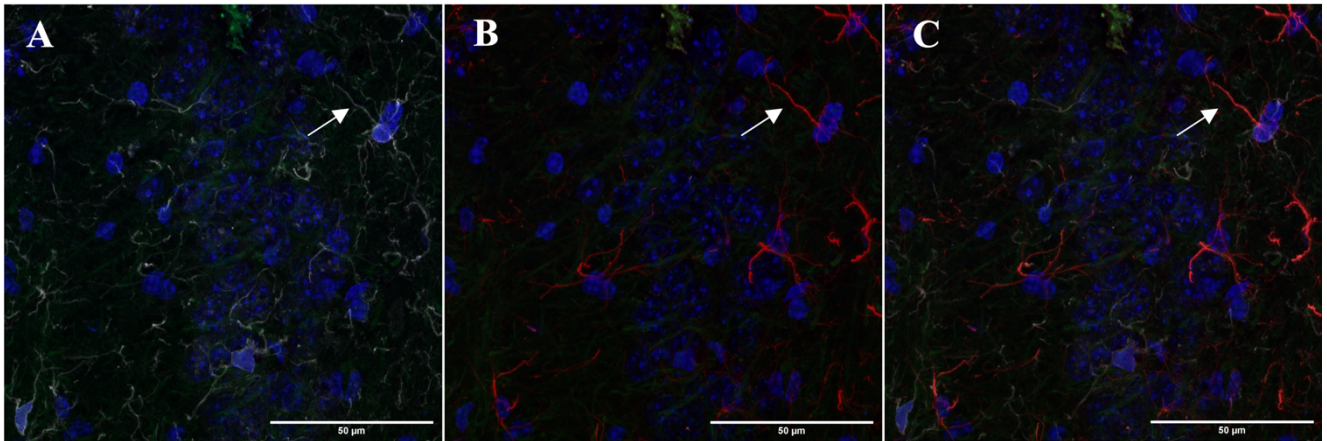


**Figure 39: Confocal images showing Iba1 overlay.**

**A)** Confocal image of Iba1 (white), DAPI (blue) and BODIPY (green). **B)** Confocal image of GFAP (red), DAPI (blue) and BODIPY (green). **C)** Confocal image of Iba1, GFAP, DAPI and BODIPY. The fragments labelled by GFAP are also labelled by Iba1 as illustrated with arrow, indicating an Iba1 overlay. Scale bar = 50  $\mu\text{m}$

## 4.9 Lipid droplets within microglia in *db/db* and *db/+* sedentary mice

After the microglia segmentation, the same images were analyzed for LD. There were no significant differences in the average number- or area of LD in microglia in the CA1 of *db/+* and *db/db* mice (figure 40).

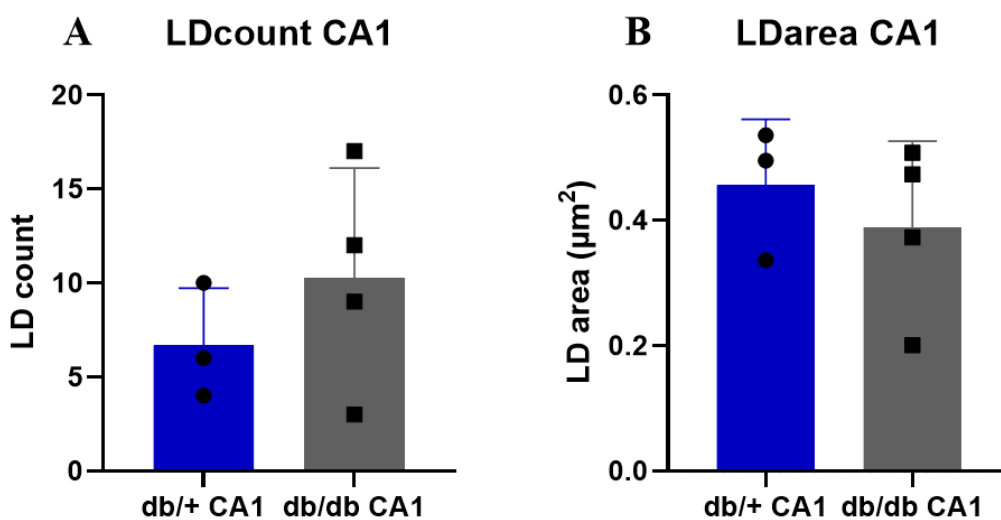


**Figure 40: Density of lipid droplets and average area of lipid droplets in microglia in the hippocampal CA1.** The density of lipid droplets (number of lipid droplets/microglia) and the area covered by each lipid droplet was analyzed in *db/+* (blue) and *db/db* (grey) mice. **A)** The average number of lipid droplets in microglia in the CA1

did not differ between sedentary *db/+* and *db/db* mice ( $p = 0.6286$ , Mann Whitney test, GraphPad Prism). **B**) The average area of the lipid droplets in microglia in the CA1 also did not differ between the genotypes ( $p = 0.6286$ , Mann Whitney test, GraphPad Prism). The bars represent mean  $\pm$  SD; individual values for each mouse are given as black circles or squares. Number of animals included: (*db/+*;  $n = 3$ , *db/db*;  $n = 4$ ).

The average number of LD in microglia in the CA3 of the *db/+* and *db/db* mice did not deviate between the genotypes ( $p = 0.6286$ , Mann Whitney test, GraphPad Prism). There was, however, a tendency towards a higher area of the LD in the CA3 of *db/db* mice compared to in microglia of *db/+* mice ( $p = 0.1143$ , Mann Whitney test, GraphPad Prism) (figure 41).

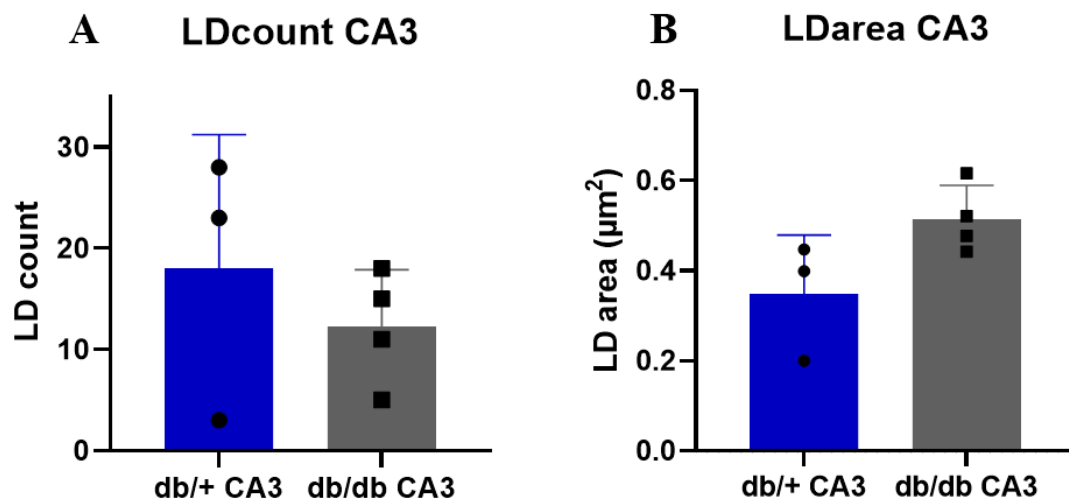


**Figure 41: Density of lipid droplets in microglia and average area of lipid droplets in the hippocampal CA3.** The density of lipid droplets (number of lipid droplets/microglia) and the area covered by each lipid droplet was analyzed in *db/+* (blue) and *db/db* (grey) mice. **A**) The average number of lipid droplets in microglia in the CA3 was not different between the genotypes ( $p = 0.6286$ , Mann Whitney test, GraphPad Prism). **B**) The average area of the lipid droplets in microglia in the CA3 tended to be higher in the *db/db* mice than in the *db/+* littermates ( $p = 0.1143$ , Mann Whitney test, GraphPad Prism). The bars represent mean  $\pm$  SD; individual values for each mouse are given as black circles or squares. Number of animals included: (*db/+*;  $n = 3$ , *db/db*;  $n = 4$ ).

A correlation test was also performed to investigate if there was any correlation between LDs and microglia activation in each microglia cell. A decreased number of junctions was used as a measure of microglia activation and we analyzed whether this correlated with a higher number of LDs in that same cell, or with the area covered by LD in the respective cell. The test found a significant positive correlation ( $r = 0.3784$ ) between a higher number of junctions and number of LDs in microglia in the CA3 of *db/+* mice ( $p = 0.0175$ , Spearman test, GraphPad Prism) (figure 42C). LD number or LD area in the CA1 as well as LD area in the CA3 did not correlate with number of microglia junctions (figure 42A,B,D). One thing to note is that outliers were not removed in this test.

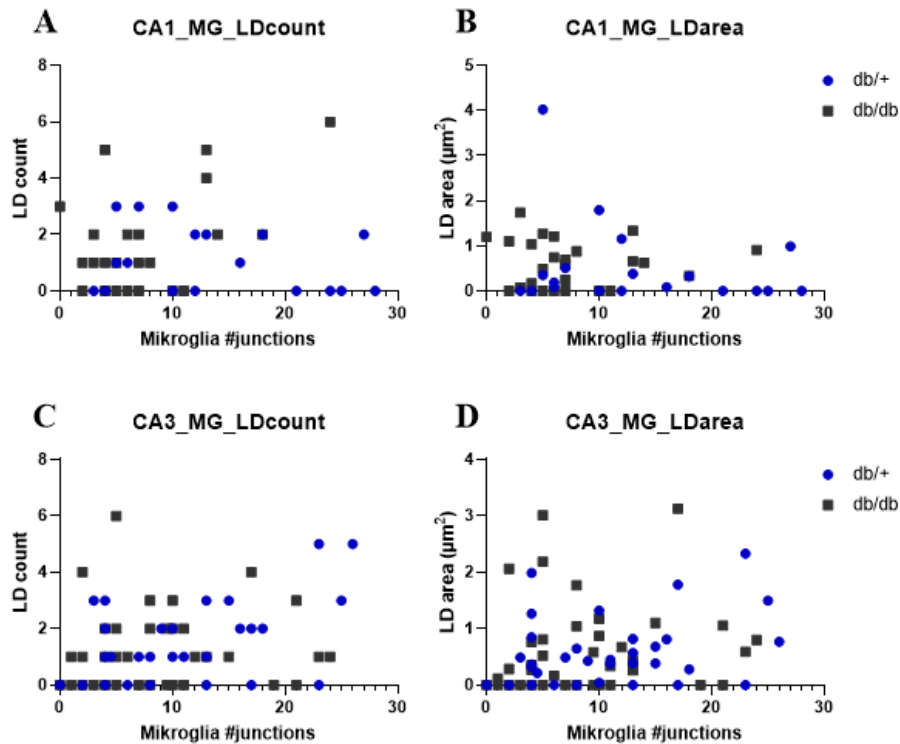


**Figure 42: Correlation between number of junctions in the microglia and number of- and area covered by lipid droplets in the individual microglial cells of the hippocampal CA1 and CA3 regions.**

Lipid droplet number and area are given for each individual cell for *db/+* (blue circles) and *db/db* (grey squares) and plotted gains each other to find if any correlation exists between the degree of microglia activation and the accumulation of lipid droplets. **A)** The number of lipid droplets did not correlate with the number of junctions on the microglia in CA1 of neither *db/+* ( $r = -0.1450$ ) nor *db/db* ( $r = 0.2181$ ). **B)** The area of the lipid droplet did not correlate with the number of junctions on the microglia in CA1 of neither *db/+* ( $r = -0.1658$ ) nor *db/db* ( $r = -0.0283$ ). **C)** The number of lipid droplets and number of junctions on the microglia in CA3 also did not correlate, neither of *db/+* ( $r = 0.3784$ ) nor *db/db* ( $r = 0.2382$ ). There was a significant positive correlation between number of junctions and number of lipid droplets in *db/+* mice ( $p = 0.0175$ ). **D)** The area of the lipid droplet did not correlate with the number of junctions on the microglia in CA3 of neither *db/+* ( $r = 0.3006$ ) nor *db/db* ( $r = 0.2958$ ). A non-parametric Spearman correlation test was used for all these data.

## 4.10 Lipid droplets within microglia of 5xFAD and wild type mice

LD number and area were also analyzed in the 5xFAD and wild type mice. There were no significant differences in the average number ( $p = 0.8747$ , unpaired students t-test, GraphPad Prism) or area ( $p = 0.9735$ , unpaired students t-test, GraphPad Prism) of LD in microglia in the CA1 of *wt* and *5xFAD* mice (figure 43).

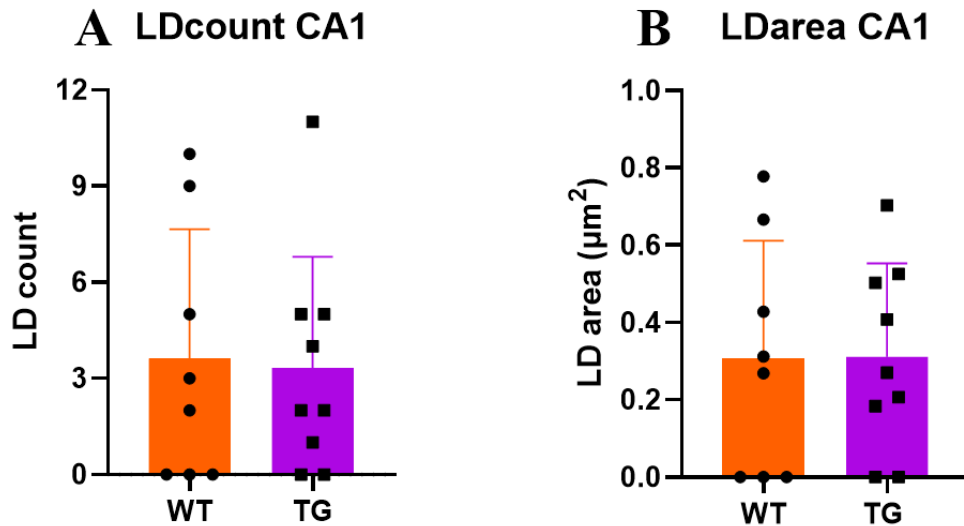


**Figure 43: Density of lipid droplets in microglia and average area of lipid droplets in each microglia of the hippocampal CA1.**

The density of lipid droplets (number of lipid droplets/microglia) and the area covered by each lipid droplet was analyzed in wt (orange) and tg 5xFAD (purple) mice. **A)** The average number of lipid droplets in microglia of the CA1 did not differ between the 5xFAD mice and the control mice ( $p = 0.8747$ , unpaired students t-test, GraphPad Prism). **B)** The average area of the lipid droplets in microglia of the CA1 also did not differ between the genotypes ( $p = 0.9735$ , unpaired students t-test, GraphPad Prism). The bars represent mean  $\pm$  SD; individual values for each mouse are given as black circles or squares. Number of animals included: (wt;  $n = 8$ , tg;  $n = 9$ ).

There were no differences in number of LD in the CA3 between the 5xFAD and wt mice ( $p = 0.5455$ , Mann Whitney U test, GraphPad Prism) (figure 44A). Interestingly, the area of the LD in microglia in the CA3 were significantly lower in the 5xFAD mice compared to the wt mice ( $p = 0.0234$ , unpaired students t-test, GraphPad Prism) (figure 44B).

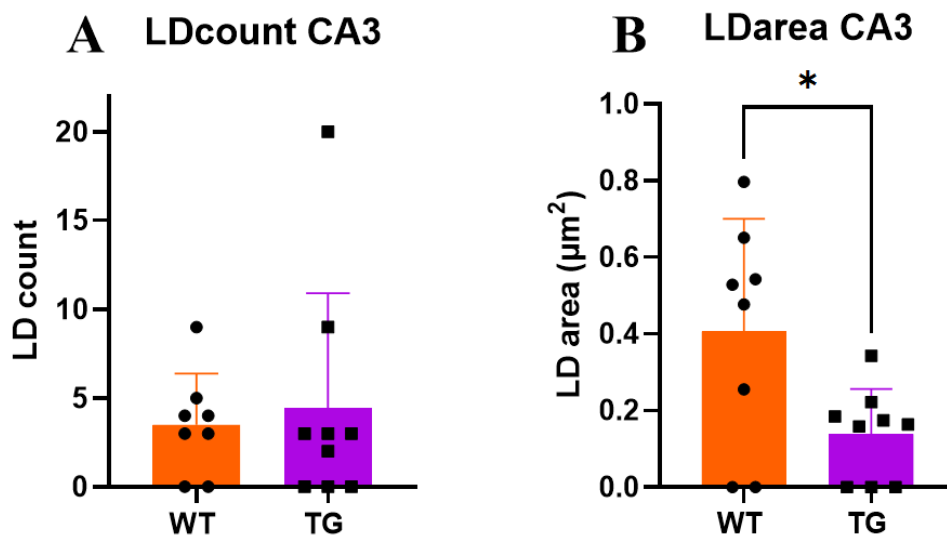


**Figure 44: Density of lipid droplets and the average area of lipid droplets in microglia of the hippocampal CA3 region.**

The density of lipid droplets (number of lipid droplets/microglia) and the area covered by each lipid droplet was analyzed in wt (orange) and tg 5xFAD (purple) mice. **A)** The average number of lipid droplets in microglia in the CA3 was not changes in the 5xFAD mice compare do the wt controls ( $p=0.5455$ , Mann Whitney U test, GraphPad Prism). **B)** The average area of the lipid droplets in microglia in the CA3, however, was lower in the 5xFAD mice (tg) than in the wt mice ( $p=0.0234$ , unpaired students t-test, GraphPad Prism). The bars represent mean  $\pm$  SD; individual values for each mouse are given as black circles or squares. Number of animals included: (wt;  $n=8$ , tg;  $n=9$ ).

In line with what was found for the *db/db* and *db/+* mice, a correlation test showed no significant correlations between LD and the number of microglia junctions in each of the microglia cells in the 5xFAD mice or the wt littermates, neither in the CA1 nor CA3 (figure 45).

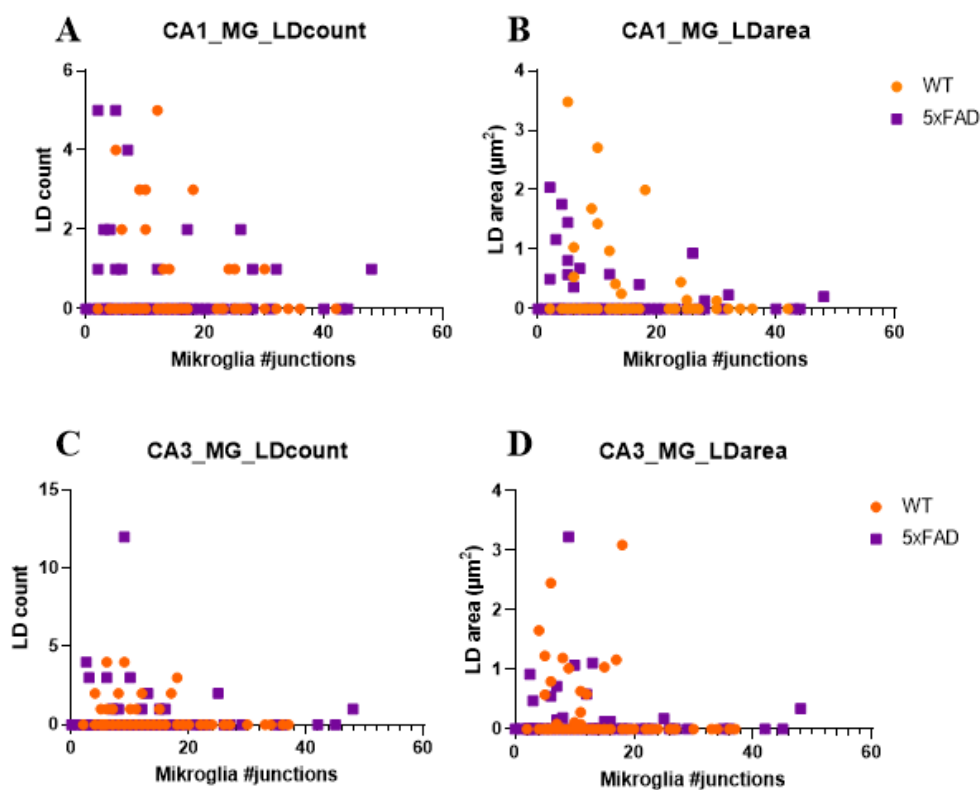


**Figure 45: Correlation between number of junctions in the microglia and number of or area covered by lipid droplets in the hippocampal CA1 and CA3.**

Lipid droplet number and area are given for each individual cell for wt (orange circles) and tg 5xFAD mice (purple squares) to find if any correlation existed betweenin the degree of microglia activation and lipid droplets. **A)** The number of lipid droplets did not correlate with the number of junctions on the microglia in CA1 for neither wt ( $r=-0.1386$ ) nor 5xFAD ( $r=-0.0303$ ). **B)** The area of the lipid droplet did not correlate sith the number of junctions on the microglia in CA1 for neither wt ( $r=-0.1423$ ) nor 5xFAD ( $r=-0.0442$ ). **C)** The number of lipid dropletsdid not correlate with the number of junctions on the oglia in CA3 for neither wt ( $r=-0.1619$ ) nor 5xFAD ( $r=0.0529$ ). **D)** The area covered by lipid droplet did not correlate with the number of junctions on the microglia in CA3 for neither wt ( $r=-0.1675$ ) nor 5xFAD ( $r=0.0555$ ). A non-parametric Spearman correlation test was used on all data.



# 5 Discussion

## 5.1 Methodological considerations

### 5.1.1 Animals

Alzheimer disease (AD) and type 2 diabetes mellitus (T2DM) can be studied with both *in vivo* and *in vitro* models. In this study we wanted to investigate any phenotypical changes in the brain after high-exercise intervals, and the pathophysiological mechanisms that link diabetes to dementia. Because of the advanced brain physiology and the complex interaction between the CNS and the periphery, this study was only possible using animal models. Both mouse and humans are mammals, and share genetic, anatomical and physiological similarities (Rosenthal & Brown, 2007). For this reason, mice are often used to model human physiology and diseases creating comparable results between humans and mice in research. Mice have short breeding periods, large litter sizes, as well as a short lifetime compared to many other species (Quesenberry & Donnelly, 2020) and are easy to handle (Clarke, 2002). This is beneficial as it gives the opportunity to study changes within a short period of time, and also to study chronic diseases, such as T2DM and AD, over a large fraction of their lifetime. Mice have been used in research for a long time, hence there is a lot of knowledge about mouse as an animal model in experiments. This includes extensive experiences with suitable behavior tests as well as normal neuroanatomical changes associated with disease. This makes it easier to compare and combine findings from different research groups, and hence interpreting our own data in the context of other studies on similar models. We aimed at studying microglia activation and the accumulation of LD in brain cells by immunohistochemistry. These techniques require brain sections, and hence our study could not be conducted in humans.

In the present study, we performed behavioral tests, including memory tests. Such tests could in theory have been conducted in humans, but this would not allow for linking the behavioral outcomes with mechanistical data. Behavioral tests depend on similar conditions throughout the test period to ensure that all test animals are exposed to equal circumstances and are not affected by changes in lifestyle or environment. The use of mice in behavioral experiments gives the opportunity to control everything happening with the animals during the entire intervention, providing good experimental control. The use of humans in the same behavior

tests over a certain time does not provide the same control, and the operators cannot be sure of what the individuals are exposed to in society. In addition, there are various genetic and physical differences between individuals that make it difficult to conclude what possible differences are due. Hence, a large group of people would have been needed to obtain results of a comparable certainty. The tests used in the present study are well-validated for mice, and the interpretation of the results have also been validated. Mice therefore was a suitable animal model for our study. The mouse genome can be easily manipulated, giving the possibility for mutations, deletions or insertions in the DNA to create precise disease models. The two mouse models used in the present study are genetic models, and their suitability and relevance for the human disease will be discussed in the next paragraphs.

**The 5xFAD animal model:** Mice do not develop AD, naturally, and do not show amyloid plaques even at old age. The mouse orthologue of A $\beta$  has a lower probability to form amyloid plaques than the human form, and hence the human APP gene –often with known human mutations– is inserted into the genome of the mice to generate relevant models. Often these genes are also over-expressed. The fact that the human orthologue is used, may serve as an argument for a high relevance for the human disease, but one may also argue that expressing a human protein variant in a mouse brain may in itself cause dyshomeostasis. These concerns, however, apply to all genetic AD models and not only to the 5xFAD model used in the present study. The 5xFAD model is a transgenic animal model with five AD-linked mutations, creating a severe Alzheimer’s model with an early developed AD pathology; for instance, A $\beta$  plaques and gliosis are observed around 2 months of age (Oakley et al., 2006). This has financial benefits and is an advantage when studying severe AD. On the other hand, the accumulation of A $\beta$  plaque in humans develops with age, and can build up for as much as 20 years before any symptoms of AD occurs (Bateman et al., 2012). This differs from the early progression in the mouse model and may raise the question of whether the pathology in the 5xFAD model is comparable with human AD pathology. Furthermore, in the human brain A $\beta$  pathology develops alongside other AD hallmarks, and these probably mutually affect each other. Amyloid may be a driver of the disease, but recent data from both basic research and human trials –for instance with anti-amyloid antibodies– have suggest that A $\beta$  pathology does not drive the disease alone. Other Alzheimer models with slower developing pathology and where AD is induced not only through manipulation with A $\beta$  also exist, such as the 3xTg-AD (The Jackson Laboratory, 2021a). This is a widely used animal model with three

mutations for AD: one mutation in the gene encoding APP and one in the gene encoding PS1 (as in 5xFAD mice), in addition to a mutation in microtubule-associated protein tau (MAPT) causing tau pathology. The 3xTg-AD mice develop A $\beta$  deposits at 6 months of age and hyperphosphorylated tau pathology at 12-15 months of age (Oddo et al., 2003). The pathology in 3xTg-AD is therefore perhaps more similar to the one seen in humans and has a later but broader disease pathology than 5xFAD mice, although the development of neuronal loss in the 3xTg-AD model is unknown (Oddo et al., 2003). In 5xFAD mice, the mutations are located in the genes encoding human APP and PS1 causing FAD with A $\beta$  plaques, neurodegeneration and cognitive impairments, the same mechanisms occurring in humans with early-onset AD. The total of five mutations simply gives a more progressive disease pathology, which in our case is an advantage as we want to examine the presence of LD in well-developed disease pathology.

**The *db/db* model:** An obese phenotype was necessary to investigate the effects of over-eating and obesity itself on LD density and morphology, as well as the effects of high-interval exercise in the brain of obese mice. In this study, the *db/db* mice model was used. A mutation in the *Lepr* gene causes these mice to eat excessively, resulting in obesity and consequentially leading to the development of T2DM. The *db/db* mice is a severe diabetic model where the mice show elevated insulin levels already at 10-14 days after birth. They also have elevated blood sugar after 4-8 weeks, and an obese phenotype at 3-4 weeks of age (The Jackson Laboratory, 2021b). This makes it possible to investigate behavioral- and cerebral changes due to high-intensity exercise in a model with a fully developed phenotype within a short amount of time. In the present study, the mice started the exercise intervention at 9-11 weeks of age, which is translated to young adult human age. At this age, the *db/db* mice had developed obesity and T2DM (Hagan, 2017). Such a rapidly developing model may be a disadvantage when studying the effects of antidiabetic treatments but is good for studying the consequences of the severe phenotype. The model also allows for discrimination between the effects of exercise on brain function *per se* and the indirect effects mediated through a reduction in T2DM pathology; the mice did not lose weight, nor did they change their body composition in response to exercise. One factor that severely affected the current master project is the fact that the model has limitations when it comes to breeding. Homozygote *db/db* are infertile, and therefore heterozygote *db/+* mice were used in breeding. According to the information given on the Jackson Laboratory homepage “*This strain is a good breeder. When maintaining a live colony, these mice are bred as heterozygotes. Females homozygous*

*for the mutation are infertile and males exhibit a reduced ability to mate*". Nevertheless, in our hands, the mice had small litters and the number of *db/db* mice in the litters did not follow a Mendelian distribution. The percentage of *db/db* mice was lower than expected most likely as a result of incomplete embryo development for this genotype. When confronting the Jackson Laboratory about this, we received the information that *«In general the Het x Het colonies don't produce as many homozygotes as the Punnett square would indicate (...)»*. The low breeding efficiency of the strain forced us to conduct the experiments repeatedly with smaller groups of animals in order to keep the animals at a comparable age. The latter is especially important when studying the fast-progressing 5xFAD model. The consequence of this is that experiments became more time-consuming and that we ended up with fewer animals in some of the groups, which may have affected the statistical results of our study (see below).

### **5.1.2 Exercise regime**

The high-intensity interval exercise regime has previously been used in research on mice and with beneficial results, such as improved glycaemic control and angiogenesis (Morland et al., 2017; Wisløff, Ellingsen, & Kemi, 2009). High-intensity interval training has also been used for *db/db* mice, and shown to cause decreased fasting plasma glucose and improved glycaemic control (Chavanelle et al., 2017), as well as alterations in mitochondrial morphology and function (Bækkerud et al., 2019). Alternative exercise regimes, such as moderate intensity continuous training can be used. However, a study conducted by Chavanelle et al. compared high-intensity interval training with moderate intensity continuous training in *db/db* mice and observed significantly lower fasting glycaemia with the high-intensity exercise regimen (Chavanelle et al., 2017). This underpins our choice of exercise regime for the mice in this study.

The mice ran on a treadmill where the running speed was decided based on their recent performance in a MECT test. When not keeping up with the pace, the animals were pushed gently back on the band. Although the animals were evaluated from day to day, and given additional breaks if needed, the exercise regime used in the present study is a form of forced running. This may cause stress for the animals. Stress can cause different physiological processes, affecting the study outcome. In the literature, it is shown that corticosterone levels, a major stress hormone, were higher in the urine of *db/db* mice after treadmill exercised

compared to voluntary exercised (running wheel) (Parrott, Ghosh, Tedeschi, Gunasekara, & Broderick, 2011). The same study found that the treadmill running impaired the metabolic control in the *db/db* mice, indicating that stress induced by a forced running method contributes to change in physiological and pathological mechanisms. Voluntary running, however, produced more variation in the exercise regime, as some mice prefer to run more, both in terms of the distance and the running speed, than others. This can be measured and accounted for, but in voluntary running, this cannot be avoided. In our study the mice had to run at 80 % of their maximum capacity, which can only be ensured by a forced running protocol. During our study, the operators observed the mice closely for any sign of stress, and if deviant behavior was observed the mouse was given a break from the exercise.

Occasionally, an assessment was made of whether the mouse should be in its cage for the rest of the training session. Only one *db/+* mouse had its training session cancelled for one day, all the mice quickly got used to the running routines and the exercise regime. An advantage in using treadmill running is that the operators at all time have control over the running speed and can easier observe whether or not the mice run at 80 % of their maximum capacity.

During the 8 weeks of intervention there were also sedentary control groups, only staying in their cages. To ensure the greatest possible similarities between the groups, for example that no one was more active than others and would influence the result, running wheels were not preserved in the animal cages.

**Maximal exercise capacity test (MECT):** During the MECT, the animals ran until exhaustion where the operators decided the time point of exhaustion based on signs such as jumping with their hind legs and leaning against operators hand when pushed. The test could not be blinded because of phenotype, which could lead to the operators being subconsciously influenced by the phenotype of the mice. This is a limitation to the MECT, as the operator may conclude that a mouse is reaching exhaustion based on the expectation that the *db/db* mice have less endurance than the lean *db/+* mice. To preserve any physiological changes in the brain caused by exercise, the mice were euthanatized on the same day as the last exercise session, at 5.5-6.5 hours after the last exercise session.

### **5.1.3 Perfusion fixation**

**Anesthesia:** Perfusion fixation took place in anaesthetized animals. This step requires careful calculations and monitoring, as the animal must be in a deeply anaesthetized state yet

maintaining adequate respiration. A too mild stage of anesthesia may cause pain and stress to the animal. It is not ethically correct to inflict unnecessary pain on the animal, as in addition this may affect the physiology (Chu, Marwaha, Sanvictores, & Ayers, 2021) of the mouse. A too deep a stage of anesthesia can provide CNS depression and death. Therefore, the animals were monitored and checked with a toe pinch test to ensure the correct depth of anesthesia before starting the perfusion fixation procedure. If the mouse reacted when pressing hard between its toes, the anesthesia depth was not sufficient.

**Perfusion fixation:** Because we study cellular and subcellular structures in the brain, the cytoarchitecture in the tissue must be kept intact throughout the entire brain. A critical step is therefore the fixation. Without an evenly distributed fixative throughout the brain, the cell structures may not be preserved, and remaining blood cells may interfere with antibodies at the IHC. We chose the perfusion fixation method to ensure even fixation through the entire brain by using the animal's circulation to distribute the fixative. This is important when studying larger tissue samples, like intact brain, and to a large degree prevents artefacts due to the fixative reaching different brain regions at different rates (Gage, Kipke, & Shain, 2012; Kasukurthi et al., 2009). In our experiments, the fixative was pumped into the heart at a rate and pressure that resembled what is normally occurring in mice. This is essential to avoid artefacts induced by for instance swelling. Formaldehyde was the chosen fixative as it has been used as a fixative for over a century and has high adaptability (Howat & Wilson, 2014; Thavarajah, Mudimbaimannar, Elizabeth, Rao, & Ranganathan, 2012). Compared to other commonly used fixatives, formaldehyde has a high rate of penetration into the tissue, resulting in less hypoxia/ischemia and degradation processes. Compared to for instance glutaraldehyde, formaldehyde better preserves the antigenicity, slightly at the cost of lower preservation of the morphology. In our study, we the ability to properly stain with antibodies as was considered more important than keeping the morphology optimal. Glutaraldehyde also produced more autofluorescence, which is not compatible with our studies. Formaldehyde does preserve morphology well enough for most studies at light- or fluorescent microscopy. A disadvantage of formaldehyde, is that it can precipitate (Kiernan, 2000). Creation of crystals may occlude blood vessels and destroy tissue and cell structures. We therefore filtrated the fixative solution on the same day as the procedure.

As a result of the fixation process, two main problems may occur: over-fixation or under-fixation. In over-fixated tissue, the formation of too many cross-links and methylene bridges

may lead to unavailable epitopes, hence impaired antibody binding in IHC. In an under-fixed animal, the IHC analysis may also be affected. The morphology of cell structures may not be intact, causing problem with identifying single cells. Circulating antibodies from blood residues can also react with the IHC labelling and cause a background noise in the histological examinations.

#### **5.1.4 Cryoprotection and cryostat sectioning**

To study microglia activation and LD, brain sections with obtained tissue morphology and epitope reactivity were needed. Cryostat sectioning was used to produce brain sections by snap-freezing the brain tissue. When water freezes, the ice crystals formed can damage tissue and cell structures. To prevent the formation of intracellular ice crystals (freezing artefacts) when the brain was snap-frozen, it was placed in 30 % sucrose the day before cryostat sectioning. A hypertonic sucrose solution functioned as a cryoprotectant by removing water from the brain, hence contributes to preserving morphology and cell structures when snap frozen to first -40 °C then -20°C (Pegg, 2007). A limitation with sucrose is the increased risk of bacterial growth; therefore, sectioning was performed consecutively after the brain was fully saturated. Appropriate sucrose concentration and freezing temperature was essential for smooth sectioning. Too low temperature causes crumbled/breakable sections and too high temperature causes folded/rolled sections. The temperature of the cooling system was therefore observed during sectioning and based on previous experience with mouse brain on the microtome connected to the cryostat, -20 °C was a suitable temperature for sectioning.

#### **5.1.5 Immunohistochemistry**

Immunohistochemistry was used to reveal microglia and LD in the brain sections. High-quality and specific antibodies were fundamental for successive IHC labeling. We used secondary antibody with different fluorophores to visualize the antibody-antigen interactions in a confocal microscope.

**Antibodies:** Antibodies binds epitopes on antigens and are either monoclonal (mAb) or polyclonal antibodies (pAb). mAb react against one specific epitope per antigen as they arise from a single B-cell parent clone. pAb, on the other hand, originates from the immune response of several B-cells, hence can bind different epitopes on the same antigen (abcam, 2021b). Because mAb reacts to only one specific epitope they normally have a high

specificity and are less likely to cross-react with other proteins, while pAb originate from different B-cells are prone to a higher risk of cross reactivity and batch-to-batch variability. In this study, both mAb and pAb were used. mAb was used against GFAP on astrocytes and pAb was used against Iba1 on microglia. During the IHC procedure, the same batch of Iba1 pAb was used on all sections. An advantage of pAb is that their immunoreactivity is less affected by small amounts of tissue denaturation and structural changes, such as glycosylation of the epitope, as they react to different epitopes on the same antigen. The pAb may also possibly create a stronger visible signal, as several antibodies bind the target antigen/protein.

The fluorophores on the secondary antibody emit light at individual wavelengths when exposed to the correct absorption wavelength. Fluorescent IHC was beneficial in our study because we wanted to visualize numerous antigens simultaneously. This was possible using secondary antibodies with different fluorophores, originating from different species. Fluorescent IHC also gave the opportunity for obtaining high-resolution image quality, favorable for the quantitative analysis. A limitation with fluorescent IHC is that the fluorophores are less stable over time. When performing the IHC protocol, the sections were therefore covered in aluminum foil to prevent bleaching to occur over time.

## **5.2 Interpretation and discussion of findings**

### **5.2.1 Body composition**

Body composition measurements were obtained using Time Domain Nuclear Magnetic Resonance (TD-NMR). This is a time-saving and non-invasive method which analyses of the body composition and provides results in only 2-3 minutes per mouse. The results from the body composition showed that high-intensity interval exercise did not affect percentages of fat, lean or free body fluid in the mice. The percentage of fat, lean and body fluid for the exercised and sedentary *db/+* mice were constant throughout the intervention period. The *db/db* mice, on the other hand, increased their percentage of fat and decreased their percentage of “lean tissue” which also contains muscles, despite high-intensity exercise. According to the literature, *db/db* mice gets obese already at 3-4 weeks of age and have elevated plasma insulin throughout their 18 to 28-month life span (The Jackson Laboratory, 2021b). The mutation in the Leptin receptor (*Lepr*) causes a non-functional *Lepr*, hence the mice do not receive signals of satiety (Dornbush & Aeddula, 2021). It is shown that excess fat



accumulates in the *db/db* mice despite normal food intake (Coleman, 1978) and the animals in our study has unlimited access to food and water. Because of the extreme animal model, the *db/db* mice keep eating which may explain their steady increase in the percentage of fat. In older humans, T2DM is associated with increased trunk fat mass and severe loss of skeletal muscle (Park et al., 2009). The percentage of “lean” in the *db/db* mice decreases over the 8 weeks. This may be due to loss of skeletal muscle, but most likely represent an increase of body fat rather than an actual decrease in the absolute weight of skeletal muscle. An advantage of TD-NMR compared to other methods is that it does not require anesthesia and the placement of the animals in the tube is considered a non-invasive method. The use of Dual-energy X-ray absorptiometry (DXA) is also an approach used for body composition measures, and both TD-NMR and DXA provides reproducibility (Halldorsdottir, Carmody, Boozer, Leduc, & Leibel, 2009). Because body composition measures were taken every week during the intervention, the timesaving, non-invasive and non-anesthetized method was preferred for the animals.

### **5.2.2 Effect of exercise on microglia activation and lipid droplet number and morphology**

We hypothesize that T2DM induces pathological accumulation of lipids in LD in the brain and alter the composition of LD towards a less health phenotype. We further hypothesize that LD accumulation in microglia contributes to neuroinflammation and dementia in individuals with T2DM. Because the LD dynamics in skeletal muscle in patients with T2DM is shown to change with exercise to a healthier phenotype (Gemink et al., 2020) we wanted to investigate whether the same applied for LD in the brain.

Due to the limited time frame of this master project, the IHC images from the exercised mice in our study were not analyzed. If the analysis were performed, the effect of exercise and T2DM on LD number and size in microglia would be investigated.

### **5.2.3 Open field Exploration test**

The open field test was performed to assess locomotor activity, but also to assess the emotional state of the animal. It is a non-invasive test with the advantage of rapidly providing behavioral information on time spent exploring the arena, distance travelled and velocity. We found that the *db/db* had significantly less ambulatory movement and velocity than the *db/+*

mice. There were no statistically significant differences between the anxious state of the animal, although *db/db* mice tended to be more anxious compared to the *db/+* mice.

**Anxiety-like behavior:** The first 10 minutes of the test is used to assess the emotional state of the animal. This is based on the assumption that mice are naturally curious animals who would like to explore their surroundings (Seibenhener & Wooten, 2015), yet consider open and unknown environments as dangerous. An animal showing anxiety-like behavior tends to “hide” in the corners or along the walls of the open field arena. This is why we compare the duration of time spent in the periphery- with the duration of time spent in the center area during the first 10 minutes of the test. More time spent in the periphery, during the first 10 minutes was considered an indication of a more anxious animal, than the ones with higher duration in the center area.

The *db/db* mice tended to spend more time in the periphery compared to the *db/+* mice ( $p=0.0666$ , Mann-Whitney U test, GraphPad Prism). The *db/db* mice also tended to spend less time in the open center area compared to the *db/+* mice ( $p=0.1108$ , unpaired students t-test, GraphPad Prism). This may indicate that the *db/db* mice are slightly more anxious and/or more easily stressed than the *db/+* mice.

Other more specific anxiety tests exist, such as the elevated plus maze. The plus maze has 4 arms crossing in the center and is placed above the ground. Two oppositely standing arms have high walls, while the two other arms are open to the environment. The test is based on the same assumption as described for the open field test, namely that more anxious rodents tend to avoid the open areas. The elevated plus maze may assess more specifically or anxiety-like behavior, such as frequency of entries into the open zones-, the arms with walls- the central zone and time in these zones. The test is also recording the animals, assessing measures of signs like grooming and sniffing. Less time exploring the zones, a low number of entries to the open zones, more time spent in the arms with walls and less grooming and sniffing are among indications of an anxious animal (Belovicova, Bogi, Csatlosova, & Dubovicky, 2017). In the present study the mice were exposed to daily exercise, and we therefore aimed at keeping the behavioral test to a minimum, to avoid additional stress to the animals. Consequently, we chose not to perform an additional test for anxiety-like behavior specifically.

**Spontaneous locomotor activity:** The 50 last minutes of the test was used to assess spontaneous locomotor activity. The *db/db* mice had significantly lower total distance travelled in both the periphery ( $p = <0.0001$ , Mann-Whitney U test, GraphPad Prism) and the center area ( $p = <0.0001$ , unpaired students t-test, GraphPad Prism) of the arena compared to the *db/+* mice. The results indicate that the *db/db* mice naturally has less locomotor activity than the *db/+* mice. The ambulatory episode average velocity and the ambulatory episode peak average velocity was also significantly lower for the *db/db* mice, in both the center- and the periphery area, compared with the *db/+* mice ( $p = <0.0001$ , unpaired students t-test and Mann Whitney U test, GraphPad Prism). This indicated that the obese *db/db* mice had a lower speed when moving. This is perhaps not surprising based on their obese phenotype, but the information is useful when interpret the findings from the MWM test.

#### **5.2.4 Learning and memory performance in the Morris water maze**

In this study, we observed a positive effect of exercise on learning and memory performance and found a tendency for a decreased spatial memory in obese *db/db* mice compared to *db/+* mice. The Morris water maze (MWM) was used to assess data on learning and memory from the mice. The ability to learn and remember locations depends on the use of allocentric navigation which involves the hippocampus (Rinaldi et al., 2020). Allocentric navigation includes the use of distal cues outside the animal, which is mimicked in the MWM test by the use of pictures and objects placed in the MWM room. This creates a reliable method for assessing data on memory.

In general, the *db/+* exercised animals had the best memory of the platform location compared to the other groups. The *db/db* exercised mice had slightly better learning and memory performance than the *db/db* sedentary mice (but not statistically significant). The lack of statistical significance between the latter groups may result for the low number of sedentary *db/db* mice included in the study. Interestingly, these results suggest that exercise results improved MWM cognitive performance and that obesity caused impaired MWM cognitive performance.

The platform was located in the north zone during the training days, therefore time spent in the north zone during the probe trial indicated that the mouse was searching at the right place. The latency to the first entry to the north zone is also often used as a measure of how well the

animals remember where to search for the platform. In our study, the latency to first entry to the north zone was significantly lower for the *db/db* exercised mice compared to the *db/db* sedentary mice ( $p= 0.016$ , Kruskal-Wallis test, Dunn's test, GraphPad Prism). Although not reaching statistical significance, the exercise *db/db* mice tended to score better than the sedentary *db/db* at all other measures of spatial memory as well.

The *db/+* exercised mice had a significantly higher average number of entries to the north zone compared to the *db/+* sedentary ( $p= 0.037$ ) and the *db/db* sedentary ( $p=0.026$ , Kruskal-Wallis test, Dunn's test, GraphPad Prism). The platform zone is the main target zone, as it implies the previous location of the platform. The peri platform zone surrounds the platform, and time spent in this zone, hence indicate that the mouse remembers the platform area within the MWM pool. The *db/+* exercised mice had both higher number of entries to the peri-platform zone ( $p= 0.042$ , Dunn's multiple comparisons test, GraphPad Prism) and spent more time in the platform zone ( $p= 0.020$ , Dunn's multiple comparisons test, GraphPad Prism) compared to the *db/+* sedentary mice. Hence, we conclude that exercise seemed to increase the spatial memory in the *db/+* mice. Our data indicate that this may also be the case for the *db/db* mice, but the number of animals in the sedentary group of *db/db* mice need to be increased before a final conclusion can be drawn.

We also observed that *db/+* mice outperformed the *db/db* mice in most measures of spatial memory. These results have to be interpreted with care, however, as *db/db* exercised mice had significantly lower average swimming speed ( $p= 0.022$ ) ( $p= 0.014$ , Kruskal-Wallis test, Dunn's test, GraphPad Prism) and total distance traveled ( $p= 0.023$ ) ( $p= 0.015$ , Kruskal-Wallis test, Dunn's multiple comparisons test, GraphPad Prism) compared to the *db/+* sedentary and *db/+* exercised, respectively. The open field test also showed that the *db/db* mice had significantly lower ambulatory episode average velocity in both the center and the periphery of the arena ( $p= <0.0001$ , unpaired students t-test, GraphPad Prism) compared to the *db/+* mice. The total distance traveled during the open field test was also significantly lower for the *db/db* mice in both the center ( $p= <0.0001$ , unpaired students t-test, GraphPad Prism) and the periphery ( $p= <0.0001$ , Mann-Whitney U test, GraphPad Prism) of the arena compared to the *db/+* mice. This shows that the *db/db* mice have a lower psychometric tempo than the *db/+* mice, and therefore, latency to the different target zones was not used alone as a measure of memory in our study, but in combination with the number of entrances and time in

the zones. For instance, the *db/db* mice –once reaching a target zone– might spent longer time in the zones due to the lower swimming speed. All parameters mentioned in “4.6” was therefore assessed and used as metrics for learning and memory.

A limitation of the interpretation is that animals who did not enter some of the target zones within the 60-second trial were given a 60-second latency time. The latency time to the zones of interest may therefore contribute to underestimates, which may "camouflage" any differences between the genotype and treatment groups.

One final point worth mentioning is the fact that MWM takes place in water, which is expected to create motivation for the mouse to find the platform, but it may also cause stress for the animals. Results from the open field test indicated that the *db/db* mice may have a tendency towards a more anxiety-like phenotype. Theoretically, this could have created a stronger motivation in these animals to find the platform. There are no indications in our data from the MWM, however, that this was the case.

### 5.2.5 Microglia activation

This part of the study aimed to investigate neuroinflammation in T2DM and AD. Activated microglia changes from a ramified structure towards a more amoeboid phenotype with shorter processes, fewer junctions and an enlarged soma (Torres-Platas et al., 2014). Activated microglia show increased production of pro-inflammatory cytokines and produce elevated levels of ROS. These microglia changes are suggested to contribute to neuroinflammation and cognitive impairments (Wang et al., 2015). The results from this study were therefore used as an indication of whether neuroinflammation was present in the CA1 and CA3 of the hippocampus.

**Microglia activation in sedentary *db/db* and *db/+* mice:** We identified a tendency for more activated microglia in *db/db* mice than in the control animals. The microglia activation in the CA1 trended towards a higher microglia activation in *db/db* sedentary mice compared to *db/+* mice. This is interesting, as T2DM increase the risk for AD and neuroinflammation is suggested to contribute to the pathogenesis of AD (Kinney et al., 2018). Although there were not statistically significant differences, the average number of branches ( $p=0.094$ , unpaired students t-test, GraphPad Prism), junctions ( $p=0.095$ , unpaired students t-test, GraphPad

Prism), and end-point voxels ( $p= 0.093$ , unpaired students t-test, GraphPad Prism) in the CA1 region, the *db/db* mice had a tendency for a more activated microglia morphology compared to the *db/+* mice. Microglia activation in CA3 also had a pattern with a lower number of branches, junctions and end-points, but statistically this was not enough to be called a tendency.

There was only  $n= 3$  *db/+* mice and  $n= 4$  *db/db* mice in this analysis, which may explain why the differences were not detected statistically. With a higher number of animals in each group, it is conceivable that the differences between the groups would be statistically significant. The results are therefore interesting and can be used as an indication that further research on neuroinflammation in T2DM could be relevant.

**Microglia activation in 5xFAD and wild type mice:** We identified a higher density of microglia in the CA1 of 5xFAD mice compared to wt mice, indicating enhanced recruitments to- or proliferation of microglia in this region, which is a signal of active neuroinflammation. In the CA1 region, the microglia also were more activated than those in the wt mice. Further, we found a tendency of increased microglia activation in the CA3 of 5xFAD mice compared to wt mice. In total, we showed that microglia activation is present in mice with AD.

The presence of a sustained immune response in the brain has emerged as an essential part of the pathology of AD (Bronzuoli et al., 2016). In accordance with previous literature, we detected increased microglia activation in the mice with AD compared to the control wt mice. We found a significant higher microglia activation in the CA1 of 5xFAD mice compared to the CA1 in wt mice: The average number of branches ( $p= 0.013$ , unpaired students t-test, GraphPad Prism), junctions ( $p= 0.015$ , unpaired students t-test, GraphPad Prism), and end-point voxels ( $p= 0.012$ , unpaired students t-test, GraphPad Prism), were all consistent with a more activated phenotype in the AD mice. This supports the hypothesis of microglia activation in the pathology of AD.

Both the 5xFAD and *db/db* mice tended to have a higher degree of microglia activation in the CA1 of the hippocampus compared to their control groups. Interestingly, the same pattern of higher microglia activation in *db/db* and 5xFAD mice occurred in the CA3, but this tendency was lower than the ones in the CA1.

We quantified Iba1<sup>+</sup> and DAPI<sup>+</sup> cells in the CA1 and the CA3, as they are the principal pyramidal cell fields of the hippocampus with densely packed neurons and is important for memory and learning (Anand & Dhikav, 2012; Leuner & Gould, 2010). Microglia activation and the cause of dysregulation of these areas may therefore lead to cognitive impairments, and key symptoms for AD. In 5xFAD mice, the microglia cells were discovered as active in both regions, while the microglia cells in the wt mice showed more resting microglia morphology. The significant differences in microglia activation between 5xFAD and wt mice suggest that neuroinflammation is a part of the pathology mechanisms of AD. The same characteristic microglia activation was observed in sedentary *db/db* mice; however, due to the low number of animals, it requires more research to investigate any statistically significant differences.

**Image analysis:** Microglia activation analysis was performed using Fiji (ImageJ software) with Trainable Weka Segmentation (TWS) and further manual segmentation. LD was quantified manually using Fiji. Using TWS, the machine learning tool has both advantages and limitations.

The changes in morphology make automatic segmentation of microglia more advanced than many monotonous structures. This requires the TWS to be able to segment microglia with different branches number of junctions and soma sizes. Using TWS to segment microglia (Iba1<sup>+</sup> and DAPI<sup>+</sup> cells) creates the advantage of automatization with standardized requirements for what accounts as the region of interest (ROI) and therefore increase reproducibility. The confocal 3D z-stack images can also be analyzed as maximum capacity 2D projections, making the segmentation more reliable as the entire brain section (stack) are analyzed. Using TWS is therefore very efficient, analyzing numerous images in a much shorter time compared to a manual reconstruction of the ROI.

Manual segmentation of microglia, on the other hand, is very time-consuming and prone to error. Manual methods are less objective than automated TWS, one margin of error is therefore that the operator may consider an image with a milder requirement than another concerning the structure of processes on the microglia, for example, due to differences in the total microglia activation in the image. Optimally, the microglia analysis would be performed using an automated method, but due to the marking of unwanted ROIs and some wrongly marked ROIs, manually reconstruction was also necessary. The brain sections analyzed was 20  $\mu\text{m}$  thick. A possible margin of error may be that microglia processes reaches beyond the 20  $\mu\text{m}$  section and therefore had a ROI not covering the full span of all branches. To avoid

subjective judgements to affect the results of the current analysis, the procedure was performed by an observer who was blinded to the treatments and genotypes.

**Macros in microglia analysis:** The first step of the microglia image analysis was using a macro for preparation and processing of images. This adjusted all the images to the same settings, creating comparable 2D projection images with the same maximum intensity and contrast, and conversion to 8-bit greyscale. Since a part of the segmentation was manually performed, a macro merging the blue (DAPI) and red (Iba1) channel together was used. To ensure correct marking of ROIs the visualization of colored images was used to give more accurate results. It was not possible to be certain of what was microglia, nuclei and fragments by only visualize grayscale images. The macro led to the same result in regard to contrast, color and clarity, creating standardized comparable images. The macros were able to run several images at once, being a major time saving factor.

Some of the microglia had processes reaching out of the image or only showing some of its soma. The TWS crated ROIs for most of these. Since a lower number of branches, junctions, end-point and size was used as metrics for microglia activation, these ROIs were deleted manually to avoid incorrect measures of the microglia morphology. This was an advantage by using manual segmentation after the automated method, as no microglia had lower data because the structure was reaching out of the side of the image. All processed images that were considered not possible to segment, for example, because of under-fixation, were excluded from the study.

### 5.2.6 Lipid droplets in microglia

In this study, we aimed to investigate whether the activated microglia contained LD. We hypothesized that LD contributes to increased ROS and toxicity, hence contributes to the pathogenesis of AD.

**Lipid droplets within microglia of sedentary *db/db* and *db/+* mice:** We found no significant differences in the number of LD in the microglia of *db/db* and *db/+* mice. This suggests the microglia activation being independent of LD.

The *db/db* mice tended towards higher microglia activation in the CA1 compared to the *db/+* mice, although there was no tendency towards a different number ( $p= 0.6286$ , Mann Whitney



test, GraphPad Prism) or area ( $p= 0.6286$ , Mann Whitney test, GraphPad Prism) of LD in the microglia. The microglia activation in the CA3 area of *db/db* mice was observed not different from that in the *db/+* mice. There were no differences in the number ( $p= 0.6286$ , Mann Whitney test, GraphPad Prism), or area ( $p= 0.1143$ , Mann Whitney test, GraphPad Prism) of LD in the CA3 region of the *db/db* and the *db/+* mice. Although it appeared that the *db/+* mice had a tendency towards a slightly higher average number of LDs in the microglia, this did not reach statistical significance. This is interesting, non the less, as it is the opposite of our hypothesis. In addition to no statistical differences in LD count, the area of the LD did not deviate between the genotypes. The LD count in the CA1 was lower than in the CA3, opposite than expected based on the microglia activation. This indicates that the LD in *db/db* mice is not larger in size and number, which was our hypothesis. It is not known, however, whether increase LD in microglia would be a driver or a consequence of microglia activation. Neither is it known if LD may accumulate in other brain cells if the microglia are activated. One possibility is that the activated microglia lose their ability to remove toxic lipid product, so that these remain in neurons or other cells.

The correlation between microglia activation and the content of LD was also studied, and there was a positive correlation between microglia activation (number of junctions) and the number of LD in the CA3 of *db/+* mice. This indicates that with a decreased microglia activation (resting state, hence increased junctions), the LD increases. This may support an assumption that activated microglia are less efficient at removing toxic lipids products, and this may in turn contribute to neurodegeneration. Further studies are needed to investigate this, for instance analysis of LD content in neurons.

The number of *db/db* ( $n= 4$ ) and *db/+* ( $n= 3$ ) are low and we cannot exclude the possibility that a larger number of animals could have revealed significant differences. Our data do not, however, point to that. In the correlation tests outliers were not removed, hence the statistically significant correlation between number of microglia junctions and the number of LD in the CA3 in *db/+* mice may differ without outliers.

**Lipid droplets within microglia of 5xFAD and wild type mice:** In the quantitative analysis on LD in microglia of 5xFAD and wt mice, there was a significantly lower area of LD in the CA3 in 5xFAD mice ( $p= 0.0234$ , unpaired students t-test, GraphPad Prism) compared to wt

mice. Other than that, there were no differences in LD size or number between the 5xFAD and control mice. The correlation test between increased microglia activation and LD number or area in 5xFAD and wt mice showed no significant correlation in any groups.

We hypothesized that activated microglia contained a higher number-, and larger sized LD compared to ramified microglia. There was significantly higher microglia activation in CA1 in 5xFAD mice compared to wt mice, but no differences in LD. This suggests the microglia activation being independent of microglial LD. In addition, 5xFAD mice had a statistically lower area of the LD present in CA3 compared to wt. This rejects our hypothesis that LD within the microglia is contributing to a less healthy phenotype of microglia and contributes to the mechanisms of AD. As discussed above, however, the density of LD in other brain cells may change the interpretations of these data.

The study from Marschallinger et. al. contradicts our results. They found a significantly higher number- of enlarged sized LD in microglia of 20-month-old mice. The 5xFAD and wt mice in our study varied from 39-49 weeks of age. Three of the wt type mice were 49 weeks old, while only two tg 5xFAD mice were 49 weeks. The results of the microglia analysis showed significantly higher microglia activation in CA1 in 5xFAD mice compared to the wt mice, hence the age difference should not cause that much change in the results. The microglia activation in the CA3 area of 5xFAD mice did not deviate from the control mice, although microglia in the CA3 of 5xFAD mice had a significantly lower area of LDs. Our AD mouse model had a specific A $\beta$  pathology and was a severe AD model. In their study, Marschallinger et. al. used *GRN*<sup>-/-</sup> mice, a model for frontotemporal dementia. This raises the question of whether the difference in LD results is due to different mouse models.

**Image analysis:** The LD analysis was manually performed to only quantify LD inside microglia, but also to exclude other unwanted fragments identified by the BODIPY staining that were not LD. Myelin is also labeled by BODIPY, hence making it difficult for an automated method to recognize only the small LD as ROIs. Some circular shapes in the myelin, for instance if the axons are cut perpendicularly, may look like LD, but often with less intensity in comparison. Some of the *db/db* mice were under-fixated, resulting in more background from erythrocytes. This labeling can easily be recognized by the trained eye, but it takes time to train the algorithm to do the same discrimination, and this must be optimized

for each experiment. This is another reason why an automated method was difficult to perform on the LD. When the z-stack is projected to a 2D image, some microglia may seem to contain LD, even when these LD are in another dimension in the brain section. To be certain that only microglial LD were quantified, all images were analyzed comparing with the z-stack. This was performed by an operator who was blinded to the genotypes.

## 6 Conclusion

This thesis aimed to investigate the effects of obesity and exercise on neuroinflammation and cognitive impairment. Additionally, the effects of neuroinflammation on cognitive function has been investigated by using the 5xFAD model for AD. This thesis further investigates the role of LD concerning microglia activation and neuroinflammation in the hippocampal CA1 and CA3. The 8 weeks of high-intensity interval exercise for 5 days/week improved cognitive performance of *db/db* mice in the MWM test, but the preventive effect on neuroinflammation is yet to be investigated. The obese *db/db* mice have worse spatial memory compared to the *db/+* mice in the MWM test. Microglia activation is present in both the diabetic animal model and the AD animal model, indicating neuroinflammation with activated microglia as a key mechanism for cognitive impairments. The microglia activation appeared to be independent of the LD accumulation as no significant differences in the density of LD was found within the activated microglia.

The results of this study demonstrate that *db/db* and 5xFAD mice have higher microglia activation in the hippocampal CA1 compared to their controls, although this was not due to the content of LD within the microglia. At the level of each individual cell, the increase of microglia activation did not correlate with increased LD accumulation. We further found exercise to have a positive effect on learning and memory performance, where obesity had a negative effect on learning and memory performance. These results support the hypothesis that exercise contributes to positive effects on cognition. The findings may contribute to further investigations of the LD function in the brain and AD pathology, and it would be interesting to investigate the effect of exercise on LD dynamics in the brain, especially in other cells than microglia.



# References

- abcam. (2021a). Anti-GFAP antibody (ab7260). Retrieved from <https://www.abcam.com/gfap-antibody-ab7260.html>
- abcam. (2021b). What are polyclonal, monoclonal and recombinant antibodies? Retrieved from <https://www.abcam.com/protocols/a-comparison-between-polyclonal-and-monoclonal>
- Allen Institute for Brain Science. (2008). Mouse Brain Reference Atlas. Retrieved from [http://mouse.brain-map.org/experiment/thumbnails/100142144?image\\_type=atlas](http://mouse.brain-map.org/experiment/thumbnails/100142144?image_type=atlas)
- Anand, K. S., & Dhikav, V. (2012). Hippocampus in health and disease: An overview. *Ann Indian Acad Neurol*, 15(4), 239-246. doi:10.4103/0972-2327.104323
- Arganda-Carreras, I., Kaynig, V., Rueden, C., Eliceiri, K. W., Schindelin, J., Cardona, A., & Sebastian Seung, H. (2017). Trainable Weka Segmentation: a machine learning tool for microscopy pixel classification. *Bioinformatics*, 33(15), 2424-2426. doi:10.1093/bioinformatics/btx180
- Arnold, S. E., Arvanitakis, Z., Macauley-Rambach, S. L., Koenig, A. M., Wang, H. Y., Ahima, R. S., . . . Nathan, D. M. (2018). Brain insulin resistance in type 2 diabetes and Alzheimer disease: concepts and conundrums. *Nat Rev Neurol*, 14(3), 168-181. doi:10.1038/nrneurol.2017.185
- Bailey, K. R., & Crawley, J. N. (2009). Anxiety-Related Behaviors in Mice. In J. J. Buccafusco (Ed.), *Methods of Behavior Analysis in Neuroscience* (2nd ed., pp. Chapter 5.3). Boca Raton (FL): CRC Press/Taylor & Francis: Copyright © 2009, Taylor & Francis Group, LLC.
- Balducci, S., Zanuso, S., Nicolucci, A., De Feo, P., Cavallo, S., Cardelli, P., . . . Pugliese, G. (2010). Effect of an intensive exercise intervention strategy on modifiable cardiovascular risk factors in subjects with type 2 diabetes mellitus: a randomized controlled trial: the Italian Diabetes and Exercise Study (IDES). *Arch Intern Med*, 170(20), 1794-1803. doi:10.1001/archinternmed.2010.380
- Bateman, R. J., Xiong, C., Benzinger, T. L. S., Fagan, A. M., Goate, A., Fox, N. C., . . . Morris, J. C. (2012). Clinical and Biomarker Changes in Dominantly Inherited Alzheimer's Disease. *New England Journal of Medicine*, 367(9), 795-804. doi:10.1056/NEJMoa1202753
- Belovicova, K., Bogi, E., Csatoslova, K., & Dubovicky, M. (2017). Animal tests for anxiety-like and depression-like behavior in rats. *Interdiscip Toxicol*, 10(1), 40-43. doi:10.1515/intox-2017-0006
- Blázquez, E., Velázquez, E., Hurtado-Carneiro, V., & Ruiz-Albusac, J. M. (2014). Insulin in the brain: its pathophysiological implications for States related with central insulin resistance, type 2 diabetes and Alzheimer's disease. *Front Endocrinol (Lausanne)*, 5, 161. doi:10.3389/fendo.2014.00161
- Boche, D., Perry, V. H., & Nicoll, J. A. (2013). Review: activation patterns of microglia and their identification in the human brain. *Neuropathol Appl Neurobiol*, 39(1), 3-18. doi:10.1111/nan.12011
- Bonadonna, R. C., & De Fronzo, R. A. (1991). Glucose metabolism in obesity and type 2 diabetes. *Diabete Metab*, 17(1 Pt 2), 112-135.
- Bronzuoli, M. R., Iacomino, A., Steardo, L., & Scuderi, C. (2016). Targeting neuroinflammation in Alzheimer's disease. *J Inflamm Res*, 9, 199-208. doi:10.2147/jir.S86958

- Bruker. (2021). minispec LF Series; Body Composition Analysis of Mice and Rats Retrieved from <https://www.bruker.com/en/products-and-solutions/mr/nmr-epr-td-nmr-industrial-solutions/minispec-lf-series.html>
- Bækkerud, F. H., Salerno, S., Ceriotti, P., Morland, C., Storm-Mathisen, J., Bergersen, L. H., . . . Stølen, T. O. (2019). High Intensity Interval Training Ameliorates Mitochondrial Dysfunction in the Left Ventricle of Mice with Type 2 Diabetes. *Cardiovasc Toxicol*, *19*(5), 422-431. doi:10.1007/s12012-019-09514-z
- Campbell, S. (2021). The Search for a Drug to End Alzheimer's. *IEEE Pulse*, *12*(2), 2-7. doi:10.1109/mpuls.2021.3066715
- Carty, M., & Bowie, A. G. (2011). Evaluating the role of Toll-like receptors in diseases of the central nervous system. *Biochem Pharmacol*, *81*(7), 825-837. doi:10.1016/j.bcp.2011.01.003
- Chavanelle, V., Boisseau, N., Otero, Y. F., Combaret, L., Dardevet, D., Montaurier, C., . . . Sirvent, P. (2017). Effects of high-intensity interval training and moderate-intensity continuous training on glycaemic control and skeletal muscle mitochondrial function in db/db mice. *Sci Rep*, *7*(1), 204. doi:10.1038/s41598-017-00276-8
- Cho, N. H., Shaw, J. E., Karuranga, S., Huang, Y., da Rocha Fernandes, J. D., Ohlrogge, A. W., & Malanda, B. (2018). IDF Diabetes Atlas: Global estimates of diabetes prevalence for 2017 and projections for 2045. *Diabetes Res Clin Pract*, *138*, 271-281. doi:10.1016/j.diabres.2018.02.023
- Christ, A., Lauterbach, M., & Latz, E. (2019). Western Diet and the Immune System: An Inflammatory Connection. *Immunity*, *51*(5), 794-811. doi:10.1016/j.immuni.2019.09.020
- Chu, B., Marwaha, K., Sanvictores, T., & Ayers, D. (2021). Physiology, Stress Reaction. In *StatPearls*. Treasure Island (FL): StatPearls Publishing Copyright © 2021, StatPearls Publishing LLC.
- Clarke, T. (2002). Mice make medical history. *Nature*. doi:10.1038/news021202-10
- Coleman, D. L. (1978). Obese and diabetes: two mutant genes causing diabetes-obesity syndromes in mice. *Diabetologia*, *14*(3), 141-148. doi:10.1007/bf00429772
- Craft, S., Baker, L. D., Montine, T. J., Minoshima, S., Watson, G. S., Claxton, A., . . . Gerton, B. (2012). Intranasal insulin therapy for Alzheimer disease and amnesic mild cognitive impairment: a pilot clinical trial. *Arch Neurol*, *69*(1), 29-38. doi:10.1001/archneurol.2011.233
- Crews, F., & Vetreno, R. (2015). Mechanisms of neuroimmune gene induction in alcoholism. *Psychopharmacology*, *233*. doi:10.1007/s00213-015-3906-1
- Cummings, J., Aisen, P., Lemere, C., Atri, A., Sabbagh, M., & Salloway, S. (2021). Aducanumab produced a clinically meaningful benefit in association with amyloid lowering. *Alzheimers Res Ther*, *13*(1), 98. doi:10.1186/s13195-021-00838-z
- Daemen, S., Gemmink, A., Brouwers, B., Meex, R. C. R., Huntjens, P. R., Schaart, G., . . . Hesselink, M. K. C. (2018). Distinct lipid droplet characteristics and distribution unmask the apparent contradiction of the athlete's paradox. *Mol Metab*, *17*, 71-81. doi:10.1016/j.molmet.2018.08.004
- Daryabor, G., Atashzar, M. R., Kabelitz, D., Meri, S., & Kalantar, K. (2020). The Effects of Type 2 Diabetes Mellitus on Organ Metabolism and the Immune System. *Front Immunol*, *11*, 1582. doi:10.3389/fimmu.2020.01582

- de la Monte, S. M., & Wands, J. R. (2008). Alzheimer's disease is type 3 diabetes-evidence reviewed. *J Diabetes Sci Technol*, 2(6), 1101-1113.  
doi:10.1177/193229680800200619
- De Meyts, P. (2000). The Insulin Receptor and Its Signal Transduction Network. In K. R. Feingold, B. Anawalt, A. Boyce, G. Chrousos, W. W. de Herder, K. Dhatariya, K. Dungan, A. Grossman, J. M. Hershman, J. Hofland, S. Kalra, G. Kaltsas, C. Koch, P. Kopp, M. Korbonits, C. S. Kovacs, W. Kuohung, B. Laferrère, E. A. McGee, R. McLachlan, J. E. Morley, M. New, J. Purnell, R. Sahay, F. Singer, C. A. Stratakis, D. L. Trencé, & D. P. Wilson (Eds.), *Endotext*. South Dartmouth (MA): MDText.com, Inc. Copyright © 2000-2021, MDText.com, Inc.
- DeFronzo, R. A., Ferrannini, E., Groop, L., Henry, R. R., Herman, W. H., Holst, J. J., . . . Weiss, R. (2015). Type 2 diabetes mellitus. *Nat Rev Dis Primers*, 1, 15019.  
doi:10.1038/nrdp.2015.19
- Dionisio-Santos, D. A., Olschowka, J. A., & O'Banion, M. K. (2019). Exploiting microglial and peripheral immune cell crosstalk to treat Alzheimer's disease. *Journal of Neuroinflammation*, 16(1), 74. doi:10.1186/s12974-019-1453-0
- DiSabato, D. J., Quan, N., & Godbout, J. P. (2016). Neuroinflammation: the devil is in the details. *J Neurochem*, 139 Suppl 2(Suppl 2), 136-153. doi:10.1111/jnc.13607
- Dornbush, S., & Aeddula, N. R. (2021). Physiology, Leptin. In *StatPearls*. Treasure Island (FL): StatPearls Publishing  
Copyright © 2021, StatPearls Publishing LLC.
- Du Yan, S., Zhu, H., Fu, J., Yan, S. F., Roher, A., Tourtellotte, W. W., . . . Schmidt, A. M. (1997). Amyloid-beta peptide-receptor for advanced glycation endproduct interaction elicits neuronal expression of macrophage-colony stimulating factor: a proinflammatory pathway in Alzheimer disease. *Proc Natl Acad Sci U S A*, 94(10), 5296-5301.  
doi:10.1073/pnas.94.10.5296
- Erion, J. R., Wosiski-Kuhn, M., Dey, A., Hao, S., Davis, C. L., Pollock, N. K., & Stranahan, A. M. (2014). Obesity elicits interleukin 1-mediated deficits in hippocampal synaptic plasticity. *J Neurosci*, 34(7), 2618-2631. doi:10.1523/jneurosci.4200-13.2014
- Farese, R. V., & Walther, T. C. (2009). Lipid Droplets Finally Get a Little R-E-S-P-E-C-T. *Cell*, 139(5), 855-860. doi:<https://doi.org/10.1016/j.cell.2009.11.005>
- Farmer, B. C., Kluemper, J., & Johnson, L. A. (2019). Apolipoprotein E4 Alters Astrocyte Fatty Acid Metabolism and Lipid Droplet Formation. *Cells*, 8(2). doi:10.3390/cells8020182
- Farmer, B. C., Walsh, A. E., Kluemper, J. C., & Johnson, L. A. (2020). Lipid Droplets in Neurodegenerative Disorders. *Front Neurosci*, 14, 742. doi:10.3389/fnins.2020.00742
- Fordyce, D. E., & Farrar, R. P. (1991). Enhancement of spatial learning in F344 rats by physical activity and related learning-associated alterations in hippocampal and cortical cholinergic functioning. *Behav Brain Res*, 46(2), 123-133. doi:10.1016/s0166-4328(05)80105-6
- Fowler, S. D., Mayer, E. P., & Greenspan, P. (1985). Foam cells and atherogenesis. *Ann N Y Acad Sci*, 454, 79-90. doi:10.1111/j.1749-6632.1985.tb11846.x
- Gage, G. J., Kipke, D. R., & Shain, W. (2012). Whole animal perfusion fixation for rodents. *J Vis Exp*(65). doi:10.3791/3564
- Gemmink, A., Schrauwen, P., & Hesselink, M. K. C. (2020). Exercising your fat (metabolism) into shape: a muscle-centred view. *Diabetologia*, 63(8), 1453-1463.  
doi:10.1007/s00125-020-05170-z



- Geser, C. A. (1976). Hormonal interactions in carbohydrate metabolism. *Int Z Vitam Ernahrungsforsch Beih*, 15, 58-65.
- Gjøra, L., Strand, B. H., Bergh, S., Borza, T., Brækhus, A., Engedal, K., . . . Selbæk, G. (2021). Current and Future Prevalence Estimates of Mild Cognitive Impairment, Dementia, and Its Subtypes in a Population-Based Sample of People 70 Years and Older in Norway: The HUNT Study. *J Alzheimers Dis*, 79(3), 1213-1226. doi:10.3233/jad-201275
- Gould, E., Beylin, A., Tanapat, P., Reeves, A., & Shors, T. J. (1999). Learning enhances adult neurogenesis in the hippocampal formation. *Nat Neurosci*, 2(3), 260-265. doi:10.1038/6365
- Gregor, M. F., & Hotamisligil, G. S. (2011). Inflammatory mechanisms in obesity. *Annu Rev Immunol*, 29, 415-445. doi:10.1146/annurev-immunol-031210-101322
- Gudala, K., Bansal, D., Schifano, F., & Bhansali, A. (2013). Diabetes mellitus and risk of dementia: A meta-analysis of prospective observational studies. *Journal of Diabetes Investigation*, 4(6), 640-650. doi:<https://doi.org/10.1111/jdi.12087>
- Hagan, C. (2017). WHEN ARE MICE CONSIDERED OLD? Retrieved from <https://www.jax.org/news-and-insights/jax-blog/2017/november/when-are-mice-considered-old#:~:text=Mature%20adult%20mice%20range%20in,ranges%20from%2020%20%2D%2030%20years.>
- Halldorsdottir, S., Carmody, J., Boozer, C. N., Leduc, C. A., & Leibel, R. L. (2009). Reproducibility and accuracy of body composition assessments in mice by dual energy x-ray absorptiometry and time domain nuclear magnetic resonance. *Int J Body Compos Res*, 7(4), 147-154.
- Hardy, J. A., & Higgins, G. A. (1992). Alzheimer's disease: the amyloid cascade hypothesis. *Science*, 256(5054), 184-185. doi:10.1126/science.1566067
- He, J., Goodpaster, B. H., & Kelley, D. E. (2004). Effects of weight loss and physical activity on muscle lipid content and droplet size. *Obes Res*, 12(5), 761-769. doi:10.1038/oby.2004.92
- Hepner, F. L., Ransohoff, R. M., & Becher, B. (2015). Immune attack: the role of inflammation in Alzheimer disease. *Nat Rev Neurosci*, 16(6), 358-372. doi:10.1038/nrn3880
- Hippius, H., & Neundörfer, G. (2003). The discovery of Alzheimer's disease. *Dialogues Clin Neurosci*, 5(1), 101-108. doi:10.31887/DCNS.2003.5.1/hhippius
- Howat, W. J., & Wilson, B. A. (2014). Tissue fixation and the effect of molecular fixatives on downstream staining procedures. *Methods*, 70(1), 12-19. doi:10.1016/j.ymeth.2014.01.022
- Huang, X., Liu, G., Guo, J., & Su, Z. (2018). The PI3K/AKT pathway in obesity and type 2 diabetes. *Int J Biol Sci*, 14(11), 1483-1496. doi:10.7150/ijbs.27173
- Itabe, H., Yamaguchi, T., Nimura, S., & Sasabe, N. (2017). Perilipins: a diversity of intracellular lipid droplet proteins. *Lipids Health Dis*, 16(1), 83. doi:10.1186/s12944-017-0473-y
- Jarc, E., & Petan, T. (2020). A twist of FATE: Lipid droplets and inflammatory lipid mediators. *Biochimie*, 169, 69-87. doi:10.1016/j.biochi.2019.11.016
- Kahn, S. E., Cooper, M. E., & Del Prato, S. (2014). Pathophysiology and treatment of type 2 diabetes: perspectives on the past, present, and future. *Lancet*, 383(9922), 1068-1083. doi:10.1016/s0140-6736(13)62154-6

- Karch, C. M., & Goate, A. M. (2015). Alzheimer's disease risk genes and mechanisms of disease pathogenesis. *Biol Psychiatry*, *77*(1), 43-51. doi:10.1016/j.biopsych.2014.05.006
- Kasukurthi, R., Brenner, M. J., Moore, A. M., Moradzadeh, A., Ray, W. Z., Santosa, K. B., . . . Hunter, D. A. (2009). Transcardial perfusion versus immersion fixation for assessment of peripheral nerve regeneration. *J Neurosci Methods*, *184*(2), 303-309. doi:10.1016/j.jneumeth.2009.08.019
- Kiernan, J. A. (2000). Formaldehyde, Formalin, Paraformaldehyde And Glutaraldehyde: What They Are And What They Do. *Microscopy Today*, *8*(1), 8-13. doi:10.1017/S1551929500057060
- Kimura, R., & Ohno, M. (2009). Impairments in remote memory stabilization precede hippocampal synaptic and cognitive failures in 5XFAD Alzheimer mouse model. *Neurobiol Dis*, *33*(2), 229-235. doi:10.1016/j.nbd.2008.10.006
- Kinney, J. W., Bemiller, S. M., Murtishaw, A. S., Leisgang, A. M., Salazar, A. M., & Lamb, B. T. (2018). Inflammation as a central mechanism in Alzheimer's disease. *Alzheimers Dement (N Y)*, *4*, 575-590. doi:10.1016/j.trci.2018.06.014
- Koffie, R. M., Hashimoto, T., Tai, H. C., Kay, K. R., Serrano-Pozo, A., Joyner, D., . . . Spire-Jones, T. L. (2012). Apolipoprotein E4 effects in Alzheimer's disease are mediated by synaptotoxic oligomeric amyloid- $\beta$ . *Brain*, *135*(Pt 7), 2155-2168. doi:10.1093/brain/aws127
- Krahmer, N., Farese, R. V., Jr., & Walther, T. C. (2013). Balancing the fat: lipid droplets and human disease. *EMBO Mol Med*, *5*(7), 973-983. doi:10.1002/emmm.201100671
- Kuniishi, H., Ichisaka, S., Yamamoto, M., Ikubo, N., Matsuda, S., Futora, E., . . . Hata, Y. (2017). Early deprivation increases high-leaning behavior, a novel anxiety-like behavior, in the open field test in rats. *Neurosci Res*, *123*, 27-35. doi:10.1016/j.neures.2017.04.012
- Lee, H. J., Seo, H. I., Cha, H. Y., Yang, Y. J., Kwon, S. H., & Yang, S. J. (2018). Diabetes and Alzheimer's Disease: Mechanisms and Nutritional Aspects. *Clin Nutr Res*, *7*(4), 229-240. doi:10.7762/cnr.2018.7.4.229
- Lee, T. H., & Yau, S. Y. (2020). From Obesity to Hippocampal Neurodegeneration: Pathogenesis and Non-Pharmacological Interventions. *Int J Mol Sci*, *22*(1). doi:10.3390/ijms22010201
- Leto, D., & Saltiel, A. R. (2012). Regulation of glucose transport by insulin: traffic control of GLUT4. *Nature Reviews Molecular Cell Biology*, *13*(6), 383-396. doi:10.1038/nrm3351
- Leuner, B., & Gould, E. (2010). Structural plasticity and hippocampal function. *Annu Rev Psychol*, *61*, 111-140, c111-113. doi:10.1146/annurev.psych.093008.100359
- Li, Q., & Barres, B. A. (2018). Microglia and macrophages in brain homeostasis and disease. *Nature Reviews Immunology*, *18*(4), 225-242. doi:10.1038/nri.2017.125
- Li, R., Jia, Z., & Trush, M. A. (2016). Defining ROS in Biology and Medicine. *React Oxyg Species (Apex)*, *1*(1), 9-21. doi:10.20455/ros.2016.803
- Li, X., Li, Z., Zhao, M., Nie, Y., Liu, P., Zhu, Y., & Zhang, X. (2019). Skeletal Muscle Lipid Droplets and the Athlete's Paradox. *Cells*, *8*(3). doi:10.3390/cells8030249
- Liu, L., MacKenzie, K. R., Putluri, N., Maletić-Savatić, M., & Bellen, H. J. (2017). The Glia-Neuron Lactate Shuttle and Elevated ROS Promote Lipid Synthesis in Neurons and Lipid Droplet Accumulation in Glia via APOE/D. *Cell Metab*, *26*(5), 719-737.e716. doi:10.1016/j.cmet.2017.08.024

- Liu, L., Zhang, K., Sandoval, H., Yamamoto, S., Jaiswal, M., Sanz, E., . . . Bellen, H. J. (2015). Glial lipid droplets and ROS induced by mitochondrial defects promote neurodegeneration. *Cell*, *160*(1-2), 177-190. doi:10.1016/j.cell.2014.12.019
- Maia, M. A., & Sousa, E. (2019). BACE-1 and  $\gamma$ -Secretase as Therapeutic Targets for Alzheimer's Disease. *Pharmaceuticals (Basel)*, *12*(1). doi:10.3390/ph12010041
- Marschallinger, J., Iram, T., Zardeneta, M., Lee, S. E., Lehallier, B., Haney, M. S., . . . Wyss-Coray, T. (2020). Lipid-droplet-accumulating microglia represent a dysfunctional and proinflammatory state in the aging brain. *Nat Neurosci*, *23*(2), 194-208. doi:10.1038/s41593-019-0566-1
- Molinuevo, J. L., Ayton, S., Batrla, R., Bednar, M. M., Bittner, T., Cummings, J., . . . Blennow, K. (2018). Current state of Alzheimer's fluid biomarkers. *Acta Neuropathol*, *136*(6), 821-853. doi:10.1007/s00401-018-1932-x
- Morgan, D. (2009). Frontiers in Neuroscience. *Water Maze Tasks in Mice: Special Reference to Alzheimer's Transgenic Mice*. . In J. J. Buccafusco (Ed.), *Methods of Behavior Analysis in Neuroscience*. Boca Raton (FL): CRC Press/Taylor & Francis  
Copyright © 2009, Taylor & Francis Group, LLC.
- Morland, C., Andersson, K. A., Haugen, Ø. P., Hadzic, A., Kleppa, L., Gille, A., . . . Bergersen, L. H. (2017). Exercise induces cerebral VEGF and angiogenesis via the lactate receptor HCAR1. *Nature Communications*, *8*(1), 15557. doi:10.1038/ncomms15557
- Mosser, D. M., & Edwards, J. P. (2008). Exploring the full spectrum of macrophage activation. *Nat Rev Immunol*, *8*(12), 958-969. doi:10.1038/nri2448
- Murphy, D. J. (2001). The biogenesis and functions of lipid bodies in animals, plants and microorganisms. *Prog Lipid Res*, *40*(5), 325-438. doi:10.1016/s0163-7827(01)00013-3
- Nave, K. A., Tzvetanova, I. D., & Schirmeier, S. (2017). Glial Cell Evolution: The Origins of a Lipid Store. *Cell Metab*, *26*(5), 701-702. doi:10.1016/j.cmet.2017.10.011
- New England BioLabs. (2021a). OneTaq® 2X Master Mix with Standard Buffer. Retrieved from <https://international.neb.com/products/m0482-onetaq-2x-master-mix-with-standard-buffer#Quality,%20Safety%20&%20Legal>
- New England BioLabs. (2021b). Proteinase K, Molecular Biology Grade. Retrieved from <https://www.neb.uk.com/products/neb-catalogue/protein-analysis,-exp-purification/proteinase-k,-molecular-biology-grade>
- Oakley, H., Cole, S. L., Logan, S., Maus, E., Shao, P., Craft, J., . . . Vassar, R. (2006). Intraneuronal beta-amyloid aggregates, neurodegeneration, and neuron loss in transgenic mice with five familial Alzheimer's disease mutations: potential factors in amyloid plaque formation. *J Neurosci*, *26*(40), 10129-10140. doi:10.1523/jneurosci.1202-06.2006
- Oddo, S., Caccamo, A., Shepherd, J. D., Murphy, M. P., Golde, T. E., Kaye, R., . . . LaFerla, F. M. (2003). Triple-transgenic model of Alzheimer's disease with plaques and tangles: intracellular Abeta and synaptic dysfunction. *Neuron*, *39*(3), 409-421. doi:10.1016/s0896-6273(03)00434-3
- Ohno, M., Chang, L., Tseng, W., Oakley, H., Citron, M., Klein, W. L., . . . Disterhoft, J. F. (2006). Temporal memory deficits in Alzheimer's mouse models: rescue by genetic deletion of BACE1. *Eur J Neurosci*, *23*(1), 251-260. doi:10.1111/j.1460-9568.2005.04551.x
- Ohno, M., Cole, S. L., Yasvoina, M., Zhao, J., Citron, M., Berry, R., . . . Vassar, R. (2007). BACE1 gene deletion prevents neuron loss and memory deficits in 5XFAD APP/PS1 transgenic mice. *Neurobiol Dis*, *26*(1), 134-145. doi:10.1016/j.nbd.2006.12.008

- Park, S. W., Goodpaster, B. H., Lee, J. S., Kuller, L. H., Boudreau, R., de Rekeneire, N., . . . Newman, A. B. (2009). Excessive loss of skeletal muscle mass in older adults with type 2 diabetes. *Diabetes Care*, *32*(11), 1993-1997. doi:10.2337/dc09-0264
- Parrott, C., Ghosh, P., Tedeschi, J., Gunasekara, G., & Broderick, T. (2011). Urinary corticosterone and normetanephrine levels after voluntary wheel and forced treadmill running in the db/db mouse. *Journal of Diabetes Mellitus*, *01*, 71-78. doi:10.4236/jdm.2011.14011
- Patterson, C. (2018). *World Alzheimer Report 2018* Retrieved from London
- Paxinos, G., & Franklin, K. B. J. (2004). *The Mouse Brain in Stereotaxic Coordinates* (2nd ed.). USA: Elsevier Science.
- Pegg, D. E. (2007). Principles of cryopreservation. *Methods Mol Biol*, *368*, 39-57. doi:10.1007/978-1-59745-362-2\_3
- Peng, B. Y., Wang, Q., Luo, Y. H., He, J. F., Tan, T., & Zhu, H. (2018). A novel and quick PCR-based method to genotype mice with a leptin receptor mutation (db/db mice). *Acta Pharmacol Sin*, *39*(1), 117-123. doi:10.1038/aps.2017.52
- Penno, A., Hackenbroich, G., & Thiele, C. (2013). Phospholipids and lipid droplets. *Biochimica et Biophysica Acta (BBA) - Molecular and Cell Biology of Lipids*, *1831*(3), 589-594. doi:<https://doi.org/10.1016/j.bbalip.2012.12.001>
- Poirier, J. (1994). Apolipoprotein E in animal models of CNS injury and in Alzheimer's disease. *Trends Neurosci*, *17*(12), 525-530. doi:10.1016/0166-2236(94)90156-2
- Purves D, Augustine GJ, Fitzpatrick D, & et al., e. (2001). *Neuroscience. 2nd edition. Long-Term Synaptic Depression*. (2nd ed.). Sunderland (MA): Sinauer Associates.
- Quesenberry, K. E., & Donnelly, T. M. (2020). Breeding and Reproduction of Mice. Retrieved from <https://www.merckvetmanual.com/all-other-pets/mice/breeding-and-reproduction-of-mice>
- Ramos-Vara, J. A. (2005). Technical aspects of immunohistochemistry. *Vet Pathol*, *42*(4), 405-426. doi:10.1354/vp.42-4-405
- Ransohoff, R. M., Schafer, D., Vincent, A., Blachère, N. E., & Bar-Or, A. (2015). Neuroinflammation: Ways in Which the Immune System Affects the Brain. *Neurotherapeutics*, *12*(4), 896-909. doi:10.1007/s13311-015-0385-3
- Reed-Geaghan, E. G., Savage, J. C., Hise, A. G., & Landreth, G. E. (2009). CD14 and toll-like receptors 2 and 4 are required for fibrillar A $\beta$ -stimulated microglial activation. *J Neurosci*, *29*(38), 11982-11992. doi:10.1523/jneurosci.3158-09.2009
- Reitz, C., & Mayeux, R. (2014). Alzheimer disease: epidemiology, diagnostic criteria, risk factors and biomarkers. *Biochem Pharmacol*, *88*(4), 640-651. doi:10.1016/j.bcp.2013.12.024
- Rinaldi, A., De Leonibus, E., Cifra, A., Torromino, G., Minicocci, E., De Sanctis, E., . . . Mele, A. (2020). Flexible use of allocentric and egocentric spatial memories activates differential neural networks in mice. *Scientific Reports*, *10*(1), 11338. doi:10.1038/s41598-020-68025-y
- Rosenthal, N., & Brown, S. (2007). The mouse ascending: perspectives for human-disease models. *Nat Cell Biol*, *9*(9), 993-999. doi:10.1038/ncb437
- Röder, P. V., Wu, B., Liu, Y., & Han, W. (2016). Pancreatic regulation of glucose homeostasis. *Exp Mol Med*, *48*(3), e219. doi:10.1038/emm.2016.6
- Sanz, C., Gautier, J. F., & Hanaire, H. (2010). Physical exercise for the prevention and treatment of type 2 diabetes. *Diabetes Metab*, *36*(5), 346-351. doi:10.1016/j.diabet.2010.06.001

- Scearce-Levie, K., Sanchez, P. E., & Lewcock, J. W. (2020). Leveraging preclinical models for the development of Alzheimer disease therapeutics. *Nature Reviews Drug Discovery*, *19*(7), 447-462. doi:10.1038/s41573-020-0065-9
- Schröder, H., Moser, N., & Huggenberger, S. (2020). The Mouse Hippocampus. In *Neuroanatomy of the Mouse: An Introduction* (pp. 267-288). Cham: Springer International Publishing.
- Sears, B., & Perry, M. (2015). The role of fatty acids in insulin resistance. *Lipids Health Dis*, *14*, 121. doi:10.1186/s12944-015-0123-1
- Seibenhener, M. L., & Wooten, M. C. (2015). Use of the Open Field Maze to measure locomotor and anxiety-like behavior in mice. *J Vis Exp*(96), e52434. doi:10.3791/52434
- Sheppard, O., & Coleman, M. (2020). Alzheimer's Disease: Etiology, Neuropathology and Pathogenesis. In X. Huang (Ed.), *Alzheimer's Disease: Drug Discovery*. Brisbane (AU): Exon Publications  
Copyright: The Authors.
- Shimabukuro, M. K., Langhi, L. G., Cordeiro, I., Brito, J. M., Batista, C. M., Mattson, M. P., & Mello Coelho, V. (2016). Lipid-laden cells differentially distributed in the aging brain are functionally active and correspond to distinct phenotypes. *Sci Rep*, *6*, 23795. doi:10.1038/srep23795
- Sigma-Aldrich. (2021a). DAPI. Retrieved from [https://www.sigmaaldrich.com/catalog/product/roche/10236276001?lang=en&region=NO&gclid=Cj0KCQjwpdqDBhCSARIsAEUJ0hNwinBeh5Vd7xap78IX5NDfxZ2Z8ZOj5AKPLWm103dktn8bBnvsFqxwaAnq5EALw\\_wcB](https://www.sigmaaldrich.com/catalog/product/roche/10236276001?lang=en&region=NO&gclid=Cj0KCQjwpdqDBhCSARIsAEUJ0hNwinBeh5Vd7xap78IX5NDfxZ2Z8ZOj5AKPLWm103dktn8bBnvsFqxwaAnq5EALw_wcB)
- Sigma-Aldrich. (2021b). GenElute™ Mammalian Genomic DNA Miniprep Kit Protocol (G1N10, G1N70, G1N350). Retrieved from [https://www.sigmaaldrich.com/technical-documents/protocols/biology/genelute-mammalian-genomic-dna-miniprep-kit.html?gclid=Cj0KCQjwmcWDBhCOARIsALgJ2Qd80QsXSrHp45ntXlxDK3huwnDJY1Ehmo44\\_fNlp9cFN2ISh\\_g6R50aArL-EALw\\_wcB](https://www.sigmaaldrich.com/technical-documents/protocols/biology/genelute-mammalian-genomic-dna-miniprep-kit.html?gclid=Cj0KCQjwmcWDBhCOARIsALgJ2Qd80QsXSrHp45ntXlxDK3huwnDJY1Ehmo44_fNlp9cFN2ISh_g6R50aArL-EALw_wcB)
- Sigma-Aldrich. (2021c). Proteinase K from *Tritirachium album*. Retrieved from <https://www.sigmaaldrich.com/catalog/product/SIAL/P2308?lang=en&region=NO>
- Spielman, L. J., Bahniwal, M., Little, J. P., Walker, D. G., & Klegeris, A. (2015). Insulin Modulates In Vitro Secretion of Cytokines and Cytotoxins by Human Glial Cells. *Curr Alzheimer Res*, *12*(7), 684-693. doi:10.2174/1567205012666150710104428
- Spinelli, M., Fusco, S., & Grassi, C. (2019). Brain Insulin Resistance and Hippocampal Plasticity: Mechanisms and Biomarkers of Cognitive Decline. *Front Neurosci*, *13*, 788. doi:10.3389/fnins.2019.00788
- Steen, E., Terry, B. M., Rivera, E. J., Cannon, J. L., Neely, T. R., Tavares, R., . . . de la Monte, S. M. (2005). Impaired insulin and insulin-like growth factor expression and signaling mechanisms in Alzheimer's disease--is this type 3 diabetes? *J Alzheimers Dis*, *7*(1), 63-80. doi:10.3233/jad-2005-7107
- Thavarajah, R., Mudimbaimannar, V. K., Elizabeth, J., Rao, U. K., & Ranganathan, K. (2012). Chemical and physical basics of routine formaldehyde fixation. *J Oral Maxillofac Pathol*, *16*(3), 400-405. doi:10.4103/0973-029x.102496
- The Jackson Laboratory. (2021a). B6;129-Tg(APP<sup>Swe,tg</sup>,tau<sup>P301L</sup>)1Lfa Psen1tm1Mpm/Mmjax. Retrieved from <https://www.jax.org/strain/004807>
- The Jackson Laboratory. (2021b). B6.BKS(D)-Lepr<sup>db</sup>/J Retrieved from <https://www.jax.org/strain/000697>

- The Jackson Laboratory. (2021c). B6SJL-Tg(APPswFLon,PSEN1\*M146L\*L286V)6799Vas/Mmjjax. Retrieved from <https://www.jax.org/strain/006554#jump-nav-6>
- Thermo Fisher. (2021). BODIPY™ 493/503 (4,4-Difluoro-1,3,5,7,8-Pentamethyl-4-Bora-3a,4a-Diaza-s-Indacene). Retrieved from <https://www.thermofisher.com/order/catalog/product/D3922#/D3922>
- Torres-Platas, S. G., Comeau, S., Rachalski, A., Bo, G. D., Cruceanu, C., Turecki, G., . . . Mechawar, N. (2014). Morphometric characterization of microglial phenotypes in human cerebral cortex. *J Neuroinflammation*, *11*, 12. doi:10.1186/1742-2094-11-12
- van Praag, H., Christie, B. R., Sejnowski, T. J., & Gage, F. H. (1999). Running enhances neurogenesis, learning, and long-term potentiation in mice. *Proc Natl Acad Sci U S A*, *96*(23), 13427-13431. doi:10.1073/pnas.96.23.13427
- van Praag, H., Shubert, T., Zhao, C., & Gage, F. H. (2005). Exercise enhances learning and hippocampal neurogenesis in aged mice. *J Neurosci*, *25*(38), 8680-8685. doi:10.1523/jneurosci.1731-05.2005
- Vorhees, C. V., & Williams, M. T. (2014). Assessing spatial learning and memory in rodents. *Illar j*, *55*(2), 310-332. doi:10.1093/ilar/ilu013
- Wakabayashi, T., Yamaguchi, K., Matsui, K., Sano, T., Kubota, T., Hashimoto, T., . . . Iwatsubo, T. (2019). Differential effects of diet- and genetically-induced brain insulin resistance on amyloid pathology in a mouse model of Alzheimer's disease. *Mol Neurodegener*, *14*(1), 15. doi:10.1186/s13024-019-0315-7
- Wakabayashi, T., Yamaguchi, K., Matsui, K., Sano, T., Kubota, T., Hashimoto, T., . . . Iwatsubo, T. (2019). Differential effects of diet- and genetically-induced brain insulin resistance on amyloid pathology in a mouse model of Alzheimer's disease. *Molecular Neurodegeneration*, *14*(1), 15. doi:10.1186/s13024-019-0315-7
- Wake, H., Moorhouse, A. J., Jinno, S., Kohsaka, S., & Nabekura, J. (2009). Resting Microglia Directly Monitor the Functional State of Synapses *In Vivo* and Determine the Fate of Ischemic Terminals. *The Journal of Neuroscience*, *29*(13), 3974-3980. doi:10.1523/jneurosci.4363-08.2009
- Walker, F. R., Beynon, S. B., Jones, K. A., Zhao, Z., Kongsui, R., Cairns, M., & Nilsson, M. (2014). Dynamic structural remodelling of microglia in health and disease: A review of the models, the signals and the mechanisms. *Brain, Behavior, and Immunity*, *37*, 1-14. doi:<https://doi.org/10.1016/j.bbi.2013.12.010>
- Walther, T. C., & Farese, R. V., Jr. (2012). Lipid droplets and cellular lipid metabolism. *Annu Rev Biochem*, *81*, 687-714. doi:10.1146/annurev-biochem-061009-102430
- Wang, W. Y., Tan, M. S., Yu, J. T., & Tan, L. (2015). Role of pro-inflammatory cytokines released from microglia in Alzheimer's disease. *Ann Transl Med*, *3*(10), 136. doi:10.3978/j.issn.2305-5839.2015.03.49
- Waters, D. L., & Shapter, F. M. (2014). The polymerase chain reaction (PCR): general methods. *Methods Mol Biol*, *1099*, 65-75. doi:10.1007/978-1-62703-715-0\_7
- Wender, R., Brown, A. M., Fern, R., Swanson, R. A., Farrell, K., & Ransom, B. R. (2000). Astrocytic glycogen influences axon function and survival during glucose deprivation in central white matter. *J Neurosci*, *20*(18), 6804-6810. doi:10.1523/jneurosci.20-18-06804.2000
- Willette, A. A., Johnson, S. C., Birdsill, A. C., Sager, M. A., Christian, B., Baker, L. D., . . . Bendlin, B. B. (2015). Insulin resistance predicts brain amyloid deposition in late

- middle-aged adults. *Alzheimers Dement*, 11(5), 504-510.e501.  
doi:10.1016/j.jalz.2014.03.011
- William Gahl, & M.D. (2021). Organelle. Retrieved from <https://www.genome.gov/genetics-glossary/Organelle>
- Wisløff, U., Ellingsen, Ø., & Kemi, O. J. (2009). High-Intensity Interval Training to Maximize Cardiac Benefits of Exercise Training? *Exercise and Sport Sciences Reviews*, 37(3), 139-146. doi:10.1097/JES.0b013e3181aa65fc
- World Health Organization. (2016). *Global report on diabetes*. Geneva.
- World Health Organization. (2017). *Global action plan on the public health response to dementia 2017 - 2025* (World Health Organization Ed.). Geneva.
- World Health Organization. (2020). The top 10 causes of death. Retrieved from <https://www.who.int/news-room/fact-sheets/detail/the-top-10-causes-of-death>
- Yang, C. N., Shiao, Y. J., Shie, F. S., Guo, B. S., Chen, P. H., Cho, C. Y., . . . Tsay, H. J. (2011). Mechanism mediating oligomeric A $\beta$  clearance by naïve primary microglia. *Neurobiol Dis*, 42(3), 221-230. doi:10.1016/j.nbd.2011.01.005
- Yankner, B. A. (1996). Mechanisms of neuronal degeneration in Alzheimer's disease. *Neuron*, 16(5), 921-932. doi:10.1016/s0896-6273(00)80115-4
- Yeadon, J. (2015). CHOOSING AMONG TYPE II DIABETES MOUSE MODELS. Retrieved from <https://www.jax.org/news-and-insights/jax-blog/2015/july/choosing-among-type-ii-diabetes-mouse-models>
- Zhang, H., Hao, Y., Manor, B., Novak, P., Milberg, W., Zhang, J., . . . Novak, V. (2015). Intranasal insulin enhanced resting-state functional connectivity of hippocampal regions in type 2 diabetes. *Diabetes*, 64(3), 1025-1034. doi:10.2337/db14-1000
- Zhang, Y., Proenca, R., Maffei, M., Barone, M., Leopold, L., & Friedman, J. M. (1994). Positional cloning of the mouse obese gene and its human homologue. *Nature*, 372(6505), 425-432. doi:10.1038/372425a0
- Zilka, N., Kazmerova, Z., Jadhav, S., Neradil, P., Madari, A., Obetkova, D., . . . Novak, M. (2012). Who fans the flames of Alzheimer's disease brains? Misfolded tau on the crossroad of neurodegenerative and inflammatory pathways. *J Neuroinflammation*, 9, 47. doi:10.1186/1742-2094-9-47

# Appendixes

## Appendix I: Equipment

*Table 12: Overview of equipment used in the study*

<b>Equipment</b>	<b>Producer</b>
Applied Biosystems 2720 Thermal Cycler	Thermo Fisher Scientific, USA
Corning® cover glasses, thickness 1, 24x60 mm	Merck, Germany
Exer 3/6 Treadmill	Columbus Instruments, USA
GenElute Mammalian Genomic DNA Miniprep Kit (G1N350/G1N70)	Sigma-Aldrich, USA
Grant Boekel BBD block heater	Boekel Scientific, USA
GreenLine cages (Sealsafe Plus GM500)	Tecniplast Group, USA
Heraeus Pico 17 Microcentrifuge	Thermo Fisher Scientific, USA
Heraeus Fresco 21 Microcentrifuge	Thermo Fisher Scientific, USA
HM 450 Sliding Microtome	Thermo Fisher Scientific, USA
ImageJ Imaging Program	Fiji Is Just ImageJ, Germany
KS 34 Enclosed Cooling System	Thermo Scientific, USA
LSM 880 with Airyscan confocal microscope	Carl Zeiss Microscopy, Germany
Minishaker MS2	IKA, Germany
MiniSpec LF90II	Bruker, Germany
Nikon SMZ645 stereo microscope	Nikon Instruments, USA
Nunclon 24-well cell culture plates (6 x 4 well trays)	Thermo Fisher Scientific, USA
Paintbrush Watercolour Round No. 0 and 3/0 pine marten hair	Panduro Hobby, Norway
Parafilm M PM-996	Bemis, USA



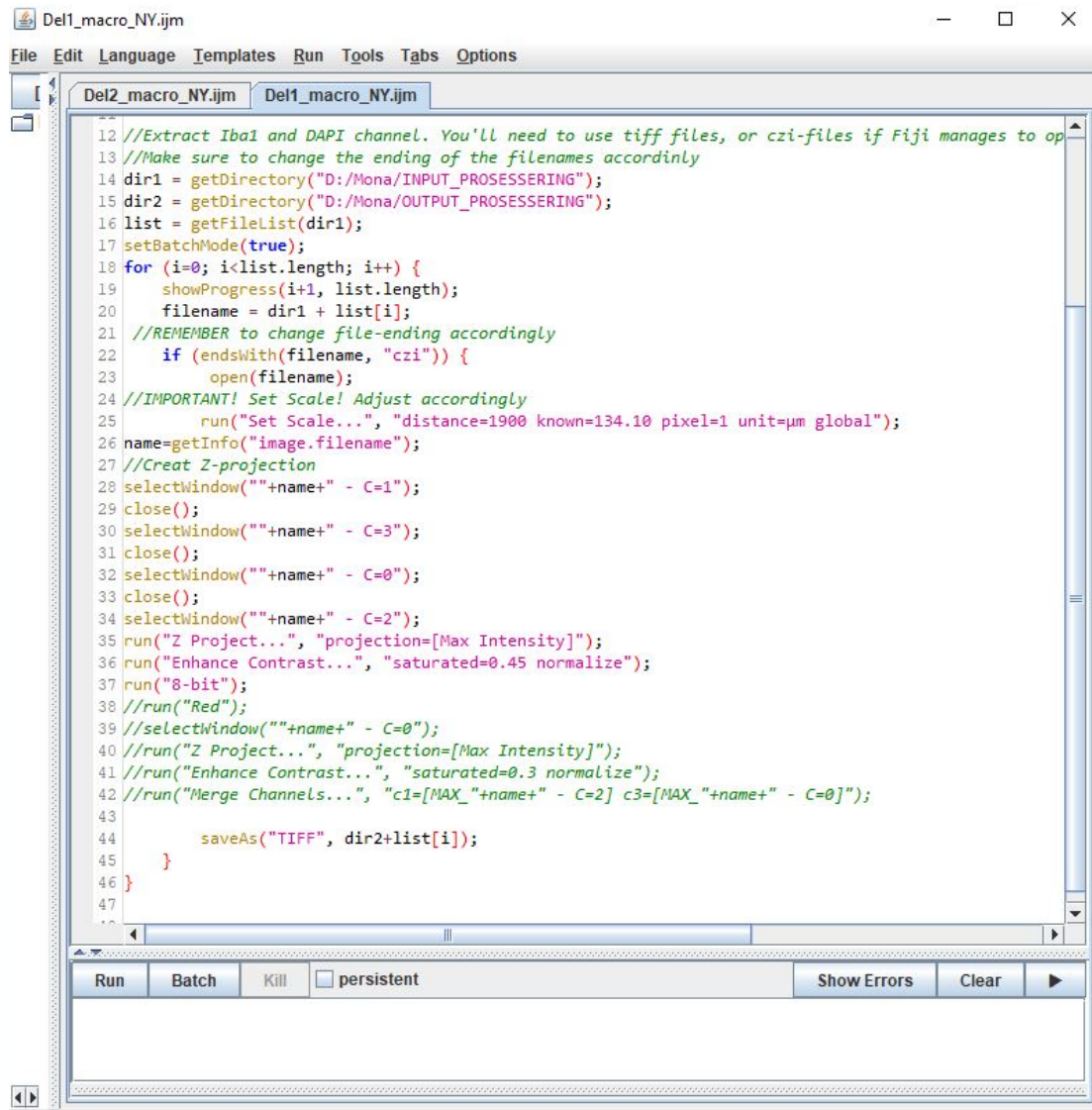
Qualitative filter paper, grade 403	VWR, USA
SuperFrost Plus™ Adhesion Microscope Slides	Thermo Scientific, USA
Water bath	GFL, Germany
Watson Marlow 323U, Peristaltic pump with 323, rapid load flip-top pumphed	Watson Marlow Pumps, United Kingdom

## Appendix II: MWM form

Dag #			Morris Water Maze – prosjekt: Diabetesrelatert demens/lipiddråper			Dato:		
Plattform i N SW = sørvest SE = sørøst E = øst W = vest			OP 1:	Starttid:	Sluttid:	Vanntemp. 1:	60 sek maks trial-tid/30 sek på plattform/ *plassert på plattform	
				LUX 1:		Vanntemp. 2:		
			OP 2:	LUX 2:		Vanntemp. 3:		
				LUX 3:		Vanntemp. 4:		
Gruppe :								
Dyr ID: #			Merking (øre, hale):			Bur #:		
Trial	Slipp punkt	Plattform lokasjon	Kommentarer (flyter, hopper av plattform osv.)					
1	SW	N						
2	SE	N						
3	E	N						
4	W	N						
Gruppe :								
Dyr ID: #			Merking (øre, hale):			Bur #:		
Trial	Slipp punkt	Plattform lokasjon	Kommentarer (flyter, hopper av plattform osv.)					
1	SW	N						
2	SE	N						

3	E	N	
4	W	N	
<b>Gruppe :</b>			
<b>Dyr ID: #</b>		<b>Merking (øre, hale):</b>	<b>Bur #:</b>
<b>Trial</b>	<b>Slipp punkt</b>	<b>Plattform lokasjon</b>	<b>Kommentarer (flyter, hopper av plattform osv.)</b>
1	SW	N	
2	SE	N	
3	E	N	
4	W	N	
<b>Gruppe :</b>			
<b>Dyr ID: #</b>		<b>Merking (øre, hale):</b>	<b>Bur #:</b>
<b>Trial</b>	<b>Slipp punkt</b>	<b>Plattform lokasjon</b>	<b>Kommentarer (flyter, hopper av plattform osv.)</b>
1	SW	N	
2	SE	N	
3	E	N	
4	W	N	

## Appendix III: Fiji macros



```
Del1_macro_NY.ijm
File Edit Language Templates Run Tools Tabs Options
Del2_macro_NY.ijm Del1_macro_NY.ijm
12 //Extract Iba1 and DAPI channel. You'll need to use tiff files, or czi-files if Fiji manages to op
13 //Make sure to change the ending of the filenames accordinly
14 dir1 = getDirectory("D:/Mona/INPUT_PROSESSERING");
15 dir2 = getDirectory("D:/Mona/OUTPUT_PROSESSERING");
16 list = getFileList(dir1);
17 setBatchMode(true);
18 for (i=0; i<list.length; i++) {
19     showProgress(i+1, list.length);
20     filename = dir1 + list[i];
21     //REMEMBER to change file-ending accordingly
22     if (endsWith(filename, "czi")) {
23         open(filename);
24         //IMPORTANT! Set Scale! Adjust accordingly
25         run("Set Scale...", "distance=1900 known=134.10 pixel=1 unit=µm global");
26         name=getInfo("image.filename");
27         //Creat Z-projection
28         selectWindow(""+name+" - C=1");
29         close();
30         selectWindow(""+name+" - C=3");
31         close();
32         selectWindow(""+name+" - C=0");
33         close();
34         selectWindow(""+name+" - C=2");
35         run("Z Project...", "projection=[Max Intensity]");
36         run("Enhance Contrast...", "saturated=0.45 normalize");
37         run("8-bit");
38         //run("Red");
39         //selectWindow(""+name+" - C=0");
40         //run("Z Project...", "projection=[Max Intensity]");
41         //run("Enhance Contrast...", "saturated=0.3 normalize");
42         //run("Merge Channels...", "c1=[MAX_"+name+" - C=2] c3=[MAX_"+name+" - C=0]");
43
44         saveAs("TIFF", dir2+list[i]);
45     }
46 }
47
Run Batch Kill persistent Show Errors Clear
```

*Figure 46: Screenshot of the first macro used to analyze microglia activation. The macro used raw confocal images to create 8-bit greyscale images of microglia and nuclei.*

```

Del2_macro_NY.ijm
File Edit Language Templates Run Tools Tabs Options

Del2_macro_NY.ijm
2 //You "input" should be previous "output"
3 dir1 = getDirectory("D:/OUTPUT_PROSESSING");
4 dir2 = getDirectory("D:/Mona/DEL2_Masker");
5 list = getFileList(dir1);
6 setBatchMode(true);
7 for (i=0; i<list.length; i++) {
8     showProgress(i+1, list.length);
9     filename = dir1 + list[i];
10    if (endsWith(filename, ".tif")) {
11        open(filename);
12        //IMPORTANT! Set Scale! Adjust accordingly
13        run("Set Scale...", "distance=1900 known=134.10 pixel=1 unit=µm global");
14    name=getInfo("image.filename");
15        //selectWindow("Classification result");
16        run("8-bit");
17        //setAutoThreshold("Default dark");
18        //run("Threshold...");
19        setThreshold(67, 255);
20        run("Convert to Mask");
21        run("Despeckle");
22        run("Despeckle");
23        run("Analyze Particles...", "size=30-200 show=Masks display clear summarize add");
24        selectWindow("Results");
25        saveAs("Results", "D:/Mona/DEL2_Resultater/"+name+"-Results.csv");
26        //saveAs("Results", "D:/Mona/DEL2_Resultater/"+name+"-Summary.csv");
27        roiManager("Save", "D:/Mona/DEL2_resultater/"+name+"-ROI.zip");
28        saveAs("TIFF", dir2+list[i]);
29    }
30 }
31

Run Batch Kill  persistent Show Errors Clear ▶

```

**Figure 47: Screenshot of the third macro used to analyze microglia activation.** The macro used the greyscale images to create ROIs containing Iba1+ and DAPI+ microglia.

```

10 // "Destination directory" is your output folder
11
12 // Extract Iba1 and DAPI channel. You'll need to use tiff files, or czi-files if Fiji manages to open them
13 // Make sure to change the ending of the filenames accordingly
14 dir1 = getDirectory("D:/Mona/INPUT_PROSESSING");
15 dir2 = getDirectory("D:/Mona/Gamle mapper/INPUT_WEKA");
16 list = getFileList(dir1);
17 setBatchMode(true);
18 for (i=0; i<list.length; i++) {
19     showProgress(i+1, list.length);
20     filename = dir1 + list[i];
21     // REMEMBER to change file-ending accordingly
22     if (endsWith(filename, "czi")) {
23         open(filename);
24         // IMPORTANT! Set Scale! Adjust accordingly
25         run("Set Scale...", "distance=1900 known=134.10 pixel=1 unit=µm global");
26 name=getInfo("image.filename");
27 // Creat Z-projection
28 selectWindow(""+name+" - C=1");
29 close();
30 selectWindow(""+name+" - C=3");
31 close();
32 selectWindow(""+name+" - C=2");
33 run("Z Project...", "projection=[Max Intensity]");
34 run("Enhance Contrast...", "saturated=0.3 normalize");
35 run("Red");
36 selectWindow(""+name+" - C=0");
37 run("Z Project...", "projection=[Max Intensity]");
38 run("Enhance Contrast...", "saturated=0.3 normalize");
39 run("Merge Channels...", "c1=[MAX_"+name+" - C=2] c3=[MAX_"+name+" - C=0]");
40
41     saveAs("TIFF", dir2+list[i]);
42     }
43 }
44
45

```

**Figure 48:** Screenshot of the macro used to create a red and blue control images by creating Z-projections and merging Iba1 and DAPI channel.